Mechanistic insights into anchoring the cytokinetic ring

By

Chloe Elizabeth Snider

Dissertation

Submitted to the Faculty of the

Graduate School of Vanderbilt University

in partial fulfillment of the requirements

for the degree of

DOCTOR OF PHILOSOPHY

in

Cell and Developmental Biology

February 28th, 2021

Nashville, Tennessee

Approved:

Matthew J. Tyska, Ph.D.

Ian G. Macara, Ph.D.

Alissa M. Weaver, M.D., Ph.D.

Matthew J. Lang, Ph.D.

Kathleen L. Gould, Ph.D.

ACKNOWLEDGEMENTS

The work described herein would not have been possible without the support of my mentors, peers, family, and friends. To the following I offer my sincerest thanks.

First, I would like to express my immense gratitude to my mentor, Dr. Kathy Gould, for providing the environment that fostered my success. Thank you for the lessons, the encouragement, and the many celebrations. I acknowledge my collaborators and informal mentors: Dr. Lauren Jackson, Dr. Marjia Zanic, Dr. Melanie Ohi, Dr. Mintu Chandra, Dr. Göker Arpağ, and Dr. Scott Collier. Thank you for your support and for allowing me to try and think about new things. Thank you to my committee members, Dr. Matthew Tyska, Dr. Ian Macara, Dr. Alissa Weaver, and Dr. Matthew Lang for your input and encouragement. I would also like to thank Dr. Kerry Bloom, Dr. Elaine Yeh, and Dr. Andrew Stephens for providing my first opportunity to conduct research at the University of North Carolina and for continuing to support my career.

I would like to thank the members of the Gould lab, past and present, for offering training, support, a sounding board, criticism when necessary, and a fun environment for science. I also thank the Vanderbilt Department of Cell and Developmental Biology for excellent scientific and administrative support.

I acknowledge the financial support received from the predoctoral fellowship awarded by the American Heart Association and support from the Cellular, Biochemical, and Molecular Sciences training grant. Thank you to the Vanderbilt Cell Imaging Shared Resource for the access to fancy microscopes and resources.

Lastly, I thank my family and friends for their support and encouragement. Thank you to my parents, siblings, grandparents, and the extended Snider bunch for the words of encouragement. Thank you to Michael Tackenberg, for your partnership in life and in science. I

am also grateful to the friends I’ve made throughout my graduate school journey for all of the happy hours, the laughs, the cries, and the lasting friendships.

TABLE OF CONTENTS

LIST OF TABLES

Table **Page**

LIST OF FIGURES

Figure **Page**

Chapter I

Introduction

Introduction to cytokinesis in *Schizosaccharomyces pombe*

Cytokinesis is the last step in cell division in which two daughter cells physically separate. This process must be spatially and temporally coordinated with the division of the segregating DNA in order to avoid damage to the dividing genome. Failure during cytokinesis can lead to cell death, aneuploidy, or the formation of tetraploid intermediates, which can promote carcinogenesis (Fujiwara et al., 2005; Ganem et al., 2009; Hayashi and Karlseder, 2013; Krajcovic et al., 2011). However, differential regulation of cytokinesis is employed during development; for instance, cardiomyocytes purposefully inhibit cytokinesis to become multinucleate (Clubb, 1984; Lacroix and Maddox, 2012; Li et al., 1996; Li et al., 1997). Therefore, mechanistic studies of cytokinesis are informative for understanding both normal development and disease pathologies.

In eukaryotic cells, cytokinesis takes place in four general steps (reviewed in (Guertin et al., 2002)). The first is the selection of the division plane. Although different organisms employ a variety of mechanisms to specify the site of cytokinesis, the general strategy is that the cytokinetic plane is established in a spatially distinct area from that of the dividing genome. The second step is the assembly of an actin- and myosin-based cytokinetic ring (CR). The CR is a contractile structure that must be built in close proximity to the plasma membrane (PM), so that during the third step, CR constriction, opposing membranes are brought together as the CR decreases in diameter. In the last step, abscission, the two daughter cells physically separate.

Cell division in *Schizosaccharomyces pombe,* or fission yeast, has been studied in detail for over two decades. *S. pombe* are rod-shaped unicellular yeast that grow by elongating their tips and divide by medial fission. Like many other eukaryotes, *S. pombe* assemble and constrict an actin- and myosin-based CR on the PM to facilitate cytokinesis (Pollard and Wu, 2010). Because of the technical advantages of working with *S. pombe,* including short generation times and amenability to facile and precise genetic manipulation and large-scale biochemical assays, studies utilizing this organism have provided detailed insights into the structure and function of the CR (Cheffings et al., 2016; Goyal et al., 2011; Mangione and Gould, 2019; Pollard, 2010; Rincon and Paoletti, 2016). As a result, *S. pombe* is perhaps the premier model for understanding the mechanistic basis of eukaryotic cytokinesis.

In *S. pombe,* the cytokinetic machinery typically clusters in precursor nodes. The medial assembly of nodes is promoted by the shuttling of the anillin-like protein Mid1 out of the nucleus in late G2 phase, promoting its accumulation on the cortex proximal to the central nuclear position (Sohrmann et al., 1996). Mid1 then recruits additional components such as myosin II, IQGAP Rng2, F-BAR protein Cdc15, and formin Cdc12 that assemble in punctae on the medial cortex of the cell (Wu et al., 2003). The nodes are then assembled into a coherent CR in the cell center using a “search-capture-pull-release” mechanism dependent upon actin polymerization and myosin activity (Vavylonis et al., 2008; Wu et al., 2006). The next step is CR maturation, during which the CR must remain stably anchored in the cell center while nuclear division occurs. Once the daughter nuclei have segregated to opposite ends of the cell, the CR then constricts and disassembles (Pelham and Chang, 2002; Pollard and Wu, 2010; Stachowiak et al., 2014). Concomitantly, cell wall material is synthesized and deposited behind the CR to form the division septum, or the new cell wall between the two daughter cells, providing the force necessary for CR constriction (Muñoz et al., 2013; Proctor et al., 2012).

Despite decades of work detailing how the division plane is selected and how the CR is assembled, our understanding of how the CR is attached to the PM is incomplete. *S. pombe*

build a medial CR early in mitosis (Kitayama et al., 1997; Marks and Hyams, 1985). How the CR remains anchored until constriction is not yet clear although several players have been implicated. One is the paxillin-like protein Pxl1 that plays a role in CR anchoring and integrity evidenced by CR sliding and splitting during anaphase in *pxl1*Δ (Cortés et al., 2015; Ge and Balasubramanian, 2008). Another factor is the cell wall: loss of β(1,3)glucan (Muñoz et al., 2013) or loss of the integral membrane protein Sbg1 (Davidson et al., 2016; Sethi et al., 2016) result in CR sliding and instability, suggesting that cell wall-PM linkage is important for CR maintenance. Additionally, the microtubule post-anaphase array ensures a medial CR during a cytokinesis arrest (Pardo and Nurse, 2003). Another major factor is the essential F-BAR protein Cdc15: when *cdc15* expression is repressed or Cdc15 oligomerization disrupted, the CR can slide along the PM and disassemble (Arasada and Pollard, 2014; McDonald et al., 2015). In each of these situations, CR sliding is observed in only a fraction of cells (Arasada and Pollard, 2014; Cortés et al., 2015; McDonald et al., 2015; Pardo and Nurse, 2003), indicating that multiple mechanisms contribute to CR anchoring. Consistent with this, combined repression of *pxl1* with a hypomorphic *cdc15* allele results in exacerbated CR sliding (Cortés et al., 2015). In addition to protein factors, the lipid composition of the PM has been implicated in promoting the integrity of cytokinesis as *efr3*Δ, which encodes a scaffolding protein implicated in phosphoinositide metabolism, displays defects in division site placement (Baird et al., 2008; Chen et al., 2015). Although there is evidence that the lipid composition of the PM influences cytokinesis in other eukaryotic systems, this was an unexplored subject area in *S. pombe*, and part of my dissertation research investigated this as described in Chapters II-IV.

Evidence for roles of plasma membrane lipid composition in cytokinesis

Though phosphoinositides (PIPs) comprise ~5-10% of PM lipid species in mammalian cells (Wenk et al., 2003) and are important for cytokinesis (Echard, 2012), the mechanisms by which PIPs promote accurate cytokinesis are not fully defined.

Of the 7 PIP species found in the cell, only a subset have been implicated in cell division, including phosphatidylinositol-4-phosphate (PI4P) and phosphatidylinositol-4,5-bisphosphate ($PI(4,5)P_2$). A role for PI4P in cytokinesis was revealed through studies focused on PI4-kinases, the enzymes that generate PI4P from phosphatidylinositol (PI). In *Drosophila melanogaster* spermatocytes, absence of the type IIIβ PI4-kinase (PI4KIIIβ) encoded by *four wheel drive* results in cytokinesis failure and multinucleate spermatids (Brill et al., 2000). Similarly, the catalytic activity of *S. pombe* PI4KIIIβ Pik1 is essential for normal septation and abscission (Park et al., 2009). The role of PI4KIIIβ in human cells is less clear although one study showed that elevated levels of PI4KIIIβ activity and thus higher PI4P levels inhibit cytokinesis, resulting in multinucleate cells (Rajamanoharan et al., 2015). Type IIIα PI4-kinases (PI4KIIIα) have also been implicated in cytokinesis. *D. melanogaster* cells lacking PI4KIIIα display cytokinesis defects that result in binucleate cells (Eggert et al., 2004). Additionally, deletion of the gene encoding Efr3, a non-essential PM scaffolding protein of the *S. pombe* PI4KIIIα Stt4, results in off-center septation, indicating a defect in cytokinesis (Chen et al., 2015). A role of PI4KIIIα in human cytokinesis has not been reported though the kinase and scaffolding machinery are conserved from yeast to humans (Baird et al., 2008; Chung et al., 2015).

Another PIP species implicated in modulating cell division is $PI(4,5)P_2$, the most abundant PIP species in the PM. $PI(4,5)P_2$ is enriched at the division site of mammalian (Abe et al., 2012; Dambournet et al., 2011; Emoto et al., 2005; Field et al., 2005; Kouranti et al., 2006), *S. pombe* (Snider et al., 2017; Zhang et al., 2000) and *D. melanogaster* S2 (El Kadhi et al., 2011; Roubinet et al., 2011) cells. In addition, PI5-kinases that generate $PI(4,5)P_2$ from PI4P localize to the division site in human (Emoto et al., 2005), *D. melanogaster* S2 (Roubinet et al., 2011) and *S. pombe* (Zhang et al., 2000) cells. $PI(4,5)P_2$ can also be generated by PI3-phosphatases acting on $PI(3,4,5)P_3$ and PI3-phosphatases localize to the division site in *Dictyostelium discoideum* and *S. pombe* (Janetopoulos et al., 2005; Mitra et al., 2004). In HeLa

and Chinese hamster ovary cells, depletion of PM $PI(4,5)P_2$ results in separation of the PM from the actin cytoskeleton and cytokinesis failure (Field et al., 2005). It is hypothesized that proteins that mediate actin-PM adhesion may require $PI(4,5)P_2$ for this function; candidates relevant to the process of cytokinesis include anillin (Liu et al., 2012; Sun et al., 2015) and other regulators of F-actin dynamics such as N-WASP and profilin (Higgs and Pollard, 2000; Machesky et al., 1990). However, the exact combination of molecules involved in CR detachment when $PI(4,5)P_2$ is depleted remains to be determined.

F-BAR domains: membrane anchors for actin-based structures

BAR domains: oligomeric bridges between membrane and actin networks

Bin/Amphiphysin/Rvs (BAR) superfamily proteins are critical components of membrane-linked processes in eukaryotic cells, including endocytosis, cytokinesis, and motility. These proteins are defined by the namesake BAR domain, which dimerizes to form a crescent-shaped bundle of six alpha-helices that directly binds membrane. BAR proteins are usually modular and contain additional domains that generally link components of the actin cytoskeleton to membrane via the BAR domain (Carman and Dominguez, 2018; Nishimura et al., 2018; Suetsugu et al., 2010).

BAR domains associate with membrane through positively charged residues on their concave faces that interact with negatively charged lipids, and they have the propensity to self-associate into oligomeric assemblies (Carman and Dominguez, 2018). The membrane-binding properties, tendency to oligomerize, banana-shape of the dimers, and localization of some BAR domains at sites of membrane curvature in cells led to the view that BAR domains are curvature generating and/or sensing modules. Indeed, the earliest in vitro studies of BAR domains demonstrated their ability to tubulate when concentrated on membrane (Itoh and De Camilli, 2006). However, later studies on the Fes/Cip4 homology BAR (F-BAR) subfamily revealed that this description of BAR domain function may be over-generalized. The F-BAR subfamily is

distinguished from classical BAR domains based on sequence and structure; F-BAR dimers form a more extended and less curved shape compared to BAR dimers (Frost et al., 2007). Although some F-BAR domains tubulate membrane in vitro, a subset of the family cannot, suggesting that membrane curvature generation is not a unifying function of the family (McDonald et al., 2015).

Like classical BARs, F-BAR proteins typically have additional domains. Many have at least one SH3 domain that recruits factors to link actin networks to membrane and/or promote actin polymerization locally (McDonald and Gould, 2016b). Though most known partners bind to the SH3 domains of F-BAR proteins, there is growing evidence that F-BAR domains themselves function as protein assembly platforms.

Here, I review the structures and oligomerization strategies of F-BAR domains and how these properties confer biological functions. Additionally, I discuss the emerging evidence that oligomerization allows F-BAR domains to polymerize protein interaction networks to promote the structure and function of actin-based structures, including the CR.

All F-BAR domains bind, but not all bend membrane

BAR domains have been described as generators, stabilizers, and/or sensors of membrane curvature. Membrane deformation activity was first reported for the BAR domain of human amphiphysin (reviewed in (Itoh and De Camilli, 2006)). Purified amphiphysin BAR domain binds and deforms liposomes in vitro and electron microscopy (EM) analyses suggested that it self-associates to drive vesicle tubulation. Further evidence for amphiphysin's ability to deform membrane was obtained by overexpressing its BAR domain in cultured cells, which resulted in plasma membrane tubulation. These two assays – adding purified BAR domains to liposomes and over-expressing BAR domains in cultured cells – became standard for assaying tubulation activity.

Further studies utilizing these assays revealed that multiple members of the BAR superfamily can generate membrane curvature at high concentrations. These include some members of the F-BAR subfamily (Frost et al., 2007; Henne et al., 2007; Shimada et al., 2007), leading to the idea that F-BAR domains may generate different degrees of membrane curvature than classical BARs. There is supporting evidence for this hypothesis, as F-BARs cluster in spatially separate areas when overexpressed simultaneously with classical BAR domains in cultured cells, and F-BARs generate wider tubules than classical BARs (Frost et al., 2008). However, comprehensive examination of human F-BAR family members showed that some do not tubulate membranes at all, but simply bind it (McDonald et al., 2015). These F-BAR domains are also incapable of tubulating membranes when overexpressed in cultured cells.

If membrane deformation is a critical function of BAR domains, then why do some members, specifically a subset of the F-BAR family, lack this ability? Here, I discuss the developing understanding of the diversity of oligomerization strategies employed by F-BAR domains, and how this relates to in vitro tubulation activity, and more importantly, to in vivo function.

F-BAR oligomerization strategies inform function

F-BAR domains use varying modalities to oligomerize. For example, crystal packing contacts implicate residues at the tips of the F-BARs FBP17 and CIP4 in mediating oligomerization (Shimada et al., 2007). Cryo-EM of CIP4 F-BAR assembled on membrane allowed for single-particle reconstruction, which provided further evidence of tip-to-tip assembly of dimers in vitro (Frost et al., 2008). This analysis also revealed that lateral contacts can occur between neighboring F-BAR dimers, facilitating membrane tubulation in vitro and resulting in spiral filaments with the concave faces of the assembled F-BAR domains contacting membrane. Disrupting CIP4 F-BAR domain tip-to-tip or lateral oligomerization reduces tubule formation in standard assays (Frost et al., 2008; Shimada et al., 2007).

The *Schizosaccharomyces pombe* Imp2 F-BAR domain crystalized as a dimer of dimers, with residues at the tip of one dimer contacting the core of a neighboring dimer, resulting in a helical assembly when extended mathematically (McDonald et al., 2016). Similar to the orientation of CIP4 F-BAR dimers on membrane tubules, the concave membrane-binding surfaces of the Imp2 F-BAR oligomer face the interior of the helical assembly. This oligomerization strategy is consistent with Imp2 F-BAR domain's ability to tubulate vesicles in vitro, and mutation of oligomerization residues renders Imp2 tubulation-deficient (McDonald et al., 2016). It is logical that F-BAR domains like CIP4 and Imp2 that can assemble into spiral structures are able to tubulate membrane in vitro.

However, F-BAR domains also assemble on flat membranes, and this requires different oligomerization strategies. FBP17 F-BAR dimers make tip-to-tip contacts when assembled on a flat membrane in vitro and imaged by EM (Frost et al., 2008). Intriguingly, in this instance, F-BAR domains contact the membrane with the lateral side of the crescent, rather than the canonical membrane-binding surface, occluding lateral oligomeric contact sites observed on membrane tubules. Although this flat assembly has not been detected in vivo, it may be relevant to FBP17 action at lamellipodia membranes (Tsujita et al., 2015). In another example of sheet-like assembly, the mammalian GAS7 F-BAR domain forms flat filamentous oligomers (FFO) through lateral interactions of the F-BAR dimers on monolayers in vitro (Hanawa-Suetsugu et al., 2019). Similar to the orientation of FBP17 F-BAR domains observed on a flat membrane, the configuration of GAS7 dimers in the FFO suggests that residues on the lateral side of the GAS7 F-BAR contact the membrane. This oligomerization strategy of the GAS7 F-BAR domain into a flat sheet is consistent with its lack of tubulation activity (Hanawa-Suetsugu et al., 2019; McDonald et al., 2015).

The *S. pombe* Cdc15 F-BAR domain forms tip-to-tip linear oligomers as visualized by EM, mediated by electrostatic interactions between reciprocally charged residues at dimer tips (McDonald et al., 2015; Roberts-Galbraith et al., 2010). A strictly linear assembly of Cdc15 F-

BAR domains is consistent with their inability to deform membrane in vitro and also with the function of Cdc15 at a flat membrane along the cell wall of rod-shaped *S. pombe* (Fankhauser et al., 1995). *D. melanogaster* Nervous wreck (Nwk) F-BAR domain is also non-tubulating and assembles tip-to-tip on monolayer membranes in vitro. Nwk dimers come together in a V-shape, resulting in zig-zag assemblies as visualized by EM (Becalska et al., 2013). This arrangement may explain the scalloped shapes of Nwk-bound membranes in vitro and when Nwk is overexpressed in S2 cells (Becalska et al., 2013). In the Cdc15 and Nwk F-BAR examples, the evidence suggests that the concave faces are utilized for membrane-binding when assembled in an oligomer.

Mammalian GAS7 and *S. pombe* Cdc15 exemplify how F-BAR domain structure and oligomerization strategy are connected to biological function. Consistent with the shallow curvature and sheet-like assembly of the GAS7 F-BAR domain, GAS7 localizes to the flat membrane at the base of the phagocytic cup in macrophages as revealed by super-resolution microscopy (Hanawa-Suetsugu et al., 2019). Furthermore, mutations that disrupt GAS7 F-BAR domain oligomerization inhibit phagocytosis, indicating the functional requirement for this GAS7 oligomerization mechanism. The mammalian FCHSD2 F-BAR dimer also has shallow curvature and localizes to the flat membrane at the base of clathrin-coated pits during endocytosis (Almeida-Souza et al., 2018b). It is unknown what oligomeric FCHSD2 looks like in this context, but it will be interesting to see if FCHSD2 also assembles into flat sheets like the GAS7 F-BAR domain or in zig-zags like its orthologue Nwk (Becalska et al., 2013). *S. pombe* Cdc15 is a scaffolding protein of the cytokinetic ring, linking protein partners to the plasma membrane. In vitro studies demonstrated that oligomerization allows high avidity Cdc15 membrane-binding, suggesting that oligomerization allows efficient scaffolding of the cytokinetic ring in cells (McDonald et al., 2015). In support of this, Cdc15 oligomerization mutants are more dynamic and less stably associated with the membrane compared to wildtype and display cytokinetic ring instability. The shallow curvature of the Cdc15 F-BAR dimer, the tip-to-tip oligomerization

strategy, and the inability to tubulate membrane in vitro are all consistent with function at a flat membrane in vivo.

At flat membranes, instead of driving membrane curvature, F-BAR domain oligomerization may function to generate high avidity membrane-binding and concentrate binding partners at the membrane. For instance, Cdc15 scaffolds a network of proteins via its F-BAR and SH3 domains that promote completion of cytokinesis (Ren et al., 2015; Roberts-Galbraith et al., 2009). In mammalian cells, oligomerized F-BAR domains likely function similarly to create a high-density of binding modules for partners that promote actin polymerization for endocytosis, as well as podosome and phagocytic cup formation (Almeida-Souza et al., 2018b; Ho et al., 2004; Takano et al., 2008; Tsuboi et al., 2009).

While it is now appreciated that F-BAR domains oligomerize in a variety of modes, the next frontier is linking the structure of F-BAR dimers and their higher-order oligomeric assemblies to functions in vivo. For example, it is unclear how helical structures formed by CIP4 and FBP17 F-BAR domains in vitro relate to their functions at flat membranes, such as those of lamellipodia (Tsujita et al., 2015). While the F-BAR domain of PACSIN/Syndapin can generate membrane tubules in vitro, crystal lattice contacts suggest that PACSIN1 assembles into sheets with contacts between the tip of one dimer and the core of another, with the membrane binding face of each dimer facing the same direction toward the membrane (Wang et al., 2009). It is unclear how such an assembly could generate membrane tubulation, and it is unknown if this flat assembly is utilized in vivo (Wang et al., 2009). In the case of *S. pombe* Imp2, although the F-BAR domain forms helical assemblies and tubulates membrane in vitro, structure-function analysis showed that mutations that disrupt oligomerization have little consequence for Imp2's function in cytokinesis in vivo (McDonald et al., 2016). Interestingly in this regard, it has emerged in recent years that membrane crowding of any protein on a membrane can generate curvature (Snead et al., 2017), and membrane-anchored GFP is sufficient to drive GUV fission (Steinkühler et al., 2020). These biophysical studies illustrate that caution is warranted when

drawing conclusions about the physiological relevance of membrane deformation from in vitro assays performed with supra-physiological concentrations of F-BAR domains.

F-BAR domains as protein interaction modules

F-BAR domains are typically linked to other domains that have protein interaction and/or enzymatic activities that in turn link F-BAR proteins to the actin cytoskeleton (reviewed in (McDonald and Gould, 2016b; Suetsugu and Gautreau, 2012)). Hence, F-BAR domains might be viewed simply as membrane-targeting modules, which merely localize other domains to their site(s) of action. Indeed, substitutions of an essential F-BAR domain in yeast with various yeast and human F-BAR domains support cell viability, suggesting that F-BAR domains are remarkably interchangeable membrane-binding modules (Mangione et al., 2019). However, there is mounting evidence that a key F-BAR domain function is mediating protein-protein interactions in addition to protein-membrane interactions, and these dual properties can allow F-BAR domains to form interaction platforms that link complex actin-based structures to membrane.

The list of reported F-BAR domain binding partners is expanding, as is insight into the functional consequences of such interactions in different biological contexts. For some F-BAR domains, a partner is required for robust localization to a site of action within the cell. An example of this type of relationship is the cooperation between *S. pombe* cytokinetic F-BAR protein Rga7 and coiled-coil protein Rng10 (Liu et al., 2019). Although the Rga7 F-BAR domain binds membrane in vitro, it does so with low affinity unless in complex with Rng10, and in cells Rga7 does not localize to the cell division site without Rng10, or vice-versa.

In platelets and megakaryocytes, the F-BAR domain of PACSIN2 binds the actin-binding protein Filamin A, and deletion or mutation of Filamin A disrupts PACSIN2 localization (Begonja et al., 2015). In epithelial cells, PACSIN2 F-BAR domain binds to polycystin-1 to facilitate its localization at lamellipodia membranes (Yao et al., 2014). Similarly, the cytoskeleton-associated

protein pyrin binds the PSTPIP1 F-BAR domain (Shoham et al., 2003). When expressed together in COS cells, pyrin directs PSTPIP1 to inflammasomes, while PSTPIP1 does not localize there on its own (Waite et al., 2009). In these cases, testing if F-BAR affinity for membrane is modulated by interacting partners would provide important mechanistic insight.

Binding partners also regulate F-BAR protein properties other than membrane binding. The *D. melanogaster* Nwk promotes membrane remodeling at synapses by activating WASp and directing actin assembly. Nwk's membrane and actin remodeling activities are autoinhibited by interactions between its N-terminal F-BAR and C-terminal SH3 domains (Stanishneva-Konovalova et al., 2016). Full activation of Nwk requires association with membrane, WASp, and Dap160/intersectin, a partner that binds both the F-BAR domain and a C-terminal SH3 domain of Nwk (Del Signore et al., 2020). Multi-step activation of Nwk may ensure it promotes actin assembly only at the appropriate place and time. It will be interesting to determine if other F-BAR proteins are regulated in such a multi-factor manner.

In a reciprocal mechanism to that described for Nwk, some F-BAR domains influence the activity or localization of their partners. For example, during cytokinesis in *Saccharomyces cerevisiae*, the Hof1 F-BAR domain binds and inhibits Chs4, an chitin synthase III activator, which synthesizes the secondary septum at the division site (Oh et al., 2017). Because Chs4 arrives at the bud neck during the early stages of cytokinesis, inhibition by the Hof1 F-BAR domain prevents premature septum synthesis (Oh et al., 2017). The Hof1 F-BAR domain also inhibits actin cable formation by binding the formin Bnr1 to block actin nucleation (Garabedian et al., 2018). This regulation ensures normal actin cable morphology and secretion (Graziano et al., 2014).

F-BAR domains also serve to anchor proteins directly to membrane. In *S. pombe,* the Cdc15 F-BAR domain binds the cytokinetic formin Cdc12, promoting its recruitment to the division site where it nucleates the F-actin of the cytokinetic ring (Willet et al., 2015a). Acting as a bridge between the cytoskeleton and the PM through F-BAR domain binding to Cdc12 is likely

a key mechanism by which Cdc15 anchors the cytokinetic ring. The human F-BAR protein PSTPIP1 similarly localizes to the plasma membrane of the cytokinetic cleavage furrow (Spencer et al., 1997), but scaffolding roles for the PSTPIP1 F-BAR domain are yet to be explored in this context.

In some cases, the F-BAR domain residues that mediate protein-protein interactions have been identified, but there does not appear to be a unifying mechanism of F-BAR domain–protein engagement. The PACSIN2 F-BAR domain associates with F-actin in vitro, but the residues implicated in this interaction are on the concave side of the F-BAR domain, which is also the membrane-binding face (Kostan et al., 2014). This suggests that the PACSIN2 F-BAR domain would be unable to bind membrane and F-actin simultaneously, and the physiological function of this interaction is unclear. For the Filamin A–PACSIN2 association, the residues important for binding are at the tips of the F-BAR dimer (Begonja et al., 2015). Because membrane binding is generally coincident with F-BAR dimer tip-to-tip oligomerization, determining if PACSIN2 can oligomerize on membranes in vivo and bind Filamin A simultaneously will be critical to understanding its physiological function. Therefore additional studies are required in order to understand the molecular basis of F-BAR domain interaction with their partners and how this promotes linkage of actin-based structures to membrane.

Summary

In this work, I have provided new insights into two aspects of CR anchoring in *S. pombe*: the PIP composition of the PM and the scaffolding roles of the Cdc15 F-BAR domain. In Chapter II, I discovered that the PIP composition of the PM promotes medial CR anchoring after its formed, representing a distinct mechanism for CR anchoring from those previously described. In Chapter III, through a combination of genetics, live-cell imaging, and development of lipid biosensors for *S. pombe*, I determined that $PI(4,5)P_2$ is the specific PIP species that promotes CR anchoring. In Chapter IV, I challenged the field's view of the function of the dual

PH domain-containing protein family by demonstrating that a family member in *S. pombe,* Opy1, does not regulate the kinase activity of the PI5-kinase Its3. However, Opy1 specifically binds $PI(4,5)P_2$ and can sequester it and cause CR anchoring defects when over-expressed. In Chapter V, I explored how the Cdc15 F-BAR domain serves as a CR anchor by examining the structure and mechanism of its interaction with the formin Cdc12. Together these studies advance our understanding of how the CR is anchored to promote the fidelity of cell division.

Chapter II

Phosphoinositide-mediated ring anchoring resists perpendicular forces to promote medial cytokinesis[1]

Introduction

To divide, many eukaryotes assemble and constrict an actin- and myosin-based contractile ring (CR) (Cheffings et al., 2016) that is anchored to the plasma membrane (PM) (Gould, 2016). Despite decades of work on how the division plane is selected and the CR assembles (Bohnert and Gould, 2011; Goyal et al., 2011; Lee et al., 2012; Pollard and Wu, 2010; Rincon and Paoletti, 2016), mechanisms of CR-PM anchoring remain incompletely understood.

Here we define a mechanism distinct from those previously reported which anchors CRs during anaphase, explaining why cells lacking *S. pombe efr3* divide asymmetrically (Chen et al., 2015). In *S. cerevisiae*, Efr3 and its partner Ypp1 form a platform at the PM for Stt4, a PI4-kinase, which regulates PIP composition and supports endocytosis (Baird et al., 2008). Similarly, human homologues of Efr3 and Ypp1 (EFR3A/B and TTC7) scaffold a PI4-kinase type-IIIα at the PM (Nakatsu et al., 2012).

We find that *S. pombe* lacking properly positioned Stt4 have altered PM PIPs. These cells form CRs in the cell middle that can then slide towards one end in a directed manner. CR

---

[1] Adapted from Chloe E. Snider*, Alaina H. Willet*, Jun-Song Chen, Göker Arpağ, Marija Zanic, Kathleen L. Gould (2017). Phosphoinositide-mediated ring anchoring resists perpendicular forces to promote medial cytokinesis. *Journal of Cell Biology* 216(10):3041-3050.

sliding in *efr3*Δ requires the type V myosin Myo51, indicating for the first time that the CR is subject to perpendicular forces in addition to being under constrictive tension (Proctor et al., 2012), and that these forces can dislodge the CR from the cell center. Thus, PM PIP composition contributes to CR anchoring, promoting proper septum positioning and ensuring accurate genome segregation.

Results and discussion

We previously observed that a high percentage of *efr3*Δ divide asymmetrically (Figure 2.1A), sometimes resulting in a "cut" phenotype (Chen et al., 2015). To determine if this is due to altered PM PIP composition, we first determined if Efr3 co-localizes with Stt4 and Ypp1 in *S. pombe* by analyzing the localization of three distinct pairs of these proteins tagged with mCherry and mNeonGreen (mNG) or GFP. Each pair co-localized on the PM in a punctate pattern (Figure 2.1B), resembling the PI kinase patch localization of the *S. cerevisiae* Stt4 complex (Baird et al., 2008). The PM enrichment of *S. pombe* Stt4 and Ypp1, but not their levels, depended on Efr3 (Figure 2.1C). Efr3 co-immunoprecipitated with Ypp1 (Figure 2.2A) and both Ypp1 and Stt4 were identified in an Efr3-TAP by LC-MS/MS analysis (Figure 2.2B) indicating that these proteins associate in *S. pombe*. To further study the influence of Stt4 on septa positioning, we attempted to construct *stt4*Δ and *ypp1*Δ, but found that these genes are essential (Figure 2.2C-D). However endogenous GFP-*stt4* displayed off-center septa indicating that although GFP-Stt4 localizes correctly to the PM, it is likely to be a hypomorphic allele (Figure 2.1A-B). These data establish that proteins of the Stt4 complex are important for medial division.

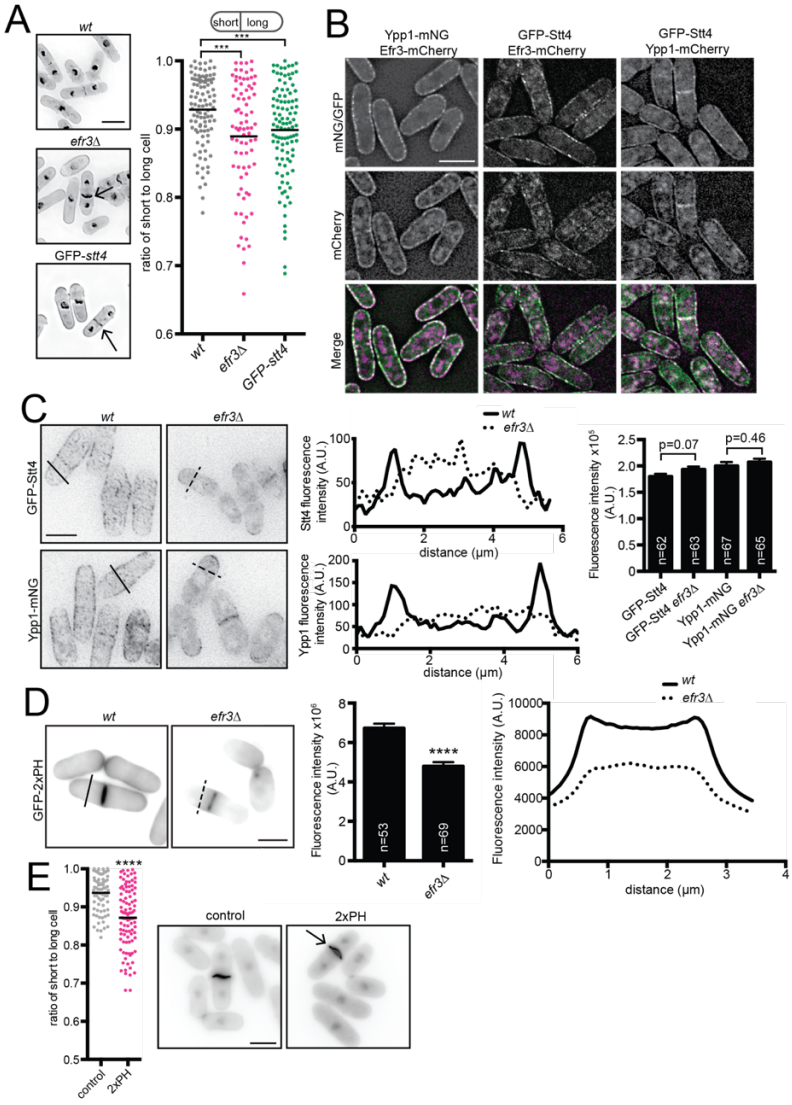

Figure 2.1. *efr3*Δ display off-center septa. (A, left) Representative images of indicated strains stained for cell wall and nuclei. Arrows indicate off-center septa. (A, right) Schematic of centered and off-centered septa classification and quantification. Individual points represent the ratio of the length of the short to long daughter cell at septation and black bars denote mean. (B) Efr3-mCherry, Ypp1-mNeonGreen (mNG), Ypp1-mCherry and GFP-Stt4. Images are of a single medial Z-slice. (C, left) GFP-Stt4 or Ypp1-mNG in either (wt) or efr3Δ. Images are Z-projections and are not identically scaled. (C, middle) Line scans of the fluorescence intensity of the solid (wt) and dotted (efr3Δ) black lines shown in left panels. (C, right) Whole-cell fluorescence intensity of the indicated strains. (D, left) Representative images of GFP-2xPH(PLCδ) localization in either wt or efr3Δ. (D, middle) Quantification of the fluorescence intensity at the division septum. (D, right) Line scans of the fluorescence intensity of the solid (wt) and dotted (efr3Δ) black lines. Data in graphs are from three biological replicates. (E) Representative images (left) and quantification (right) of cells stained for cell wall and nuclei. Arrow indicates off-center septum. ***p ≤ 0.001 ****p ≤ 0.0001; (A) one-way ANOVA or (C,D,E) Student's t-test. Error bars represent SEM. Scale bars = 5 μm.

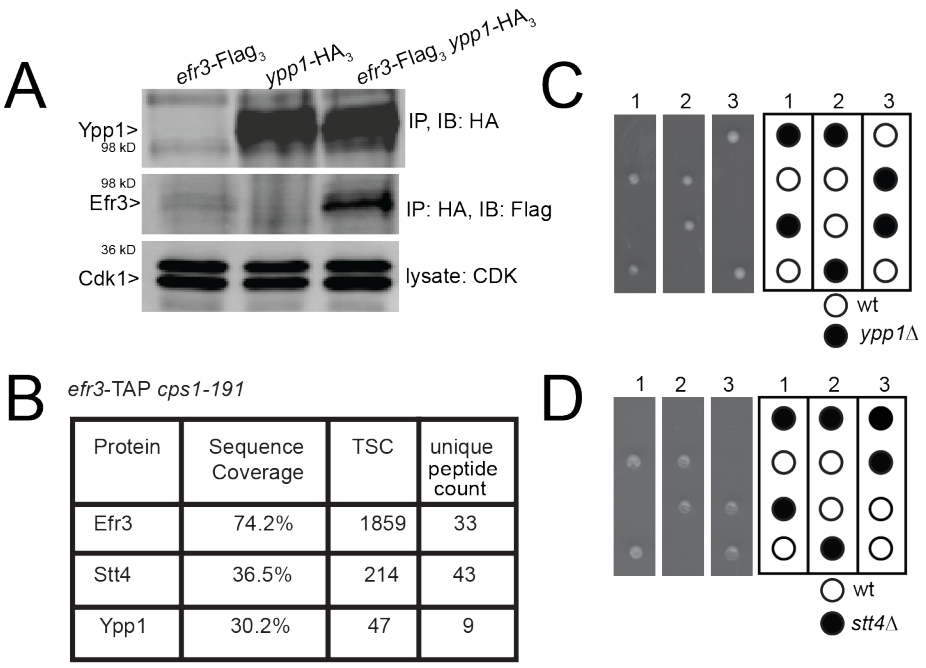

Protein	Sequence Coverage	TSC	unique peptide count
Efr3	74.2%	1859	33
Stt4	36.5%	214	43
Ypp1	30.2%	47	9

Figure 2.2. *stt4* and *ypp1* are essential in *S. pombe*. (A) Anti-HA immunoblot (IB; top) and anti-Flag immunoblot (middle) of anti-HA and anti-Flag immunoprecipitations (IPs) from the indicated strains. Anti-CDK was used as a loading control (bottom). (B) Proteins affinity purified with *efr3*-TAP *csp1–191* detected by mass spectrometry. TSC, total spectral count. (C and D) Diploids heterozygous for *ypp1::ura*$^+$ (C) or *stt4::ura*$^+$ (D) were sporulated on glutamate plates, and tetrads were picked and allowed to germinate on YE at 29°C. Pictures of plates were taken after 5 d of growth at 29°C. All viable colonies were susceptible to growth media without uracil.

Stt4 phosphorylates PM PI to produce PI4P, which can be further modified to PI(4,5)P_2. Therefore, disruption of PI4-kinases results in a reduction of both PI4P and PI(4,5)P_2 (Audhya and Emr, 2002; Baird et al., 2008; Nakatsu et al., 2012). The PI(4,5)P_2 sensor GFP-2xPH(PLCδ) (Stefan et al., 2002) was reduced at the cell cortex and the division site in *efr3*Δ compared to (Figure 2.1D), indicating that PIP PM abundance is reduced in *efr3*Δ. In accord, overexpression of GFP-2xPH(PLCδ), expected to sequester PI(4,5)P_2, resulted in off-center septa (Figure 2.1E).

We next addressed how off-center septa arise in *efr3*Δ. Because septum position is dictated by CR position (Marks et al., 1986; Marks and Hyams, 1985), we reasoned that either

the CR forms off-center or it slides from its original medial position. To distinguish between these possibilities, we imaged wildtype and *efr3*Δ expressing CR (Rlc1-GFP) and spindle pole body (Sid4-GFP) markers. In wildtype the CR formed in the cell center and maintained this position during cytokinesis (Figure 2.3A). In *efr3*Δ, the CR formed in the cell center, but slid from its original position while remaining perpendicular to the cell's long axis (Figure 2.3A-C). Temporal progression through cytokinesis was unchanged in *efr3*Δ compared to wildtype (Figure 2.4A-B). CR sliding occurred during anaphase B, after the CR formed in early mitosis, but stopped before or coincidently with CR constriction (Figure 2.3A and D). This indicates that the CR cannot slide in *efr3*Δ once septation begins, likely because septum formation locks the CR in position (Muñoz et al., 2013; Willet et al., 2015b).

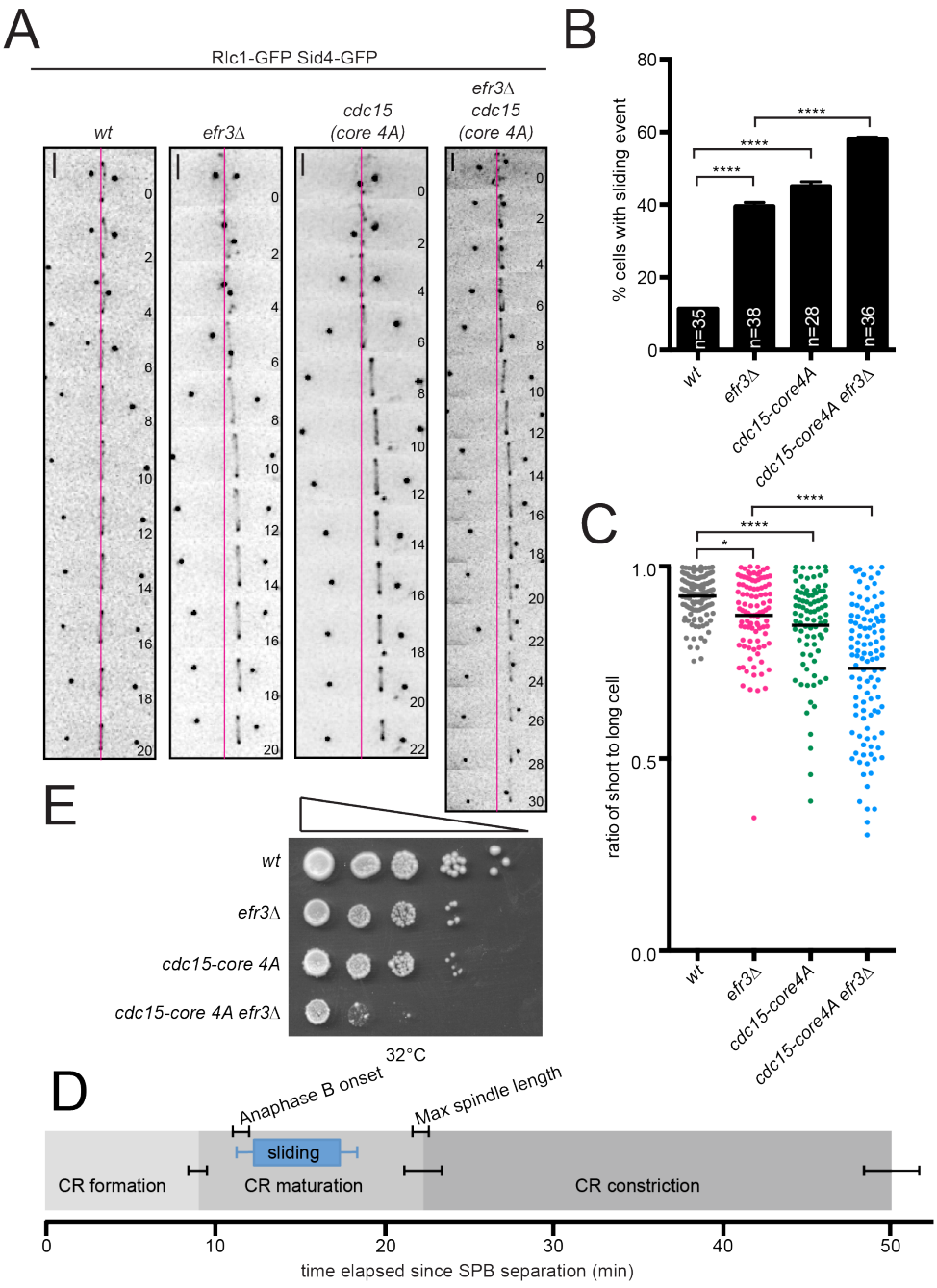

Figure 2.3. CRs slide in *efr3*Δ. (A) Live-cell imaging of indicated strains expressing Rlc1-GFP and Sid4-GFP. Magenta lines mark the cell center. Scale bars = 2 μm. (B) Quantification of the frequency of CR sliding events from (A). (C) Quantification of off-center septa. Individual points represent the ratio of the length of the short to long daughter cell at septation and black bars denote mean. (D) Average timing of CR events in *efr3*Δ determined from (A). (E) Growth assay of serial 10-fold dilutions of the indicated strains at 32°C on YE media. Error bars represent SEM. *p ≤ 0.05 ****p≤ 0.0001, one-way ANOVA.

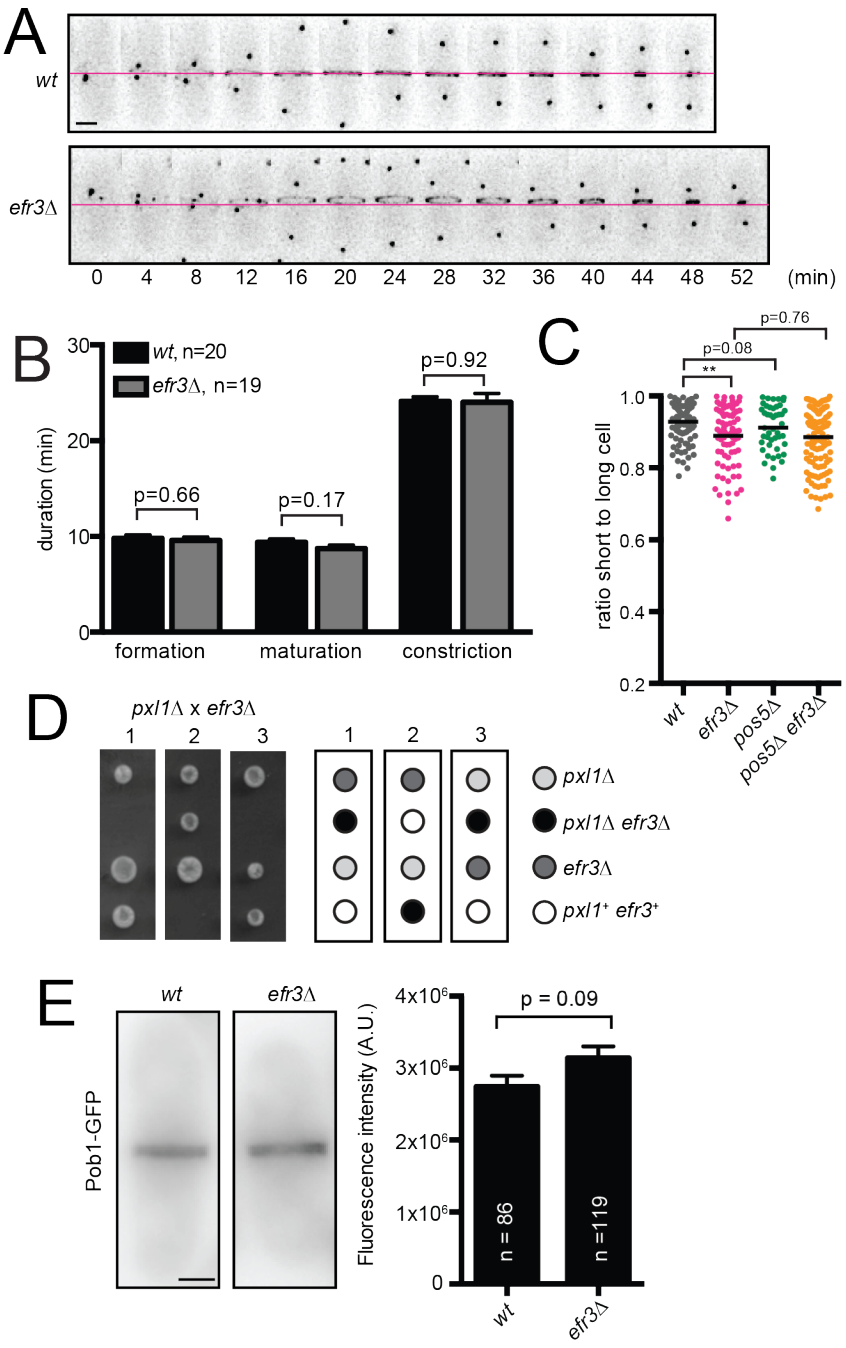

Figure 2.4. Cytokinesis kinetics are unperturbed in *efr3Δ*. (A) Timing of cytokinesis events was monitored by Rlc1-GFP and Sid4-GFP in live cells. (B) Quantification of cytokinesis kinetics in WT and *efr3Δ* from A. (C) Off-center septa were measured in indicated strains. Individual points represent the ratio of the length of short to long cells at septation, and black bars denote means. **, P < 0.01; one-way ANOVA. (D) Tetrads resulting from cross of *pxl1Δ* and *efr3Δ*. (E) Representative live-cell images (left) and quantification (right) of Pob1-GFP in WT and *efr3Δ*. Error bars represent SEM. Bars, 2 μm.

CR sliding, indicative of a CR anchoring defect, was observed when oligomerization of Cdc15's F-BAR domain was prevented or when *cdc15* expression was repressed (Arasada and Pollard, 2014; McDonald et al., 2015). To determine if Cdc15-mediated CR anchoring involves Efr3, we compared CR sliding events in *efr3*Δ and *cdc15-core 4A*, a mutation that specifically impairs membrane binding (McDonald et al., 2015). Alone, *cdc15-core 4A* displayed CR sliding. When combined with *efr3*Δ*,* the frequency of CR sliding events was increased compared to each single mutant (Figure 2.3A-B). Also, CRs slid farther in the double mutant, indicated by the lower average ratio of short to long cell at septation (Figure 2.3C), ultimately leading to growth defects (Figure 2.3E). Therefore Cdc15- and Efr3-mediated CR anchoring are independent mechanisms that maintain central CR positioning. Mutants of *pxl1* also display CR sliding (Cortés et al., 2015), however *pxl1*Δ *efr3*Δ was inviable (Figure 2.4D), suggesting that Pxl1 contributes to CR anchoring independently of Efr3. Because *efr3*Δ does not change the kinetics of cytokinesis (Figure 2.4A-B), as do defects in ß-glucan enzymes Bgs1 and Bgs4 (Davidson et al., 2016; Muñoz et al., 2013; Sethi et al., 2016), Efr3-dependent anchoring appears to be an independent mechanism from cell wall anchoring as well.

Because *efr3*Δ have reduced levels of PM PI(4,5)P_2, we hypothesized that the cortical enrichment of proteins with membrane-binding domains (F-BAR, PH, PX or C2) would be diminished in *efr3*Δ compared to wildtype. Consistent with Cdc15 acting independently of Efr3 and interacting with a wide range of anionic phospholipids (McDonald et al., 2015), we found no difference in Cdc15 CR intensity (Figure 2.5A,B). The localizations of many other membrane-binding proteins, such as Pob1 (Figure 2.4E), were also unaltered in *efr3*Δ (Figure 2.5A), suggesting that they do not rely upon PI4P or PI(4,5)P_2. However, we identified three PH domain-containing proteins with reduced PM localization in *efr3*Δ compared to wildtype. The RhoGEF Rgf1 and Cdc42 GEF Scd1 were reduced at the division site without any reduction in total protein levels (Figure 2.5C-D). Opy1, encoded by the ORF SPCPB16A4.02c, is normally enriched at the PM, but was diffusely localized in *efr3*Δ (Figure 2.5E). Opy1 contains two PH

domains and the *S. cerevisiae* ortholog, Opy1, is implicated in sensing PI4P at the PM and inhibiting the PI5-kinase Mss4 (Its3 in *S. pombe*) (Ling et al., 2012). Thus, it may be a collective reduction of several proteins at the cortex that compromises CR-PM attachment in *efr3*Δ.

Off-center septa in *S. pombe* are observed when CRs slide and also when they assemble off-center. Mid1 and Pom1 dictate CR positioning (Rincon and Paoletti, 2016); cells lacking either divide asymmetrically due to misplaced CRs (Bähler and Pringle, 1998; Bähler et al., 1998a; Chang et al., 1996; Sohrmann et al., 1996). In *mid1*Δ, CRs assemble at random positions and angles along the cortex but eventually coalesce into an orthogonal CR (Huang et al., 2008) although if CRs form within the curved cell pole of *mid1-18,* they can slide towards the tip, decreasing in diameter (Mishra et al., 2012). To test whether the Mid1 and Pom1 cues are influenced by PM composition, given that both proteins bind membrane PIPs (Celton-Morizur et al., 2004; Hachet et al., 2011), we combined *mid1*Δ or *pom1*Δ with *efr3*Δ and analyzed CR dynamics. We scored if CRs formed off-center and if fully formed CRs slid during anaphase. In our experiments, *mid1*Δ rarely formed CRs at the extreme cell tip that slid. As previously observed, *mid1*Δ and *pom1*Δ form off-center CRs but we did not detect a significant number of subsequent sliding events. Consistent with our finding that initial CR placement is not altered in *efr3*Δ, the localizations of PM-binding proteins Mid1 and Pom1 were not influenced by deletion of *efr3* (Figure 2.5A). In combination with *efr3*Δ, *mid1*Δ and *pom1*Δ CRs formed off-center *and* slid during anaphase, resulting in septa that were farther off-center than single mutants (Figure 2.6A-C). These combinations also led to significant growth defects (Figure 2.6D), most likely due to cutting of chromosomes by off-center septation.

A

Protein	Domain	Change?
Bzz1	F-BAR	no
Cdc15	F-BAR	no
Cdr2		no
Cnt6	PH	no
Fic1	C2	no
Imp2	F-BAR	no
Mid1	C2	no
Mid2	PH	no
Opy1	PH (2)	yes
Pck1	C2	no
Pck2	C2	no
Pob1	PH	no
Pom1		no
Rga2	PH	no
Rga7	F-BAR	no
Rgf1	PH	yes
Rlc1		no
Rng2		no
Scd1	PH	yes
Scd2	PX	no
Syt22	PH	no
Wsp1	PH	no

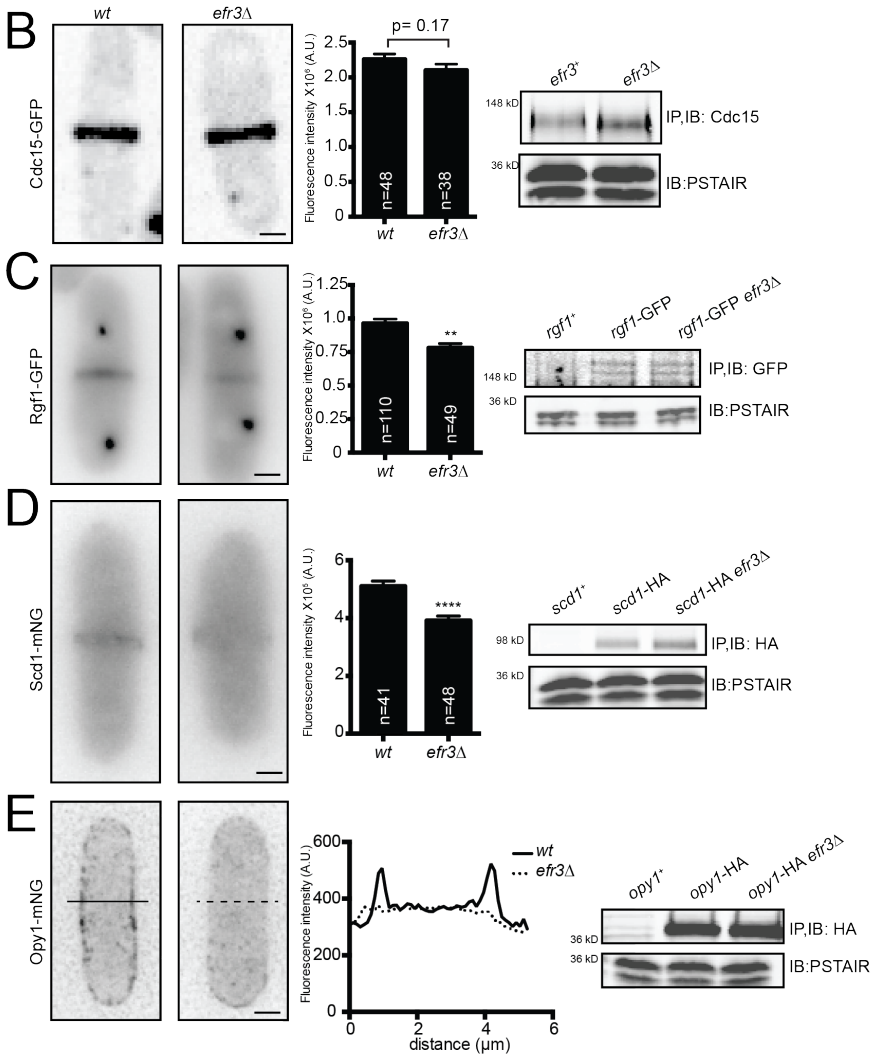

Figure 2.5. Localization of membrane-binding proteins in *efr3*Δ. (A) List of proteins tagged with GFP or mNG and screened for differences in protein localization in *efr3*Δ compared to wt. Fluorescence intensity at the division site was measured and statistically significant differences are noted. (B-E, Left) Live-cell imaging of Cdc15-GFP (B), Rgf1-GFP Sid4-GFP (C), Scd1-mNG (D), or Opy1-mNG (E) in either wt or *efr3*Δ. (B-D, Middle) Quantification of fluorescence intensity at the cell division site. (E, Middle) Line scan of fluorescence intensity. (A-E, Right) Western blots of protein levels in wt and *efr3*Δ. Measurements in (B-D) represent three biological replicates. **p ≤ 0.01 ****p≤ 0.0001, Student's t-test. Error bars represent SEM. Scale bar = 2 μm.

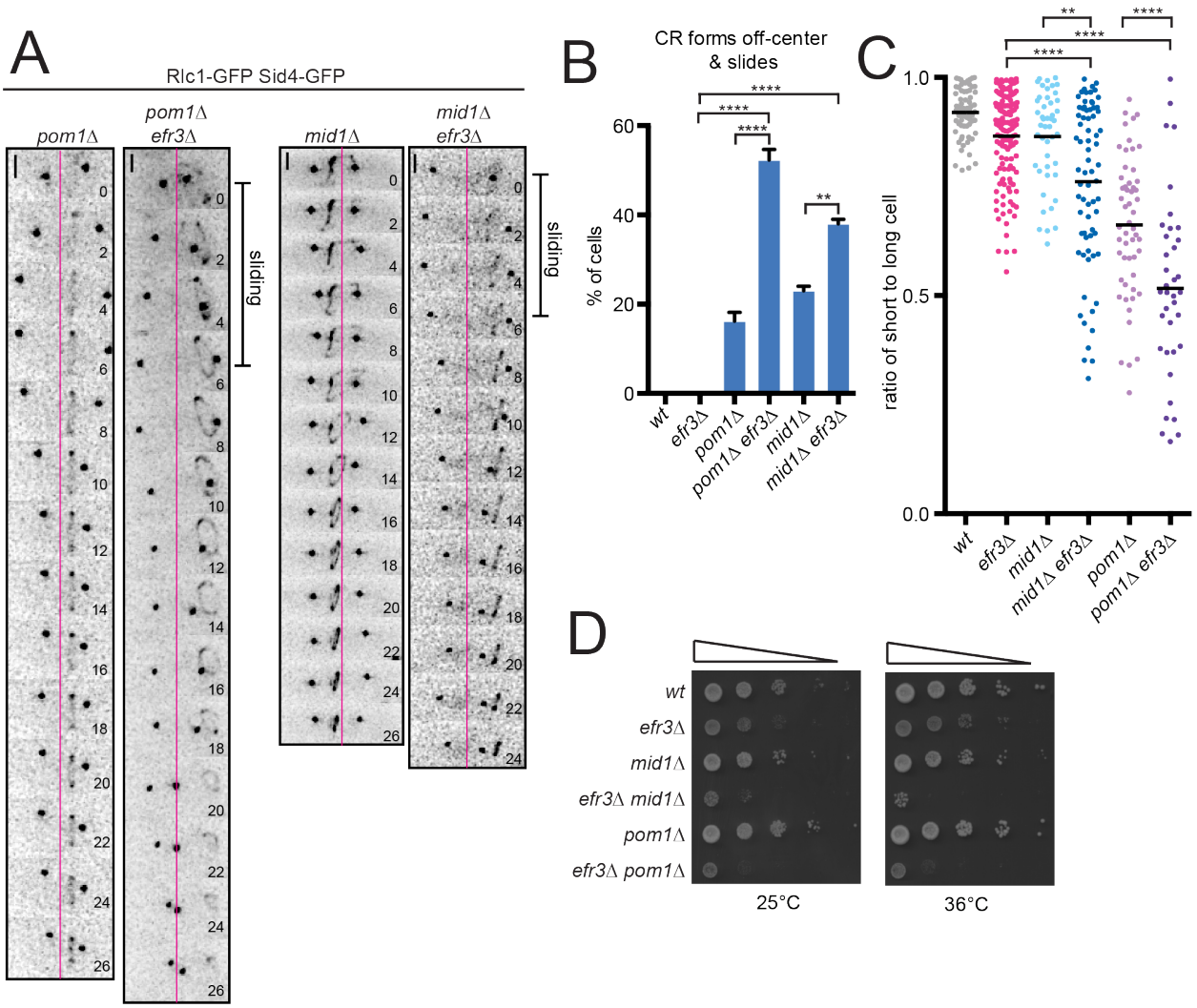

Figure 2.6. The Stt4-complex and CR positioning machinery cooperate in septum positioning. (A) Live-cell imaging of indicated strains expressing Rlc1-GFP and Sid4-GFP. Magenta lines mark the cell center. Scale bars = 2 μm. (B) Quantification of the frequency of events shown in (A) where the CR forms off center *and* slides. (C) Quantification of CR sliding. Individual points represent the ratio of the length of the short to long cell at septation and black bars denote mean. (D) Growth assay of serial 10-fold dilutions of the indicated strains at the indicated temperatures. **p ≤ 0.01 ****p≤ 0.0001, one-way ANOVA. Error bars represent SEM.

We next considered whether CR sliding events in *efr3*Δ are enabled by diminishing cell circumference from the cell middle towards one end similar to CRs in spheroplasts that move along the cortex while constricting (Mishra et al., 2013). This seemed unlikely, however, because *efr3*Δ have normal morphology (Chen et al., 2015) and CRs slide only 1-2 μm (Figure 2.3A), not approaching the region of curvature at the hemispherical cell ends (Atilgan et al., 2015). Also *pos5*Δ, which is tapered at one cell end (Hayles et al., 2013), does not have off-center septa, indicating that a CR does not automatically slide toward a tapered end (Figure 2.4C). The CR width, as a proxy of cell diameter, also does not decrease during a sliding event in *efr3*Δ, which would be expected if the circumference of the cell changed (Δ width = 0.045 μm +/- 0.039 μm (SEM, n = 19)). Further, in *pos5*Δ *efr3*Δ*,* there is no worsening of the off-center septa phenotype compared to *efr3*Δ (Figure 2.4C) and sliding CRs have no bias toward the tapered end of the cell (54% to tapered end vs 46% to non-tapered end) similar to *efr3*Δ where the CR is equally likely to slide to the old or new end of the cell (48% to old end vs 52% to new end). We conclude that CR sliding events in *efr3*Δ are not dictated by cell geometry.

Because CR sliding in spheroplasts and *cdc15* defective cells depends on type II myosins Myo2 and Myp2, respectively (Arasada and Pollard, 2014; Mishra et al., 2013), we tested if myosin-generated force is required for CR sliding in *efr3*Δ. Neither Myp2, the type I myosin Myo1, nor the type V myosin Myo52 were necessary for CR sliding in *efr3*Δ (Figure 2.7A). To test if CR sliding depends on Myo2, we attempted to combine *efr3*Δ with the temperature sensitive *myo2-E1* allele (Balasubramanian et al., 1998) but these alleles were synthetically lethal (Figure 2.8A). Instead, we used a *myo2-E1* GFP-*stt4* combination. GFP-*stt4* (GFP-*stt4* is hypomorphic) and *myo2-E1* each had off-centered septa at 32°C, and the combination resulted in more cells with off-center septa that were even farther away from center (Figure 2.8B). Live-cell imaging revealed that GFP-*stt4* CRs slid during anaphase while *myo2-E1* CRs formed off-center but did not slide (Figure 2.8C). GFP-*stt4 myo2-E1* formed CRs off-

center that then also slid along the cortex (Figure 2.8C). Thus, CR sliding in *efr3*Δ does not depend on Myo2.

In contrast, deletion of the type V myosin Myo51 eliminated the *efr3*Δ off-center septa phenotype (Figure 2.7A). CR sliding events no longer occurred in *myo51*Δ *efr3*Δ (Figure 2.7B, C) and the average ratio of short to long cell was significantly higher than in *efr3*Δ (Figure 2.7A). As expected given that Stt4 binds Efr3, the GFP-*stt4* off-center septa phenotype is also Myo51-dependent (Figure 2.8B). Interestingly, none of the myosins were necessary for CR sliding in *cdc15-core 4A* or *pxl1*Δ mutants (Figure 2.8D-E) consistent with the genetic evidence that Cdc15-, Pxl1-, and Efr3-dependent CR sliding events occur through independent mechanisms (Cortés et al., 2015). CR sliding in *cdc15* and *pxl1*Δ mutants, as well as in ß-glucan synthase mutations, may occur due to structural instability of the CR rather than a directed movement of the CR along the cortex (Arai and Mabuchi, 2002; Arasada and Pollard, 2014; Balasubramanian et al., 1998; Davidson et al., 2016; Ge and Balasubramanian, 2008; Hachet and Simanis, 2008; Laporte et al., 2011; McDonald et al., 2015; Muñoz et al., 2013; Roberts-Galbraith et al., 2009; Sethi et al., 2016; Wachtler et al., 2006).

Myo51 contains an N-terminal motor head domain and a C-terminal tail domain necessary for CR localization (Wang et al., 2014). By testing Myo51 N- and C-terminal truncations in *efr3*Δ, we found that both the N-terminal head and C-terminal tail of Myo51 are necessary for CR sliding (Figure 2.8F), suggesting that Myo51 tail binding to CR components and the ability to walk along actin filaments (Wang et al., 2014) are both required to move the CR.

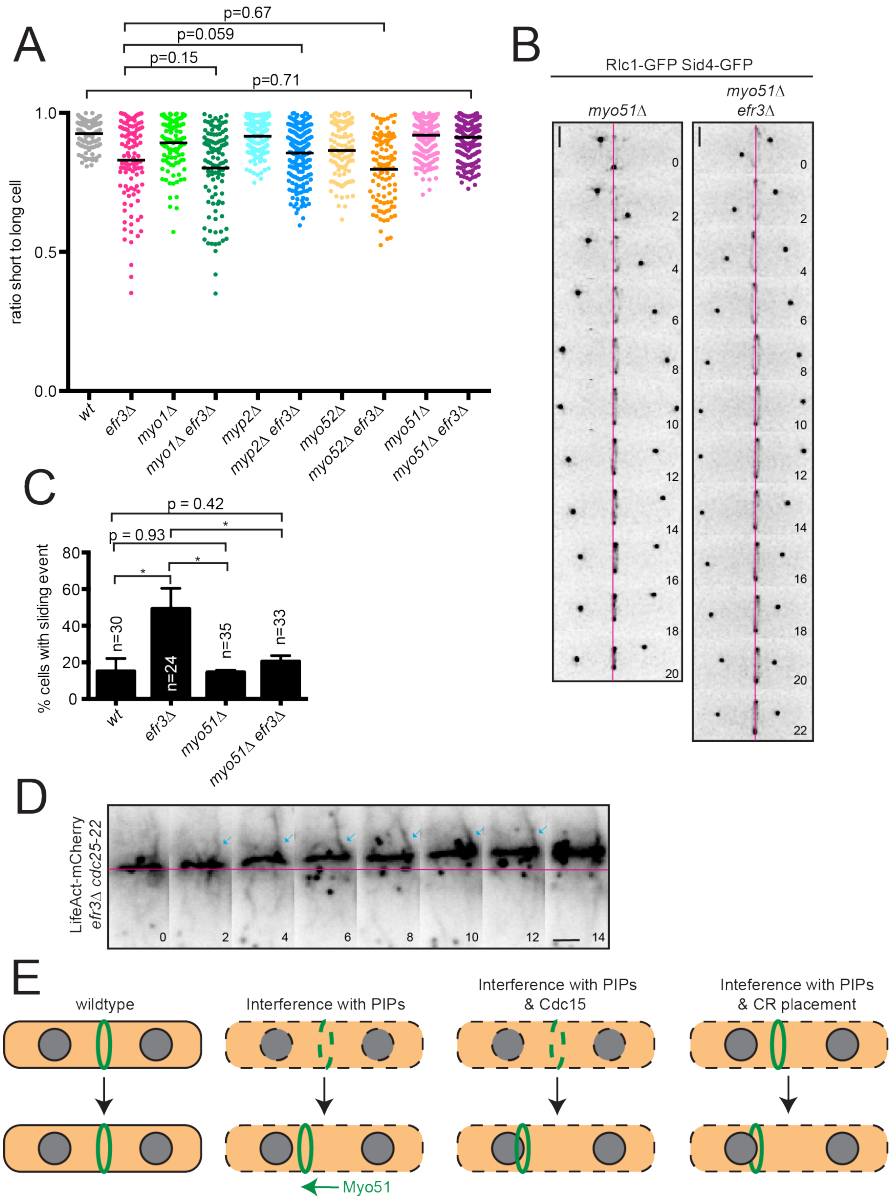

Figure 2.7. *efr3*Δ CR sliding events depend on Myo51. (A) Quantification of off-center septa. Individual points represent the ratio of the length of the short to long daughter cell at septation and black bars denote mean. (B) Live-cell imaging of indicated strains expressing Rlc1-GFP and Sid4-GFP. Magenta lines mark the cell center. (C) Quantification of the frequency of CR sliding events from (B). Error bars represent SEM. (D) Montage of time-lapse imaging of LifeAct-mCherry in *efr3*Δ *cdc25-22.* Montage is of a single Z slice and arrows indicate an actin cable in close proximity to a sliding CR. Scale bars = 2 μm. (E) Model for CR anchoring in cytokinesis. Proper PIP composition, dependent on Efr3, promotes CR anchoring. When PM lipid and CR protein composition is altered, CRs can slide. Cdc15 is an independent mechanism for CR anchoring as *cdc15* mutants combined with *efr3*Δ results in exacerbated CR sliding defects. Disruption of CR positioning machinery in combination with *efr3*Δ leads to exacerbation of off-center septa. *p ≤ 0.05, one-way ANOVA.

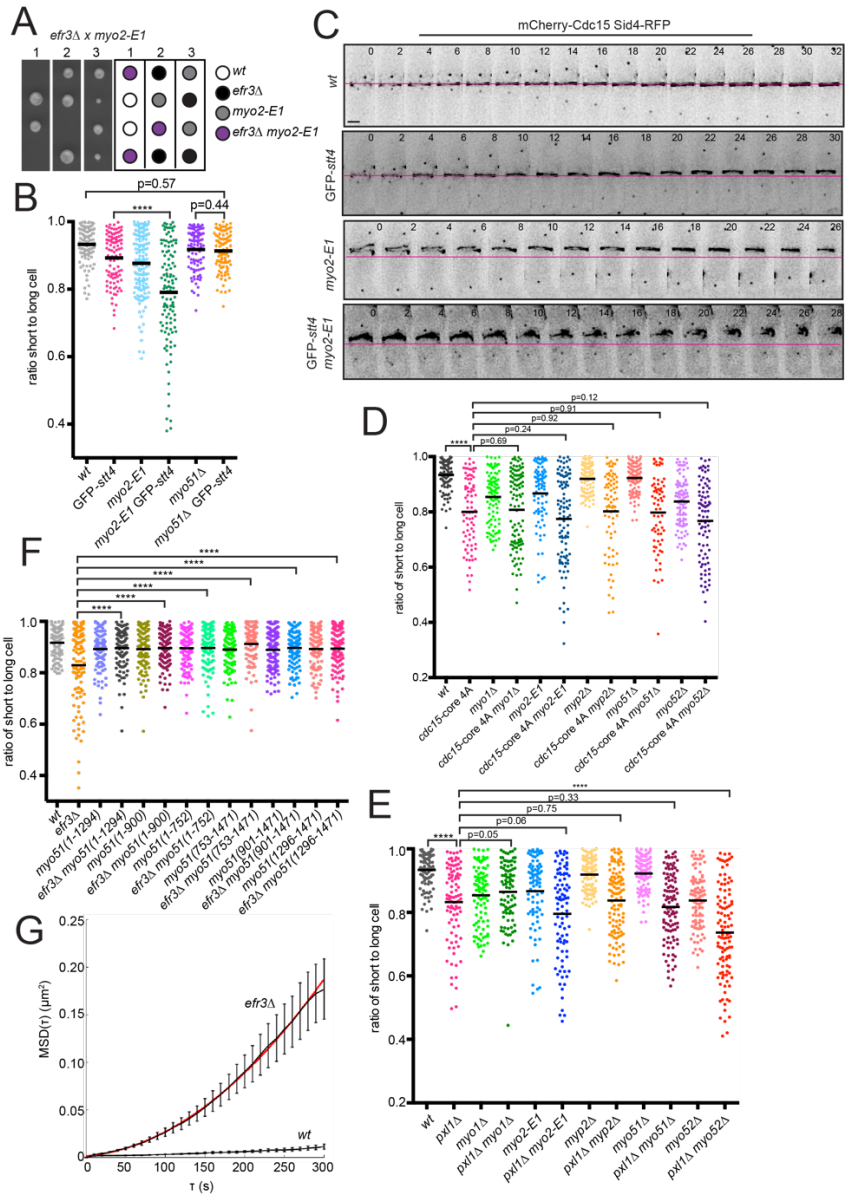

Figure 2.8. N and C termini of Myo51 are necessary for *efr3Δ* CR sliding. (A) Analysis of resulting tetrads from a cross of *efr3Δ* and *myo2-E1*. (B) Off-center septa were measured in the indicated strains. Individual points represent ratios of the length of short to long cells at septation, and black bars denote means. (C) Live-cell imaging of indicated strains expressing mCherry-Cdc15 and Sid4-RFP. Magenta lines represent the center of the cell measured in a differential interference contrast image. Bars, 2 µm. (D and E) Off-center septa were measured in WT, *cdc15–core 4A* (D), *cdc15–core 4A* with myosin mutants (D), *pxl1Δ* (E), and *pxl1Δ* with myosin mutants (E). (F) Off-center septa were measured in the indicated strains. ****, P ≤ 0.0001; one-way ANOVA. (G) MSD of cytokinetic ring position trajectories for WT (n = 34 trajectories from 17 cells) and *efr3Δ* (n = 36 trajectories from 18 cells). All trajectories are assumed to be independent realizations. The red line is the quadratic best fit to the MSD data obtained over the first 300 s (see the MSD analysis section of Materials and methods). Error bars represent SEM.

The necessity of Myo51 force generation for CR movements in *efr3*Δ provides strong evidence for the existence of forces on the CR perpendicular to the cell axis. Such forces could be involved in the splitting of CRs observed in some mutants, e.g. *pxl1*Δ (Ge and Balasubramanian, 2008) and *sbg1-3* (Sethi et al., 2016). We hypothesize that perpendicular forces are balanced in a wildtype cell and/or that CR-PM attachments are sufficient to resist these forces so that the CR remains in its central position. Further, in *efr3*Δ force imbalances may arise that cannot be stabilized, resulting in Myo51-dependent CR sliding along the cell axis. In support of this hypothesis, mean squared displacement analysis of sliding *efr3*Δ CRs shows a statistically significant drift velocity term, suggesting directed transport of the CR (Figure 2.8G, v = 1.35 nm/s, 95% confidence interval: 1.32-1.37 nm/s). No such transport term was measured for wildtype rings, which exhibit minimal changes in position over the imaging period (Figure 2.8G and Methods). A possible explanation for this behavior is that Myo51 in the CR associates with longitudinal actin cables as well as F-actin within the CR, pulling the CR along cables when PM anchoring is weakened. In support of this, Myo51 has been shown to play a role in the medial accumulation of actin cables during cytokinesis (Huang et al., 2012) and actin cables can be seen in proximity to sliding CRs in *efr3*Δ (Figure 2.7D).

Altogether, our data reveal a novel CR anchoring mechanism that depends on a conserved PM-localized PI4-kinase complex (Figure 2.7E). An ensemble of proteins sensitive to correct PM PIP composition synergize with Cdc15-, Pxl1- and cell wall-dependent anchoring to promote stable CR placement and faithful segregation of the genetic material during cell division. Given the large number of lipid-binding proteins at the cell division site of many eukaryotes, and the importance of a PI4-kinase for cytokinesis (Brill et al., 2000; Eggert et al., 2004), it is likely to be a broadly relevant factor for CR-PM adhesion.

Materials and methods

Yeast Methods

S. pombe strains were grown in yeast extract (YE). *efr3*$^{+}$, *ypp1*$^{+}$, *opy1*$^{+}$, *scd1*$^{+}$ and *rgf1*$^{+}$ were tagged at the 3' end of their ORFs with TAP: kan^{R}, Flag$_{3}$:kan^{R}, HA$_{3}$:hyg^{R}, mCherry:kan^{R}, mNeonGreen:kan^{R} or mNeonGreen:hyg^{R} using pFA6 cassettes as previously described (Bähler et al., 1998b; Wach et al., 1994). A lithium acetate method (Keeney and Boeke, 1994a) was used in *S. pombe* tagging transformations, and integration of tags was verified using whole-cell PCR and/or microscopy. Introduction of tagged loci into other genetic backgrounds was accomplished using standard *S. pombe* mating, sporulation, and tetrad dissection techniques. Fusion proteins were expressed from their native promoters at their normal chromosomal loci unless otherwise indicated.

For growth assays, cells were grown to log phase at 25˚C in YE, 10 million cells were resuspended in 1 mL of water and 10-fold serial dilutions were made. 2.5 µl of each dilution was spotted on YE plates and the plates were incubated at the indicated temperatures.
Stt4 was N-terminally tagged with GFP at the endogenous locus using a Cre-loxP method as described (Werler et al., 2003). A cassette with the sequence that encodes GFP, the *sup3-5* selection marker and a temporary promoter (nmt1) was integrated at the N terminus of the *stt4* gene. Next the selection marker and temporary promoter were removed with Cre recombinase resulting in the insertion of sequences encoding GFP at the 5'end of *stt4* under the normal promoter.

In order to express GFP-2xPH(PLCδ) in cells, the medium strength *cdc2* promoter (Carpy et al., 2014) was PCR amplified from *S. pombe* genomic DNA and GFP-2xPH(PLCδ) was PCR amplified from plasmid pRS426 (Stefan et al., 2002). The two fragments were cloned into *S. pombe* integration vector pJK148 using Gibson Assembly. This construct was linearized and inserted into the *S. pombe leu1* locus by a lithium acetate method (Keeney and Boeke, 1994a).

To overexpress GFP-2xPH(PLCδ), this sequence was PCR amplified from plasmid PRS426 and cloned into pREP81 under the *nmt81* promoter. This construct was introduced into

cells by sorbitol transformation. Cells were fixed in 70% ethanol after induction of expression for 24 hours at 32°C.

Microscopy

Live-cell images of *S. pombe* cells were acquired using a personal DeltaVision microscope system (Applied Precision) that includes an Olympus IX71 microscope, 60x NA 1.42 planApo and 100X NA 1.40 UPlanSApo objectives, a Photometrics Coolsnap HQ2 camera and softWoRx imaging software. Images were acquired at 25-29˚C and cells were imaged in YE media. Images in figures are either single slices or maximum-intensity projections of z sections spaced at 0.2-0.5 µm. Images used for quantification were not deconvolved. Other images not used for fluorescence quantification were deconvolved with 10 iterations. Time-lapse imaging was performed on cells in log phase on a YE agar pad at 32-36°C with the exception of LifeAct-mCherry *cdc25-22 efr3*Δ, where cells were shifted to 36°C for four hours and then imaged at 25°C.

Intensity measurements were made with ImageJ software (http://rsweb.nih.gov/ij/). For all intensity measurements, the background was subtracted by creating a region of interest (ROI) in the same image where there were no cells (Waters, 2009). The raw intensity of the background was divided by the area of the background, which was multiplied by the area of the ROI. This number was subtracted from the raw integrated intensity of that ROI (Waters, 2009). For CR intensity quantification, a ROI was drawn around the CR and measured for raw integrated density.

All cells were grown to log phase at 32°C before fixation. For nuclei and cell wall imaging, cells were fixed in 70% ethanol for 30 minutes before DAPI and methyl blue staining.

For quantification of ring sliding, a line was drawn through the fully formed contractile ring marked by *rlc1*-GFP using ImageJ software. Any movement of the CR away from the original line placement during the entire length of imaging was scored as a ring sliding event.

For ring sliding distances, fixed cells stained for nuclei and cell wall were imaged. The coordinates of the cell tips and septum were logged. Length of the shorter and longer cell were calculated from these coordinates and reported as a ratio.

Mean squared displacement analysis

Time-lapse images of a medial Z slice of a strain expressing a CR and spindle pole body marker were acquired every 10 seconds, registered for both DIC and fluorescent channels using ImageJ plugin Image Stabilizer (Li) and merged together to determine the position of the ring relative to the cell boundary. Cytokinetic ring positions were recorded for 17 wildtype and 18 *efr3*Δ mutant cells beginning when the CR was fully formed. Individual trajectories were obtained by reslicing the timelapse images to a 3-pixel wide line along the cell boundary and tracking the position of the ring with subpixel resolution using the ImageJ plugin TrackMate (Tinevez et al., 2017). Total absolute displacements for wildtype trajectories over a 300-second period were measured to be 83±66 nm (SD, N=34 tracks from 17 cells), which is within the spatial resolution of the imaging (pixel size 106 nm). For *efr3*Δ mutant cells, 1-dimensional position over time data were used to perform Mean-squared displacement (MSD) analysis for the first 300s of the data using MATLAB® (R2016b, The MathWorks, Natick, MA) and @msdanalyzer tool as previously described(Tarantino et al., 2014) . MSD data for *efr3*Δ mutant cells were fit by the 2nd degree polynomial function:

$$MSD(\tau) = 2D\tau + v^2\tau^2 + \sigma$$

where D is the diffusion coefficient, v is the drift velocity, and σ is the noise term. The fitting procedure yielded:

$$MSD(\tau) = \left(7.42 \times 10^{-5}\ \frac{\mu m^2}{s}\right)\tau + \left(1.82 \times 10^{-6}\ \frac{\mu m^2}{s^2}\right)\tau^2 + (1.24 \times 10^{-3}\ \mu m^2)$$

r^2=99.90%

Protein Methods and Mass Spectrometry

Cell pellets were snap-frozen in dry ice–ethanol baths. Lysates were prepared using a Fastprep cell homogenizer (MP Biomedicals). Immunoprecipitations were performed as previously described (Gould et al., 1991) in NP40 buffer for native lysates. Protein samples were resolved by SDS-PAGE and transferred to PVDF membrane (Immobilon P, EMD Millipore). Anti-HA (12CA5), anti-Flag (M2, Sigma) or anti-Cdc2 (Sigma) was used in immunoprecipitations and/or as primary antibodies in immunoblotting. Secondary antibodies were conjugated to IRDye680LT or IRDye800 (LI-COR Biosciences). Blotted proteins were detected via Odyssey (LI-COR Biosciences).

Purification of Efr3-TAP and subsequent identification of interacting proteins by mass spectrometry were performed as previously described (Chen et al., 2013; Elmore et al., 2014; Gould et al., 2004) with the following changes: a newer version of Scaffold (Scaffold v4.4.1.1) was used and the minimum peptide identification probability was changed to 95.0%.
All ANOVA statistical analyses used Tukey's post-hoc analysis.

Chapter III

Analysis of the contribution of phosphoinositides to medial septation in fission yeast highlights the importance of PI(4,5)P_2 for medial contractile ring anchoring[2]

Introduction

Although we and others have demonstrated that certain PIPs promote faithful cytokinesis, a comprehensive understanding of the specific PIP species and regulators involved has yet to be obtained in any organism. Here, we took two approaches to define the PIP species contributing to medial cytokinesis in *S. pombe*. First, we determined which PIP enzymes contribute to proper division by examining septum placement and CR dynamics in a comprehensive set of mutants. Second, we developed and validated a lipid biosensor tool set for *S. pombe*. Results from these two complementary approaches support the importance of PI(4,5)P_2 and its precursor PI4P for proper CR anchoring and thus indicate that a specialized role of PI(4,5)P_2 in cytokinesis has been conserved throughout evolution.

---

[2] Adapted from Chloe E. Snider, Alaina H. Willet, HannahSofia T. Brown, Kathleen L. Gould (2018). Analysis of the contribution of phosphoinositides to medial septation in fission yeast highlights the importance of PI(4,5)P_2 for medial contractile ring anchoring. *Molecular Biology of the Cell* 29(18):2148-2155.

Results and discussion

Deletion of the *S. pombe* PI4-kinase scaffold *efr3* results in CR anchoring defects, where the CR forms in the cell center as in wildtype but then slides away during anaphase in a myosin-dependent manner, resulting in off-center septa (Snider et al., 2017). To determine if other regulators of PIP composition contribute to medial cytokinesis, we examined septa placement in strains with mutations in genes that encode PIP kinases, phosphatases, and PIP enzyme binding partners (Figure 3.1A). As a measure of off-center septation the ratio of short to long daughter cell length at septation was calculated (Figure 3.1B).

We first examined septum placement in strains with deletions of genes encoding proteins predicted to modulate the localization or activity of PIP kinases and phosphatases (Figure 3.1B). Among these are: Opy1, a PM-localized dual PH domain-containing protein that is mislocalized in *S. pombe efr3*Δ cells and inhibits a PI5-kinase in *S. cerevisiae* (Ling et al., 2012; Snider et al., 2017); Sfk1, a predicted transmembrane scaffold of PI4KIIIα in *S. cerevisiae* and human cells (Audhya and Emr, 2002; Chung et al., 2015); Vac14, which binds both the PI(3,5)P_2-5-phosphatase Fig4 and the PI3-5-kinase Fab1 in *S. cerevisiae* and human cells (Botelho et al., 2008; Sbrissa et al., 2008); and Ncs1, a neuronal calcium sensor related protein that binds and regulates PI4-kinase Pik1 in *S. cerevisiae* (Strahl et al., 2007). Ypp1, another Stt4 PM scaffold, is essential for viability and was not tested (Baird et al., 2008; Snider et al., 2017). Septum placement was normal in all tested strains except *opy1*Δ, which had a mild off-center septa phenotype (Figure 3.1B).

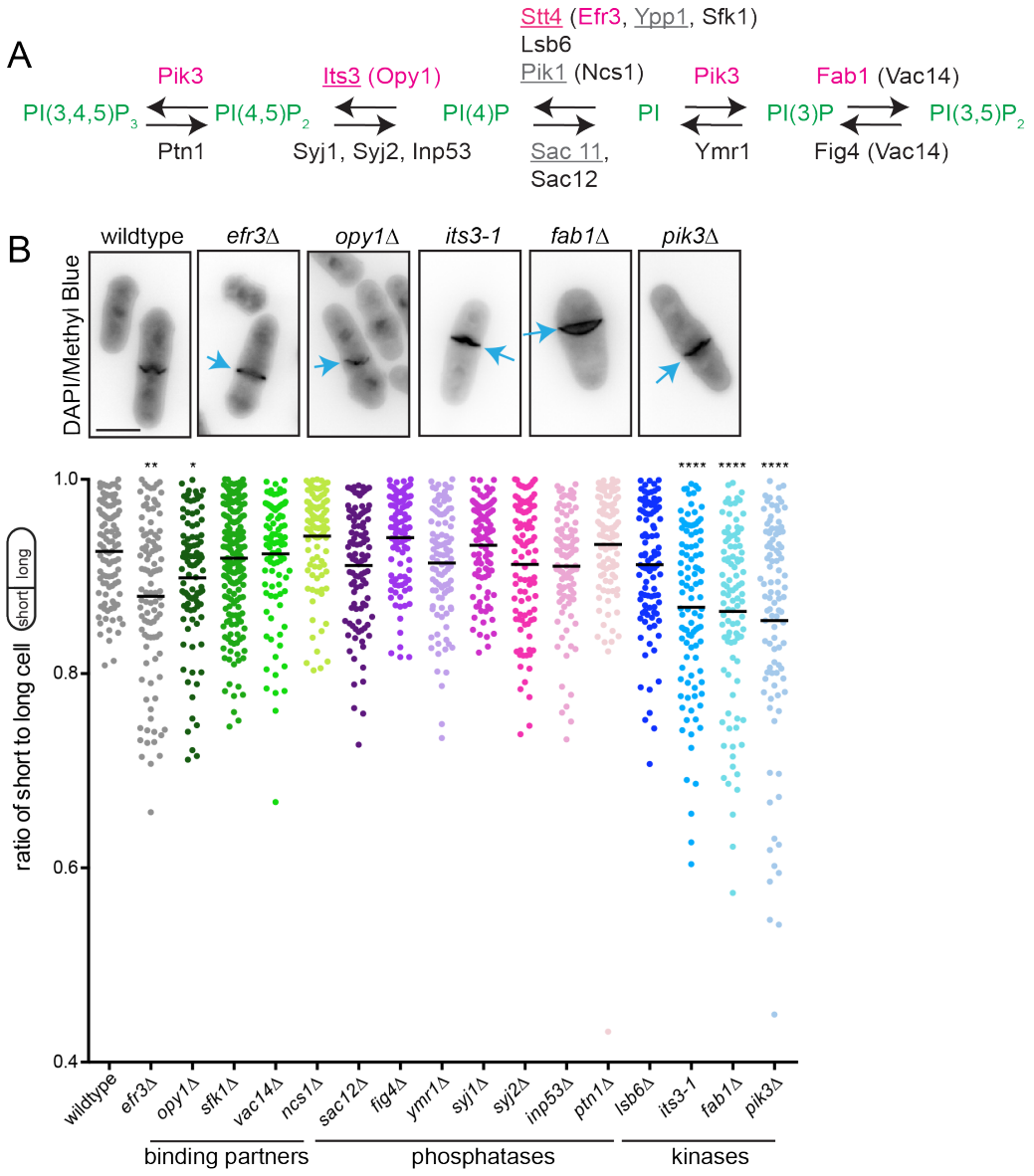

Figure 3.1. Analysis of septum placement in gene deletions of PIP regulators. (A) Schematic of the *S. pombe* phosphoinositide pathway. PIPs are green. Mutants that had off-center septa are magenta, essential genes not tested are gray, while the rest are black. Essential genes are underlined; binding partners are indicated in parentheses. (B, top) Representative images of the indicated strains stained with DAPI and Methyl Blue. Arrows indicate off center septa. (B, bottom) Quantification of septum placement in indicated strains. All cells were grown at 32ºC except *its3-1,* which was grown at 25ºC and then shifted to 32ºC for 2 hours. Black bars represent the mean. *p<0.05, **p<0.01, ****p<0.0001, one-way ANOVA. Scale bar = 5 µm.

Next, we investigated the roles of PIP phosphatases in medial septation. Single deletions of genes encoding the predicted PI4-phosphatase Sac12, the PI(3,5)P_2-5-phosphatase Fig4, the PI3-phosphatase Ymr1, the PI5-phosphatases Syj1, Syj2, and Inp53 and the PI(3,4,5)P_3-3-phosphatase Ptn1 did not result in off-center septa (Figure 3.1B), nor did combined deletions of PI(4,5)P_2-5 phosphatases (Figure 3.2D). We were unable to assay septum placement in *syj1*Δ *inp53*Δ because this combination is synthetically lethal as previously reported (Kabeche et al., 2014) (Figure 3.2E), or in the absence of the PI4-phosphatase Sac11 because *sac11* is an essential gene (Kim et al., 2010).

Lastly we assessed septum placement in mutants of PIP kinases (Figure 3.1B). There are three predicted PI4-kinases in *S. pombe*, essential Stt4 and Pik1 (Park et al., 2009; Snider et al., 2017), and non-essential Lsb6. Deletion of *lsb6* did not result in off-center septa (Figure 3.1B). There are no available temperature sensitive mutants of Stt4 or Pik1 but the hypomorphic allele *GFP-stt4* has off-center septa at elevated temperature (Snider et al., 2017), as does a temperature sensitive mutant of the essential PI-5-kinase *its3* (*its3-1*) analyzed at semi-permissive temperature (Figure 3.1B). As previously reported, deletion of the gene encoding the PI3-5-kinase Fab1 resulted in misplaced septa (Morishita and Shimoda, 2000); deletion of the gene encoding the PI3-kinase Pik3 has a similar phenotype (Figure 3.1B).

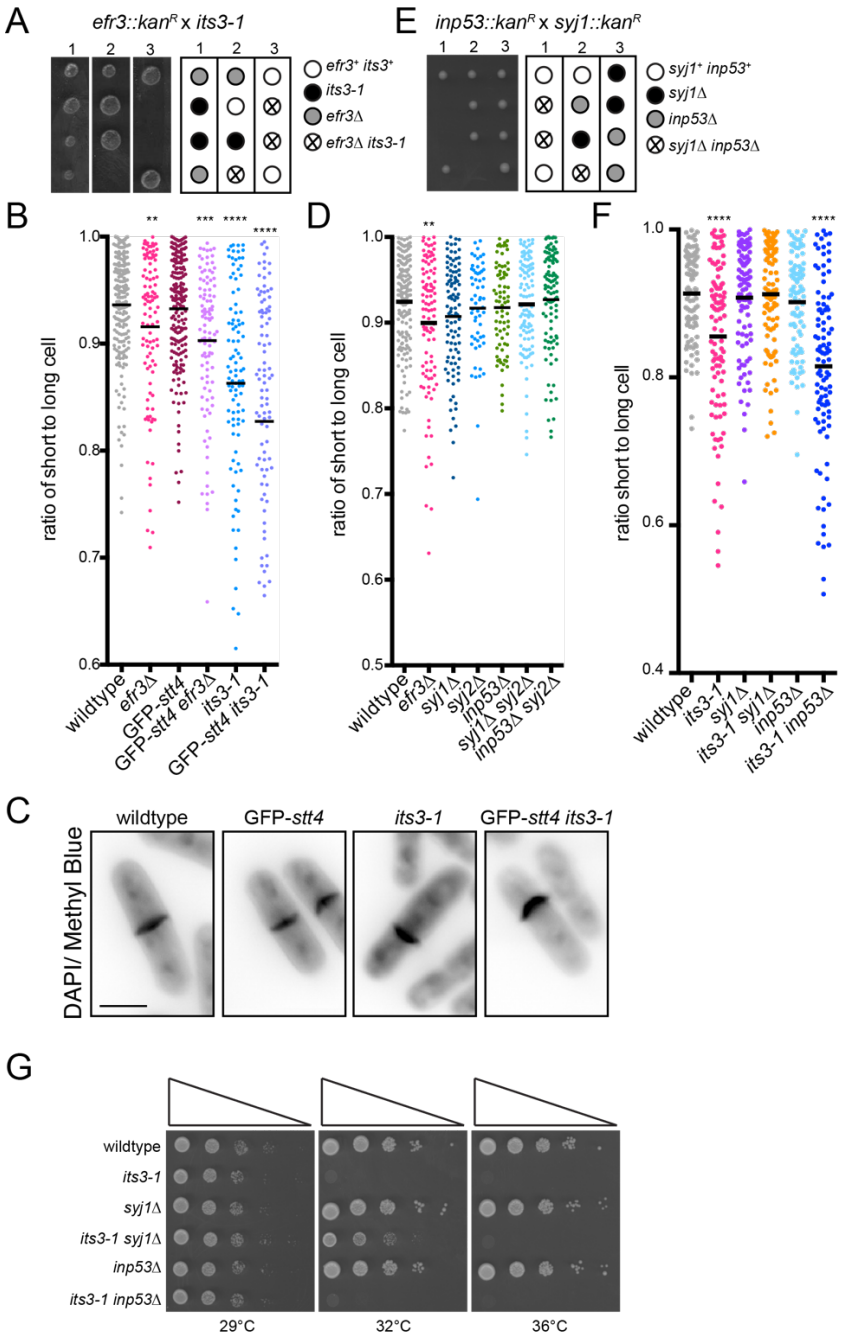

Figure 3.2. PIP kinases are important for medial division. (A) Analysis of three tetrads resulting from cross of *efr3*Δ x *its3-1*. Schematic indicates genotypes. (B, D, F) Analysis of septa placement in indicated strains. Black bars indicate mean. (C) Representative images of the indicated strains stained with DAPI and Methyl Blue. (B-D, F) Cells were grown at 25°C and shifted to 32°C for 2 hours prior to fixation. (E) Analysis of three tetrads resulting from cross of *syj1*Δ x *inp53*Δ. Schematic indicates genotypes. (G) Serial dilutions of the indicated strains at the indicated temperatures. **p < 0.01, ***p < .001 ****p < 0.0001 compared to wildtype, one-way ANOVA.

We next determined how septa form off-center in PIP kinase mutants. Though *fab1*Δ cells have misplaced CRs and septa due to off-center nuclei (Morishita and Shimoda, 2000), we wanted to determine if Pik3 and Fab1 also have a role in CR anchoring. Using live-cell time-lapse microscopy, we visualized CR dynamics in both *pik3*Δ and *fab1*Δ strains expressing CR (Rlc1-mNeonGreen (mNG)) and spindle pole body (Sid4-mNG) markers to monitor CR and mitotic events, respectively. We found that although CRs form off-center in both strains, they do not slide away from their initial position (Figure 3.3). Because $PI(3,5)P_2$ is generated by both Pik3 and Fab1, this indicates that $PI(3,5)P_2$ levels influence medial positioning of the CR, but not CR anchoring. *fab1*Δ and *pik3*Δ both have abnormally large vacuoles (Morishita and Shimoda, 2000; Takegawa et al., 1995) and it was shown in the case of *fab1*Δ that CRs form off-center due to physical displacement of the nucleus. We simultaneously observed the nucleus using Cut11-GFP (West et al., 1998) and vacuoles using Cki2-mCherry (Matsuyama et al., 2006) with live-cell time-lapse imaging. As expected, large vacuoles in *pik3*Δ prevented medial positioning of the nucleus while small vacuoles in wildtype cells did not (Figure 3.3D). To determine whether it was solely enlarged vacuoles caused by deletion of *pik3* or *fab1* rather than a reduction of $PI(3,5)P_2$ per se that causes misplaced CRs, we examined if abnormally large vacuoles arising independently of PIP misregulation cause off-center septum formation. *avt3* encodes a lysosomal amino acid transporter and *pxa1* encodes a PhoX homology associated domain protein; deletion of either gene results in abnormally large vacuoles (Chardwiriyapreecha et al., 2015; Hosomi et al., 2008). As predicted, both *avt3*Δ and *pxa1*Δ had off-center septa (Figure 3.4A). Time-lapse imaging of cells expressing Rlc1-mNG Sid4-mNG showed that *avt3*Δ formed CRs off-center that did not move from their original position (Figure 3.4B-C). In summary, large vacuoles displace nuclei from the cell center, resulting in off-center formation of the CR. This phenomenon can occur independently of PIP misregulation suggesting that the contribution of $PI(3,5)P_2$ to medial cytokinesis is likely indirect via changes to vacuole morphology.

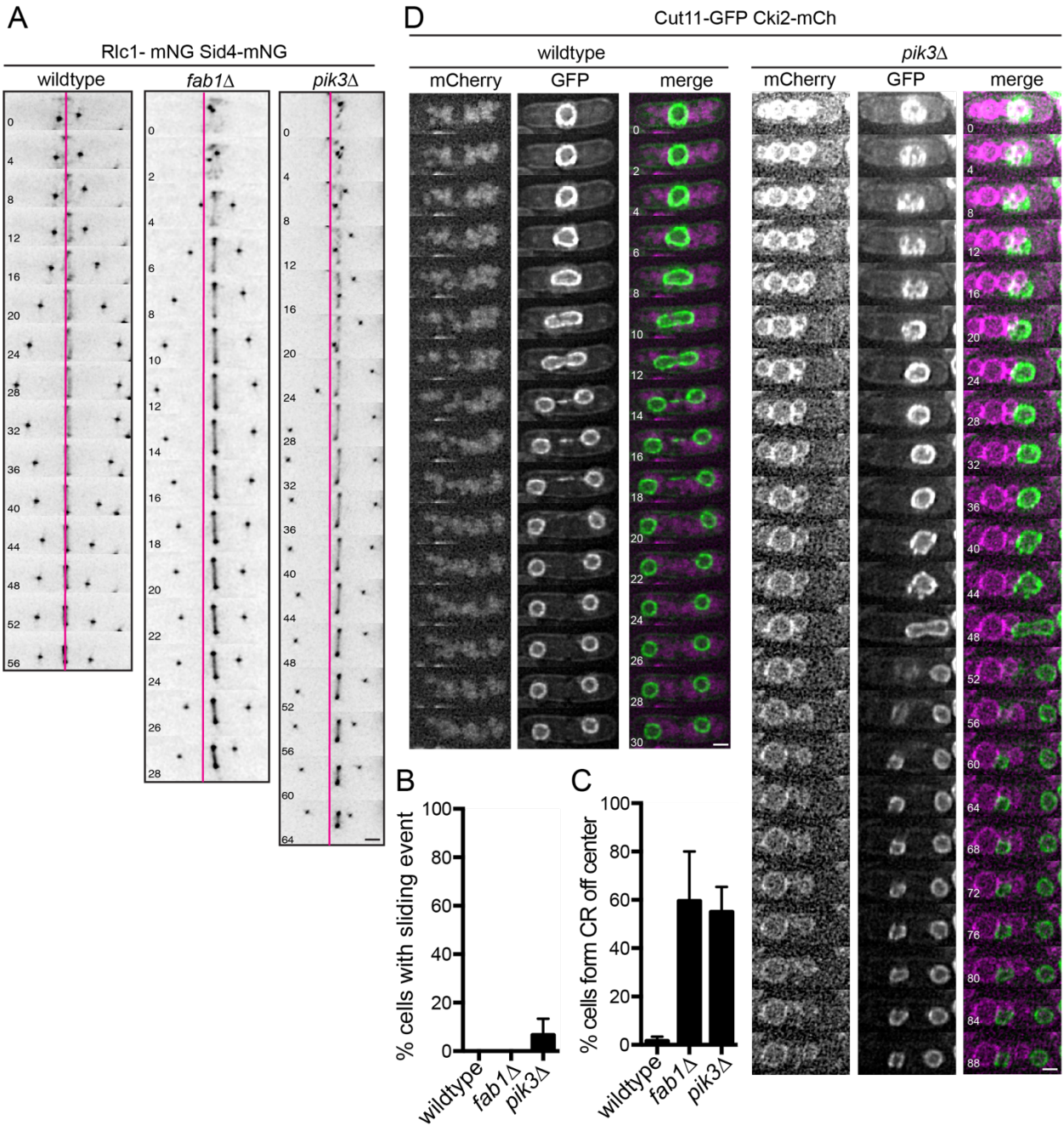

Figure 3.3. CRs form off-center in mutants of PI(3,5)P_2 regulators. (A) Montages of time-lapse imaging of the indicated strains at 25ºC. Scale bar = 2 µm. Numbers indicate minutes elapsed; magenta line indicates the cell center. (B) Quantification of CR off-center formation frequency and (C) quantification of sliding event frequency in the indicated strains. Over three independent experiments: wildtype, n=20; *fab1*Δ, n=23; *pik3*Δ, n=15. Error bars = SEM. (D) Montages of time-lapse imaging of indicated strains. Scale bar = 2 µm, numbers indicate minutes elapsed.

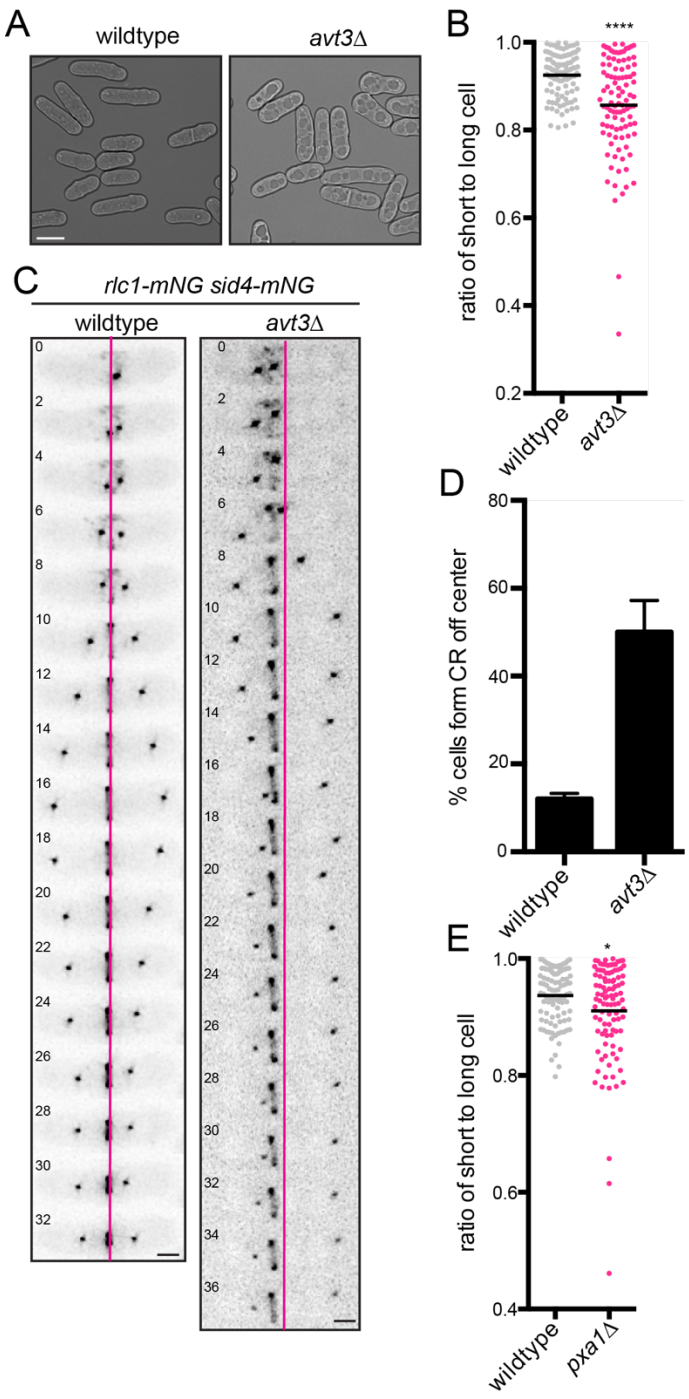

Figure 3.4. Cells with large vacuoles form the CR off center. (A) Quantification of off-center septa of indicated strains. (B) Montages of time-lapse imaging at 25°C of the indicated strains. Scale bar = 2 μm; magenta lines indicate cell center. (C) Quantification related to (B) of percentage of cells that form the CR off-center in indicated strains. Error bars = SEM. For wildtype n=34; for *avt3*Δ n=32; three experiments. * $p<0.05$; **** $p<0.0001$, Student's t-test.

We next analyzed how off-center septa originate in *its3-1* and *opy1*Δ. Using time-lapse microscopy we found that in *its3-1,* CRs formed in the cell middle and then moved from center over time, similar to the *efr3*Δ phenotype (Figure 3.5). CRs also formed normally in *opy1*Δ and consistent with its relatively mild off-center septa phenotype (Figure 3.1), only a small portion of cells displayed CR sliding events (Figure 3.5). As expected, proteins with reduced localization to the PM in *efr3*Δ (RhoGEF Rgf1-GFP, Cdc42 GEF Scd1-mNG, and dual PH domain-containing protein Opy1-mNG) were also reduced in *its3-1* while the localization of the F-BAR protein GFP-Cdc15 was unaffected (Snider et al., 2017, Figure 3.6). This indicates that Rgf1, Scd1, and Opy1 membrane-binding is PI(4,5)P_2-sensitive. Thus, only loss of Efr3 and Its3, proteins that contribute substantially to PI(4,5)P_2 generation, affect CR anchoring significantly.

To further probe the relationship between CR anchoring and changes in PM PIP levels, we developed PIP biosensors for PI4P and PI(3,4,5)P_3 that are integrated in the genome and expressed from the constitutive moderate-strength *cdc2*$^+$ promoter like the sensor we previously described for PI(4,5)P_2 (Snider et al., 2017). We measured the fluorescence intensity of these sensors bound to the membranes lining both secondary septa of dividing cells to compare PIP abundance at the PM in different mutants.

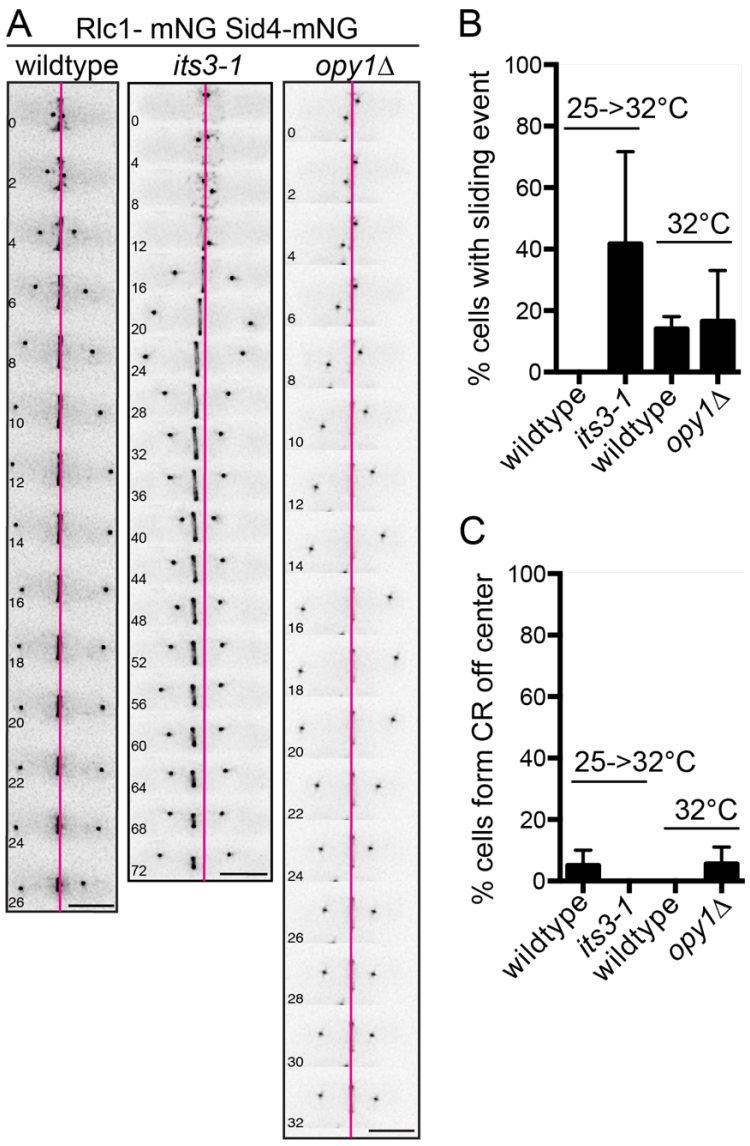

Figure 3.5. Mutants of PI(4,5)P_2 regulators display CR sliding. (A) Montages of time-lapse imaging of *opy1*Δ grown at 32ºC and *its3-1* grown at 25ºC and shifted to 32ºC for 2 hours before imaging. Scale bar = 5 µm. Numbers indicate minutes elapsed; magenta line indicates the cell center. (B) Quantification of CR sliding frequency and (C) quantification of CR off-center formation frequency in the indicated strains. For 32°C, wildtype n= 11 and *opy1*Δ n= 15; two experiments. For 25°C-32°C shift, wildtype n= 14 and *its3-1* n= 11; three experiments.

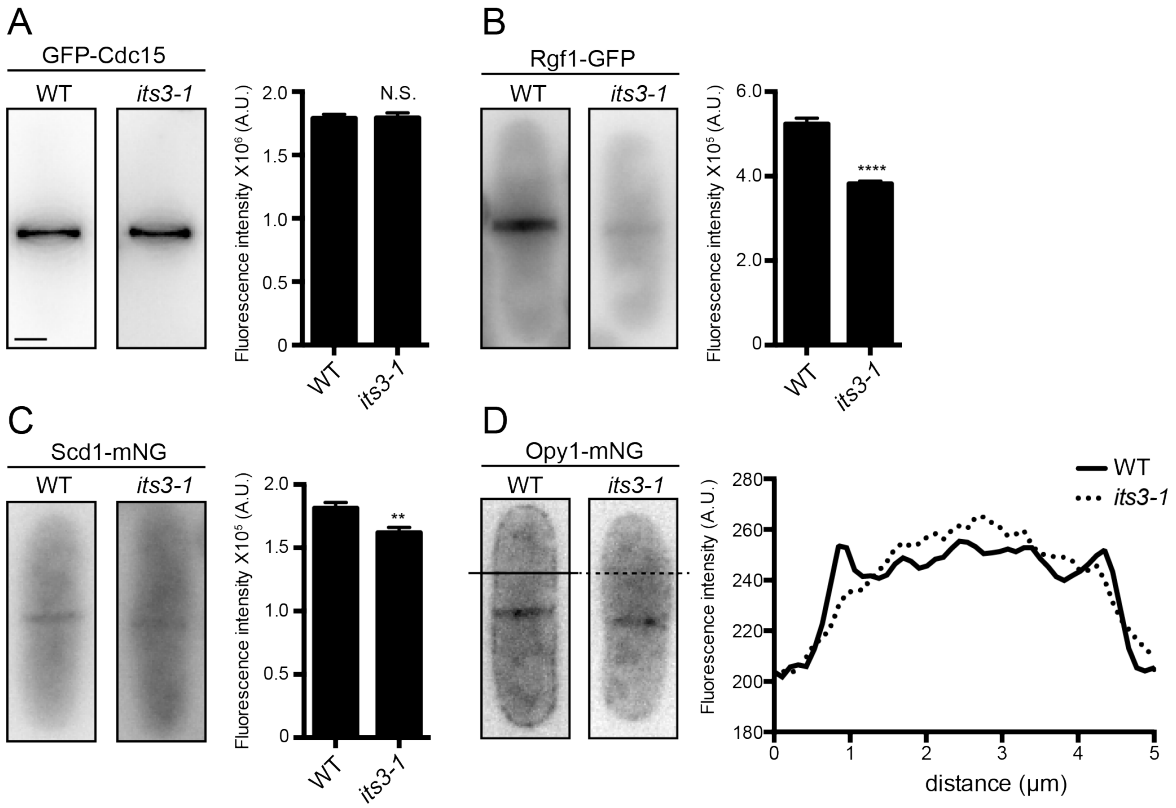

Figure 3.6. Localization of membrane-binding proteins in *its3-1*. Live cell imaging of GFP-Cdc15 (A), Rgf1-GFP (B), Scd1-mNG (C), and Opy1-mNG (D) in either wildtype or *its3-1* at 25°C. (A-C, right) Quantification of fluorescence intensity at the cell division site. (D, right) Linescan of fluorescence intensity. Measurements in A-C represent three biological replicates. Error bars represent SEM, n ≥ 74. **p<0.01, ***p<0.001, Student's t test. Bar, 2 μm.

To detect changes in PI4P levels we utilized the P4C domain from *Legionella pneumophila* SidC (Luo et al., 2015) fused to GFP. In strains with defective PI4-kinase function (*efr3*Δ, *lsb6*Δ, and *efr3*Δ *lsb6*Δ), we saw a reduction of PI4P sensor membrane localization in each single mutant compared to wildtype, and this reduction was exacerbated in the double mutant (Figure 3.7A). Consistent with this, line-scan analysis of non-septated cells revealed PI4P enrichment at the cell cortex in wildtype cells, but not in *efr3*Δ (Figure 3.8A left panel). These results validate GFP-P4C$_{SidC}$ as a suitable PI4P sensor for *S. pombe*. Using GFP-

$P4C_{SidC}$, we observed that PI4P levels are also reduced at the membranes lining the secondary septa in *its3-1* (Figure 3.7A), but this reduction was not detected at the cell cortex of interphase cells by line-scan analysis (Figure 3.8A middle panel). It is possible that there are specific defects in delivery of membrane to the division site in *its3-1* that account for the differences in PI4P at the secondary septa membranes compared to the rest of the PM. PI4P sensor localization was unaffected in *opy1*Δ (Figure 3.7A, 3.8A right), consistent with the lack of appreciable CR anchoring defects in *opy1*Δ.

To visualize $PI(3,4,5)P_3$ we used the PH domain of Akt fused to GFP (Gray et al., 1999). There was little sensor signal at the PM in wildtype cells but as previously reported using a different approach, deletion of *ptn1* (PI(3,4,5)3-phosphatase) results in enrichment of $PI(3,4,5)P_3$ at the PM (Mitra *et al.*, 2004), and the increased PM sensor signal in *ptn1*Δ validates its specificity. Because the signal in wildtype cells is so low, we used the *ptn1*Δ background to examine changes in $PI(3,4,5)P_3$ at the PM in other mutants. $PI(3,4,5)P_3$ was reduced in *efr3*Δ *ptn1*Δ and *its3-1 ptn1*Δ and interestingly increased in *opy1*Δ *ptn1*Δ at the membranes lining the secondary septa, although the reason for this increase is unknown (Figure 3.7B, 3.8B). We also noted that *pik3*Δ *ptn1*Δ cells had reduced $PI(3,4,5)P_3$ at the cell cortex, consistent with Pik3's role in generating $PI(3,4,5)P_3$ from $PI(4,5)P_2$ (Figure 3.7B).

We examined $PI(4,5)P_2$ levels using the previously described sensor, $GFP\text{-}2xPH_{Plc}$ (Snider et al., 2017). After shifting *its3-1* to a semi-permissive temperature we detected a 50% reduction in PM $PI(4,5)P_2$ compared to wildtype (Figure 3.7C, 3.8C). As expected from the lack of CR anchoring defects, no significant differences in $PI(4,5)P_2$ levels were detected in *opy1*Δ. We examined $GFP\text{-}2xPH_{Plc}$ in $PI(4,5)P_2$-5-phosphatase deletions (*syj1*Δ, *syj2*Δ, *inp53*Δ), none of which had off-center septa. The sensor localized as in wildtype in *syj1*Δ and in *syj2*Δ (data not shown), suggesting that there is redundancy between Syj1 and Syj2. However $GFP\text{-}2xPH_{Plc}$ accumulated at membranes to a greater extent in *inp53*Δ than in wildtype. Because *inp53*Δ does not have off-center septa (Figure 3.1B), we conclude that increased levels of $PI(4,5)P_2$ do not

negatively affect medial cytokinesis, while a decrease in PI(4,5)P_2 leads to CR anchoring defects.

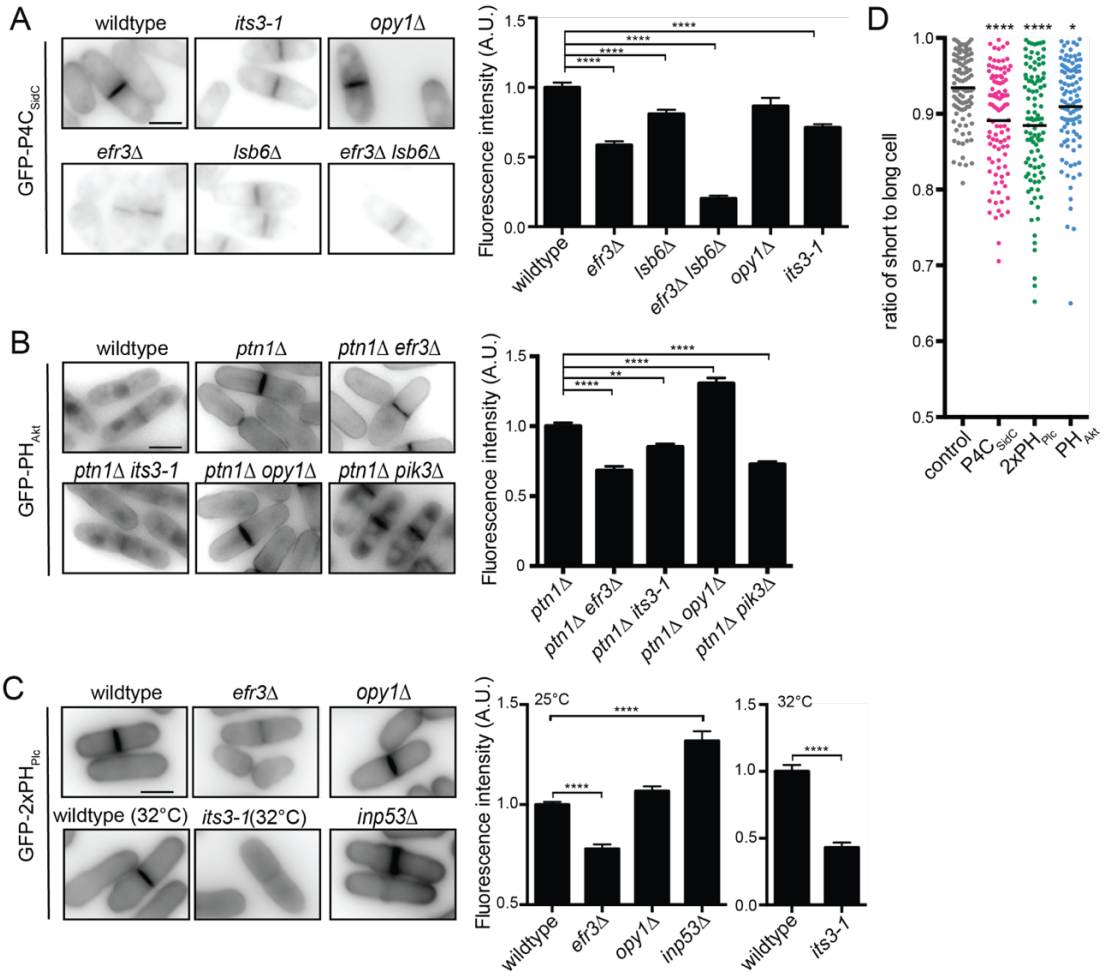

Figure 3.7. Mutants with CR anchoring defects have altered PIP composition. (Left) Representative images of strains expressing integrated (A) GFP-P4C$_{SidC}$, (B) GFP-PH$_{Akt}$, and (C) GFP-2xPH$_{Plc}$ at 25°C, with the exception of *its3-1* which was shifted to 32°C for 2 hours prior to imaging. (Right) Quantification of fluorescence intensity at secondary septal membranes of indicated strains; for all, n>40. (D) Septa placement in wildtype cells overexpressing the indicated lipid sensor or the empty vector (control). Error bars = SEM, A. U. = arbitrary units, scale bar = 5 μm. One-way ANOVA performed for all except (C) wildtype vs. *its3-1*, for which Student's t-test was performed. *p < 0.05, **p<0.01, ****p<0.0001 indicate comparison to wildtype for (A) and (C), to *ptn1*Δ for (B), and to empty vector (control) for (D).

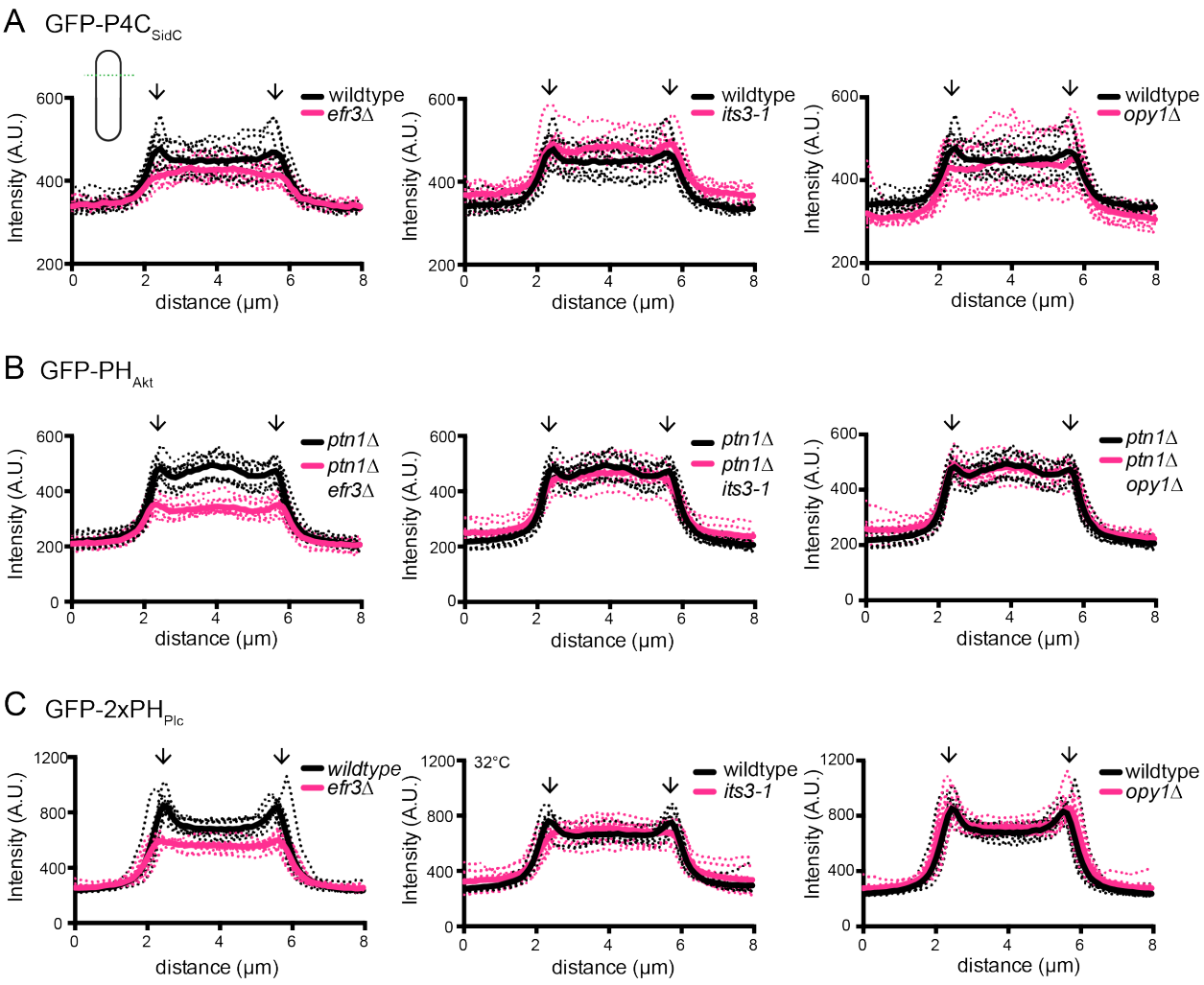

Figure 3.8. Mutants of PIP regulators have disrupted PIP composition. Linescans were drawn across the short axis of cells as indicated in the schematic in (A) where a cell is depicted by the black outline and a representative linescan by the green dashed line. Fluorescence intensity was plotted vs. distance. This analysis was completed for 10 cells (individual traces, dashed lines) of the indicated genotypes expressing (A) GFP-P4C$_{SidC}$, (B) GFP-PH$_{Akt}$, and (C) GFP-2xPH$_{Plc}$. The mean intensity profile is plotted as a solid line. Arrows indicate the position of the cell cortex. With the exception of (C middle), the same wildtype traces are plotted for each panel.

In conclusion, among the many enzymes that influence PM PIP composition, we detected a CR anchoring defect manifested by its sliding from a central position during anaphase only in *efr3*Δ and *its3-1*, indicating a specific role for PI(4,5)P_2 in CR anchoring. In accord, overexpression of PI(4,5)P_2 and PI4P sensors that are expected to sequester PI(4,5)P_2

and PI4P, respectively, result in off-center septa due to CR sliding (Snider et al., 2017) (Figure 3.7D). Interestingly, overexpression of the PI(3,4,5)P_3 sensor also causes septum misplacement, although the penetrance is low. Because Pik3 generates PI(3,4,5)P_3 (Mitra et al., 2004) and the CRs in *pik3*Δ do not slide, it is unlikely that PI(3,4,5)P_3 itself plays a significant role in CR anchoring. Perhaps this less abundant species is dephosphorylated to contribute to the PM PI(4,5)P_2 pool that promotes CR anchoring during cytokinesis. These data are consistent with the idea that only PI(4,5)P_2, the kinases that generate it, and its precursor PI4P are important for cortical CR anchoring and medial septum placement.

Our work confirmed that PI(3,5)P_2 influences medial division in *S. pombe* but most likely indirectly; reduction of PI(3,5)P_2 induces the formation of large vacuoles that prevent normal centering of the nucleus and other mutants with large vacuoles also exhibit this phenotype. The lack of CR sliding events in *fab1*Δ and *pik3*Δ indicates that PI3P and PI(3,5)P_2 do not have a role in CR anchoring, further supporting the conclusion that PI(4,5)P_2 is the only PIP species that contributes significantly to CR anchoring. PI(4,5)P_2 has a conserved role in eukaryotic cytokinesis but it remains to be determined if mediating CR anchoring to the PM is a conserved function unique to this PIP species.

Materials and methods

Yeast methods

S. pombe strains were grown in yeast extract with supplements (YES). rlc1 and sid4 were tagged at the 3′ end of their ORFs with mNG:kan^R or mNG:hyg^R using pFA6 cassettes as previously described (Bähler et al., 1998b; Wach et al., 1994). A lithium acetate method (Keeney and Boeke, 1994a) was used in S. pombe tagging transformations, and integration of tags was verified using whole-cell PCR and/or microscopy. Introduction of tagged loci into other genetic backgrounds was accomplished using standard S. pombe mating, sporulation, and

tetrad dissection techniques. Deletions of the sfk1 and ncs1 genes were accomplished as previously described (Chen et al., 2015).

Constitutively expressed lipid sensors were constructed as previously described (Snider et al., 2017). Briefly, the *cdc2* promoter, sequences encoding GFP, and the desired sensor were PCR amplified and cloned into pJK148 using Gibson assembly. GFP-P4C was PCR amplified from a plasmid provided by the Mao lab (Luo et al., 2015) and AKT-PH fragment was PCR amplified from plasmid #67301 from Addgene (Kawano et al., 2015). These constructs were linearized and inserted into the *S. pombe leu1* locus by a lithium acetate method (Keeney and Boeke, 1994a).

To overexpress $P4C_{SidC}$, PH_{Akt}, and $2xPH_{Plc}$, sequences encoding each were cloned into pREP1 (Maundrell, 1993). The resulting plasmids were introduced into cells by sorbitol transformation. Cells were fixed in 70% ethanol after induction of expression for 24 hours at 32°C.

Microscopy Methods

Live-cell images of *S. pombe* cells were acquired using a Personal DeltaVision (Applied Precision) that includes a microscope (IX71; Olympus), 60× NA 1.42 Plan Apochromat and 100× NA 1.40 U Plan S Apochromat objectives, fixed and live-cell filter wheels, a camera (CoolSNAP HQ2; Photometrics), and softWoRx imaging software (Applied Precision). z sections were spaced at 0.2-0.5 μm. Images were acquired at indicated temperature and cells were imaged in YES media. Time-lapse imaging was performed on cells in log phase on a YES agar pad at 25-32°C. Images were deconvolved with 10 iterations.

Intensity measurements were made with Fiji software (Schindelin et al., 2012). For all intensity measurements, the background was subtracted by creating a region of interest (ROI) in the same image where there were no cells (Waters, 2009). The raw intensity of the background was divided by the area of the background, which was multiplied by the area of the ROI. This

number was subtracted from the raw integrated intensity of that ROI (Waters, 2009). For intensity quantification of the membranes lining the secondary septa, sum projections were analyzed. An ROI was drawn around the septum and measured for raw integrated density. For linescans the middle z-slice was analyzed. In Fiji, a line was drawn across the short axis of non-septated cells and the fluorescence intensity profile was plotted vs. distance. All images used for quantification were not deconvolved.

For quantification of off-center septa, all cells were grown to log phase at 32°C before fixation unless otherwise indicated (*its3-1* was grown to log phase at 25ºC and then shifted for 2 hours to 32ºC). For overexpression of lipid sensors, cells were grown in the absence of thiamine for 24 hours to induce expression from the *nmt1* promoter. For nuclei and cell wall imaging, cells were fixed in 70% ethanol for at least 30 min before DAPI and Methyl Blue staining. To quantify off-center septa, the coordinates of the cell tips and septum were logged. Lengths of the shorter and longer cell were calculated from these coordinates and reported as a ratio. For quantification of CR sliding, a line was drawn through the fully formed CR marked by Rlc1-mNG using Fiji software. Any movement of the CR away from the original line placement during the entire length of imaging was scored as a ring sliding event.

Statistics

All ANOVA statistical analyses were followed by Tukey's post-hoc test.

Chapter IV

Fission yeast Opy1 is an endogenous PI(4,5)P_2 sensor that binds to the phosphatidylinositol 4-phosphate 5-kinase Its3[3]

Introduction

Phosphoinositides (PIPs) are a family of lipids that are essential for signaling, membrane identity, and diverse cellular processes involving membrane rearrangements (reviewed in (Schink et al., 2016)). The different membranes in the cell are each comprised of a unique PIP composition and these differences are driven and regulated by the activities of numerous PIP kinases, phosphatases, and lipases (Dickson and Hille, 2019). Despite decades of study, our understanding of how each of these enzymes is coordinated in space and time to control PIP levels and their downstream effectors remains incomplete.

Phosphatidylinositol(4,5)-bisphosphate (PI(4,5)P_2) is the most abundant PIP species in the plasma membrane (PM). Proper PM PI(4,5)P_2 promotes cell division in multiple eukaryotic organisms (Field et al., 2005; Snider et al., 2018; Snider et al., 2017; Wong et al., 2005). In *Schizosaccharomyces pombe,* PI(4,5)P_2 is important for anchorage of the cytokinetic ring (CR) in the cell center that in turn promotes medial division and avoids damage to the dividing

---

[3] Adapted from Chloe E. Snider, Alaina H. Willet, HannahSofia T. Brown, Jun-Song Chen, Joshua M. Evers, Kathleen L. Gould (2020). Fission yeast Opy1 is an endogenous PI(4,5)P_2 sensor that binds to the phosphatidylinositol 4-phosphate 5-kinase Its3. *Journal of Cell Science* 133(23):jcs247973.

genome (Snider et al., 2018; Snider et al., 2017). PM PI(4,5)P_2 is produced in *S. pombe* by the PI4-kinase Stt4, which is localized to the PM by its binding partners, Efr3 and Ypp1 (Snider et al., 2017). There it converts phosphatidylinositol (PI) to phosphatidylinositol-4-phosphate (PI4P), which is subsequently phosphorylated by the PI5-kinase Its3 to generate PI(4,5)P_2. Loss of function of Stt4 complex members (*efr3*Δ, GFP-*stt4*) or Its3 (*its3-1)* results in reduced PM PI(4,5)P_2, CR sliding events, and subsequent off-center septation (Snider et al., 2018; Snider et al., 2017), underscoring the importance of PM PI(4,5)P_2 for eukaryotic cytokinesis.

In our effort to understand which PM components modulate CR anchoring and are affected by *efr3*Δ and *its3-1*, we identified Opy1. Opy1 localizes to the cell cortex in punctae, but upon reduction of PM PI(4,5)P_2 in *efr3*Δ or *its3-1*, it becomes primarily cytosolic (Snider et al., 2018; Snider et al., 2017). Although Opy1 localization to the PM is sensitive to PIP content, *opy1*Δ cells do not display CR sliding (Snider et al., 2018). Additionally, we demonstrated using lipid biosensors that PI4P and PI(4,5)P_2 PM levels in *opy1*Δ are indistinguishable from wildtype (Snider et al., 2018). Together, these results indicated that *S. pombe* Opy1 is not a major CR-PM anchor nor a regulator of PIP composition.

Opy1 is the presumptive ortholog of *S. cerevisiae* Opy1 based on protein sequence similarity. Both *S. cerevisiae* and *S. pombe* Opy1 proteins contain one N- and one C-terminal pleckstrin homology (PH) domain (Figure 4.1A) (Ling et al., 2012). PH domains are common in eukaryotic proteomes and are well-appreciated to be potential membrane-binding modules. Although once thought to be exclusively PIP-binding domains, only a small fraction of PH domains bind a particular PIP with specificity and not all PH domains bind membranes (Lemmon, 2007). A function was proposed for each of the two *S. cerevisiae* Opy1 PH domains in regulation of the PI5-kinase and Its3 ortholog, Mss4. According to this model, Opy1 acts as a coincidence detector by binding PI(4,5)P_2 at the PM through its C-terminal PH domain and simultaneously binding Mss4 to inhibit its kinase activity when PI(4,5)P_2 levels are high (Ling et al., 2012). Although this

is an appealing model, it has not yet been demonstrated that Mss4 and Opy1 interact directly in vitro or that Mss4 kinase activity is diminished in the presence of Opy1.

Because deleting *S. pombe opy1* did not result in CR sliding or changes to PIP levels (Snider et al., 2018), we set out to compare features of *S. pombe* Opy1 with those of *S. cerevisiae* Opy1 (Ling et al., 2012) to better understand the generality of dual PH domain containing protein function. Our findings suggest that these proteins have evolved unexpectedly distinct properties, suggesting these proteins may have organism-specific functionality.

Results and discussion

We tested if *S. pombe* Opy1 binds membrane directly using liposome co-pelleting assays. Opy1, produced and purified from bacteria, co-pelleted with Folch fraction liposomes, indicating that it can directly bind membrane in vitro (Figure 4.1B). We then generated GST fusions to Opy1 fragments including the N-terminal PH domain (aa1-128; PH1) or the C-terminal PH domain (aa208-end; PH2). PH1 robustly interacted with liposomes while PH2 showed no significant interaction with liposomes (Figure 4.1C). We next tested if full-length Opy1 binds specific PIPs using co-pelleting assays with liposomes of defined composition. Opy1 interacted with $PI(4,5)P_2$-containing liposomes, but displayed little to no interaction with liposomes containing PI4P or $PI(3,4,5)P_3$ (Figure 4.1D-E). Opy1's specificity for $PI(4,5)P_2$ can explain the loss of Opy1 PM-targeting in both *efr3*Δ and *its3-1* mutants, in which PM $PI(4,5)P_2$ levels are reduced (Snider et al., 2018; Snider et al., 2017).

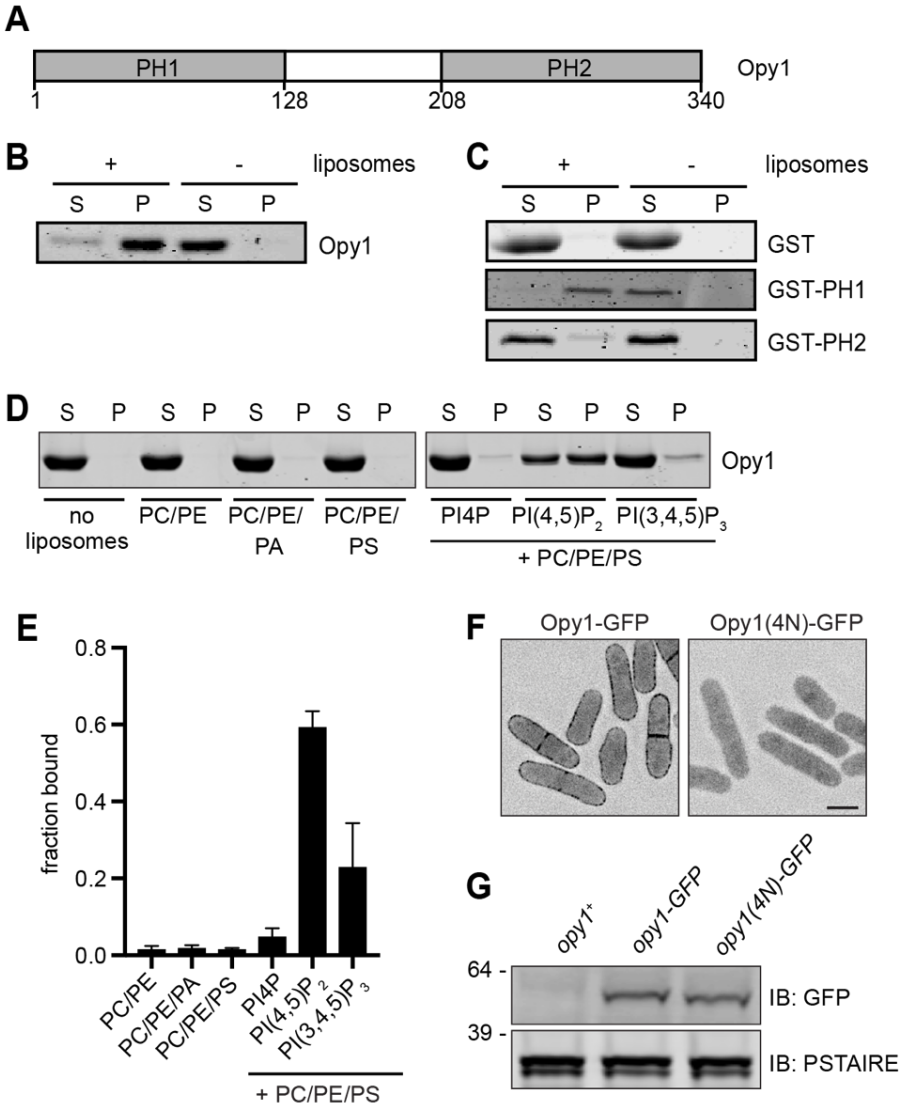

Figure 4.1. Opy1 binds PI(4,5)P_2-containing membranes. (A) Schematic of Opy1, drawn to scale. Amino acid numbers are indicated below the schematic. PH1 and PH2 indicate pleckstrin homology domains. (B) Co-pelleting assay with Folch fraction liposomes and full length Opy1. (C) Co-pelleting assay with GST and GST fusions of PH1 (aa1-128) and PH2 (aa208-340). (D) Co-pelleting assay of full length Opy1 with liposomes of indicated compositions. (E) Quantification of the mean fraction of Opy1 bound to liposomes from two experiments related to D. Error bars represent SEM. S = supernatant, P = pellet. (F) Live-cell imaging of Opy1-GFP and Opy1(4N)-GFP. Scale bar = 5 μm. (G) Western blot showing expression of indicated proteins in cell lysates. PSTAIRE was used as a loading control. Numbers on the left indicate position of molecular weight markers. IB = immunoblot. Experiments in B-G were repeated twice with similar results.

We noted significant sequence similarity between Opy1 PH1 and the N-terminal PH domain of the mammalian dual-PH domain protein pleckstrin (Figure 4.2A), which has a $PI(4,5)P_2$ binding pocket that confers pleckstrin's specificity for $PI(4,5)P_2$ in vitro and is required for targeting to the plasma membrane in cells (Harlan et al., 1994; Harlan et al., 1995; Ma et al., 1997). We mutated the analogous residues in *opy1* (K34N, K35N, K42N, K43N = *opy1(4N))* and examined the localization of endogenously tagged Opy1-4N-GFP in cells using fluorescence microscopy. Opy1-4N did not localize to the plasma membrane even though it is expressed at comparable levels to wildtype (Figure 4.1F-G), indicating that the PH1 domain is required for Opy1 PM targeting, and that it may employ a similar mechanism to that of pleckstrin for binding $PI(4,5)P_2$. We next visualized endogenously produced Opy1 fragments fused to GFP to determine whether membrane binding capacity in vitro equated with PM localization. The localizations of PH1-GFP and PH2-GFP that either included the linker between the PH domains (PH1: aa1-220 and PH2: aa123-end, Figure 4.2B) or excluded it (PH1: aa1-128 and PH2: aa208-end, Figure 4.2C) were compared to that of full length Opy1-GFP. We found that none of the truncations localized to the PM, although all of the truncations were produced, as determined by immunoblotting (Figure 4.2D). Thus, despite PH1 conferring membrane binding in vitro and being required for PM localization in vivo, neither PH domain is sufficient to target Opy1 to the PM in vivo, indicating that there is another layer of regulation governing stable PM localization of Opy1.

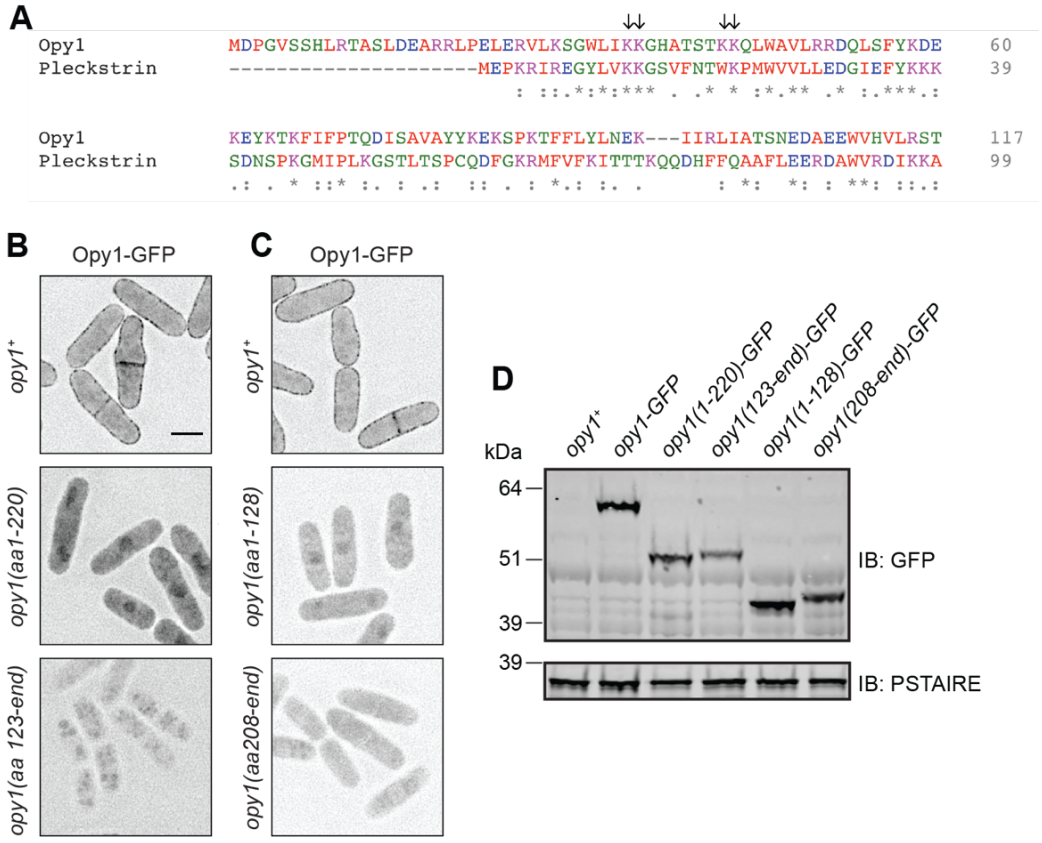

Figure 4.2. Localization of Opy1 N- and C-terminal PH domains. (A) Sequence alignment of residues 1-99 of *H. sapiens* pleckstrin and residues 1-117 of *S. pombe* Opy1 generated by Clustal Omega (Madeira et al., 2019). Asterisks denote residues that are conserved; colons denote groups with strongly similar qualities; periods denote groups with weakly similar qualities. Red = small + hydrophobic residues; blue = acidic residues; magenta = basic residues; green = hydroxyl + sulfhydryl + amine + G residues. Arrows indicate the Opy1 residues implicated in PI(4,5)P_2 binding (Harlan et al., 1995). (B-C) Representative live-cell images of Opy1-GFP in indicated genotypes. Scale bar = 5 µm. (D) Western blot of the indicated GFP-fusions, IB = immunoblot.

S. cerevisiae Opy1 associates with both PI(4,5)P_2 and the PI5-kinase Mss4 (Ling et al., 2012). To test if *S. pombe* Opy1 binds the PI5-kinase Its3, we first performed a large-scale purification of Opy1-TAP from *S. pombe* and identified associated proteins by 2D liquid chromatography-tandem mass spectrometry (LC-MS/MS). After background subtraction, Its3 was the top hit and the only PM protein identified in the top ten, indicating that Opy1 and Its3

associate in vivo (Figure 4.3A). To test if Opy1 and Its3 interact directly, we produced and purified both proteins recombinantly and performed in vitro binding assays. We found that MBP-Its3 immobilized on resin directly pulled down GST-Opy1, and that this interaction was mediated by PH1 (Figure 4.3B). Thus, *S. pombe* PH1 binds both $PI(4,5)P_2$ and PI5-kinase. The function of PH2 remains unknown.

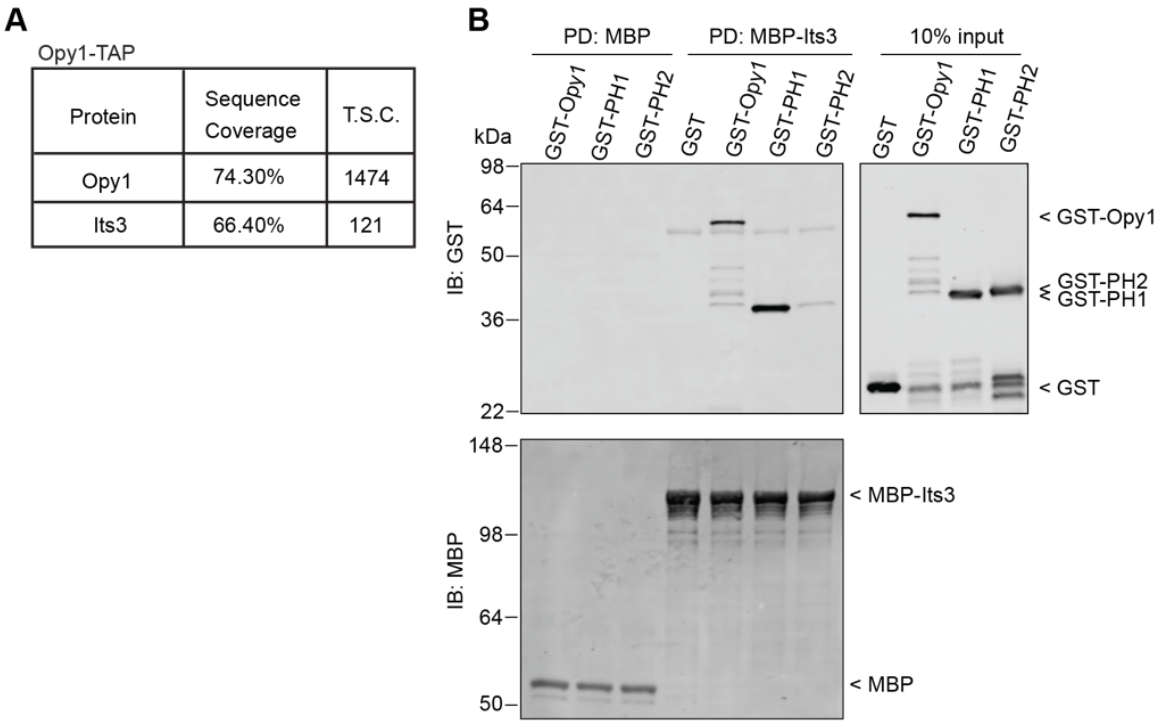

Figure 4.3. Opy1 and Its3 directly interact. (A) Summary of mass spectrometry data from Opy1-TAP. T.S.C. = total spectral counts. (B) MBP-Trap resin-bound MBP or MBP-Its3 was incubated with GST, GST-Opy1, GST-PH1, or GST-PH2, washed, and the proteins were separated by SDS-PAGE. Representative immunoblot of the in vitro binding assays are shown; experiment was performed three times with similar results. PD = pull down, IB = immunoblot.

To determine the functional consequence of the Its3-Opy1 interaction, we first used live-cell imaging to examine if Opy1 influences Its3 PM localization. The punctate pattern of Its3 at the PM was unaffected by *opy1* deletion (Figure 4.4A). The PI4-kinase Stt4, which also localizes to PM punctae, was similarly unaffected by Opy1 loss (Figure 4.5A). However, Opy1-mNG localization to the PM is dramatically reduced in *its3-1*, a temperature-sensitive allele (Snider et al., 2018). Thus, Its3 is necessary for Opy1 PM localization, possibly through directly binding Opy1, by generating $PI(4,5)P_2$ that recruits Opy1 to the PM, or a combination of both mechanisms.

We next tested if *S. pombe* Opy1 modulates Its3 kinase activity. We performed kinase assays with recombinant MBP-Its3, liposomes containing the Its3 substrate PI4P, and ATP, then used the ADP-Glo assay as a read-out for lipid kinase activity as described previously (Nishimura et al., 2019) (Figure 4.4B). Adding Opy1 to the kinase assay did not significantly affect Its3 activity (Figure 4.4C). This result is consistent with our previous determination that PM PI4P and $PI(4,5)P_2$ levels are not affected by *opy1* deletion in vivo (Snider et al., 2018). Opy1 also had no effect on Its3 membrane binding or access to substrate, based on Its3 co-pelleting with PI4P liposomes in vitro (Figure 4.4D), and the observation that Opy1 overproduction did not alter Its3 PM localization in vivo (Figure 4.5B). We hypothesized that if Opy1 negatively regulates Its3 in cells, then deletion of *opy1* would suppress the growth defects of *its3-1,* analogously to *S. cerevisiae opy1*Δ suppressing *mss4* temperature sensitive cells (Ling et al., 2012). However, *opy1*Δ did not suppress *its3-1* (Figure 4.5C). Additionally, one would expect that combining *opy1*Δ with deletion of PI-5-phosphatases would result in negative genetic interactions if Opy1 also acted to oppose Its3 kinase activity. To the contrary, we found no growth defects when *opy1*Δ was combined with either single or double deletions of PI5-phosphatases (Figure 4.5D-E). Together, these results indicate that Opy1 does not regulate Its3 localization or kinase activity.

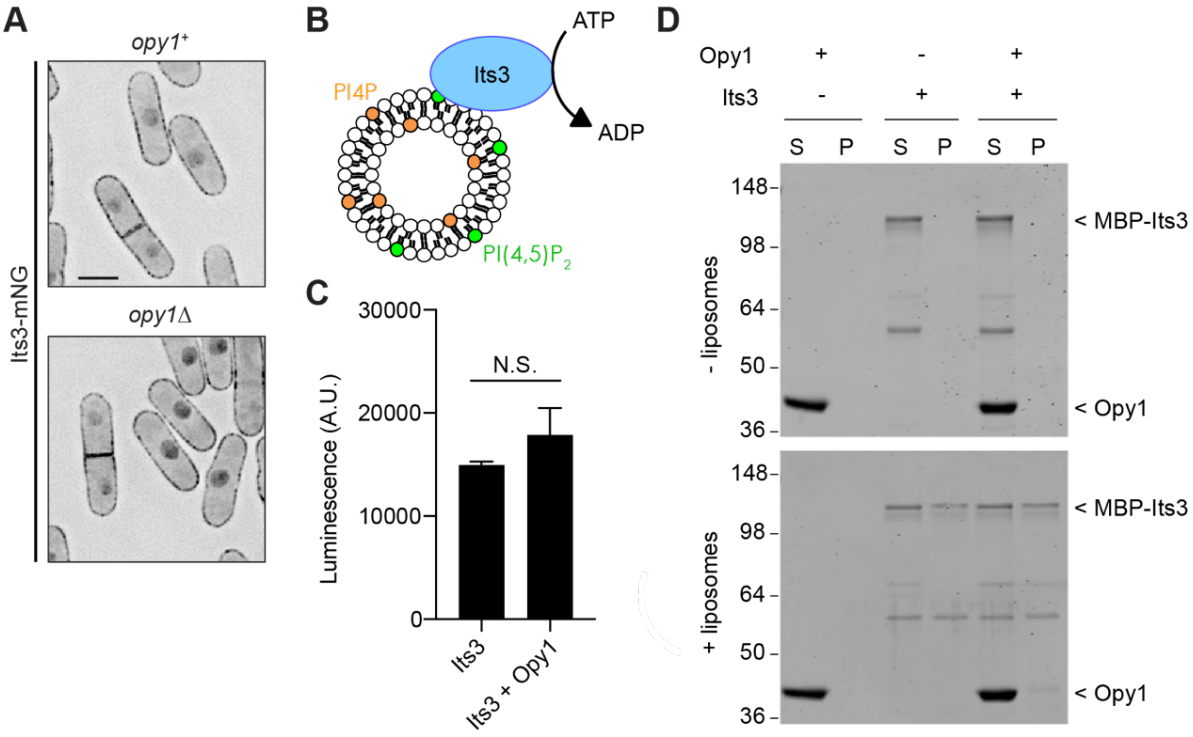

Figure 4.4. Opy1 does not regulate Its3 localization or kinase activity. (A) Live-cell imaging of Its3-mNG in indicated genotypes. Scale bar = 5 μm. (B) Schematic of Its3 lipid kinase assay, adapted from Nishimura et al., 2019. (C) ADP-Glo assay measuring mean Its3 kinase activity toward PI4P-containing liposomes. Control values from liposomes without PI4P have been subtracted from each. Error bars represent SEM, N.S. = not significant, Student's t-test, four experiments. (D) Liposome co-pelleting assay for Its3 in the presence and absence of Opy1 with PI4P-containing liposomes. S = supernatant, P = pellet. Experiment was repeated twice with similar results.

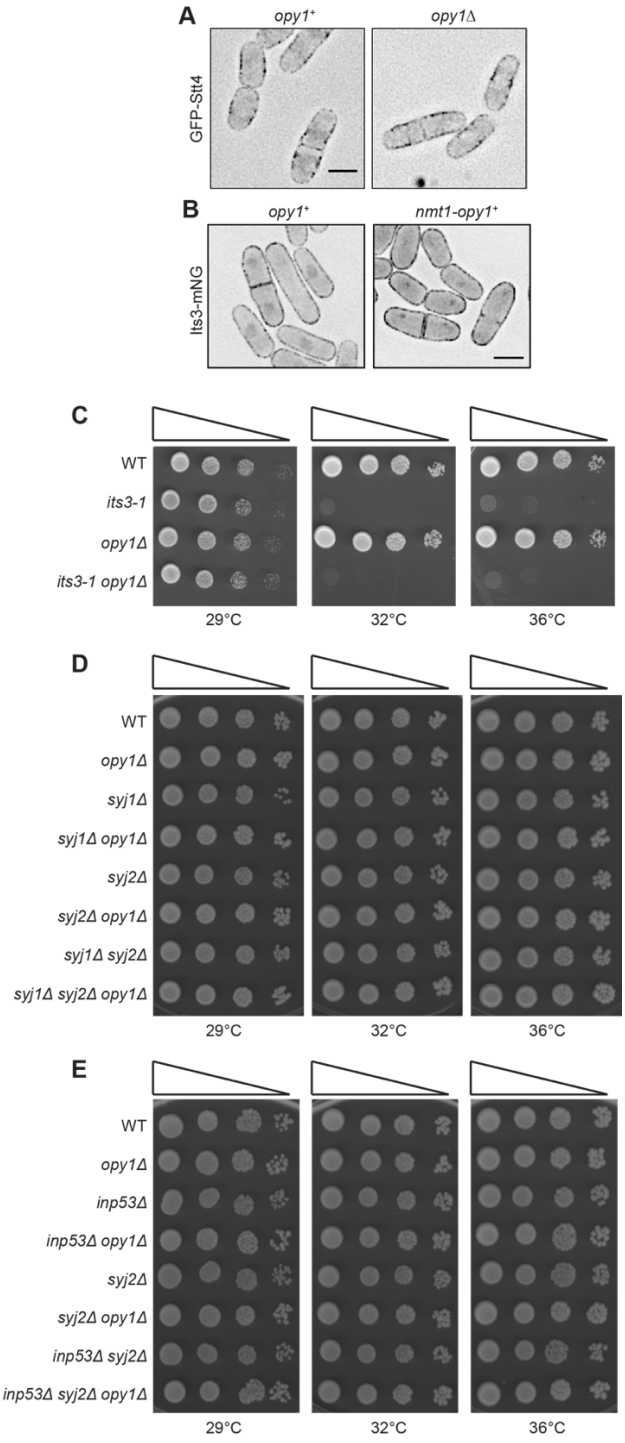

Figure 4.5. Opy1 does not influence localization of Stt4 or Its3, nor does it affect growth of mutants compromised for PI5-phosphatase activity. (A) Representative live-cell images of GFP-Stt4 in cells of the indicated genotypes. Scale bar = 5 µm. (B) Representative images of Its3-mNG in wild type (*opy1*$^{+}$) or in cells over-producing *opy1* from the *nmt1* promoter (*nmt1-opy1*$^{+}$) after 24 hours in media lacking thiamine. Scale bar = 5 µm. (C-E) Growth assay of indicated strains at the indicated temperatures on YE.

Given that Opy1 binds PI(4,5)P_2 specifically, we hypothesized that high levels of Opy1 in cells would sequester PI(4,5)P_2 and result in cytokinesis defects, similar to what we observed when a PI(4,5)P_2 sensor was overproduced (Snider et al., 2017). In *S. pombe*, reduced levels of PM PI4P and PI(4,5)P_2 cause CR anchoring defects that manifest as ring sliding events away from cell center and off-center septation (Snider et al., 2018; Snider et al., 2017). We drove overexpression of *opy1*$^+$ using the *nmt1* promoter and first examined changes in PM PIPs using low level production of biosensors that do not cause any observable growth defect in live cells (Snider et al., 2018). We found that not only the PI(4,5)P_2 sensor (GFP-2xPH_{Plc}) but also the PI4P sensor (GFP-P4C_{SidC}) were reduced in abundance at the PM when Opy1 was over-produced (Figure 4.6A-D). These results can be explained by Opy1 out-competing the PI(4,5)P_2 sensor. Further, given the importance of PM PI(4,5)P_2 for many processes, it is likely that cells expend their PI4P reservoir in an attempt to re-establish the PI(4,5)P_2 PM pool. Consistent with the idea that excess Opy1 sequesters PI(4,5)P_2, *efr3*Δ cells exhibit growth defects upon Opy1 over-production (Figure 4.7A), similar to our previous result that *efr3*Δ and *its3-1* are synthetically lethal, presumably because multiple steps in the PI(4,5)P_2 synthesis pathway are disrupted (Snider et al., 2018). Also consistent with what would be expected from elevated levels of a PI(4,5)P_2 binding protein, Opy1 over-production resulted in off-center septation (Figure 4.6E-F), and over-produced GFP-Opy1 localized in a more homogeneous pattern along the PM compared with the punctate pattern of endogenous Opy1 (Figure 4.7B vs Figure 4.2B-C), more closely resembling the localization of a PI(4,5)P_2 sensor (Snider et al., 2018). If Opy1 does compete with GFP-2xPH_{Plc} for PI(4,5)P_2, we predicted that high levels of the sensor would out-compete Opy1 for PM PI(4,5)P_2 binding. To test this, we overproduced the PI(4,5)P_2 sensor (2xPH_{Plc}) in Opy1-GFP cells. In controls cells, Opy1-GFP localized along the PM and septum, as expected, but upon overexpression of 2xPH_{Plc}, more Opy1 was diffuse in the cytoplasm and less was detected at the cell cortex, as shown by line scans across the cell (Figure 4.6G-H). These results further support the conclusion that Opy1 specifically binds PM PI(4,5)P_2.

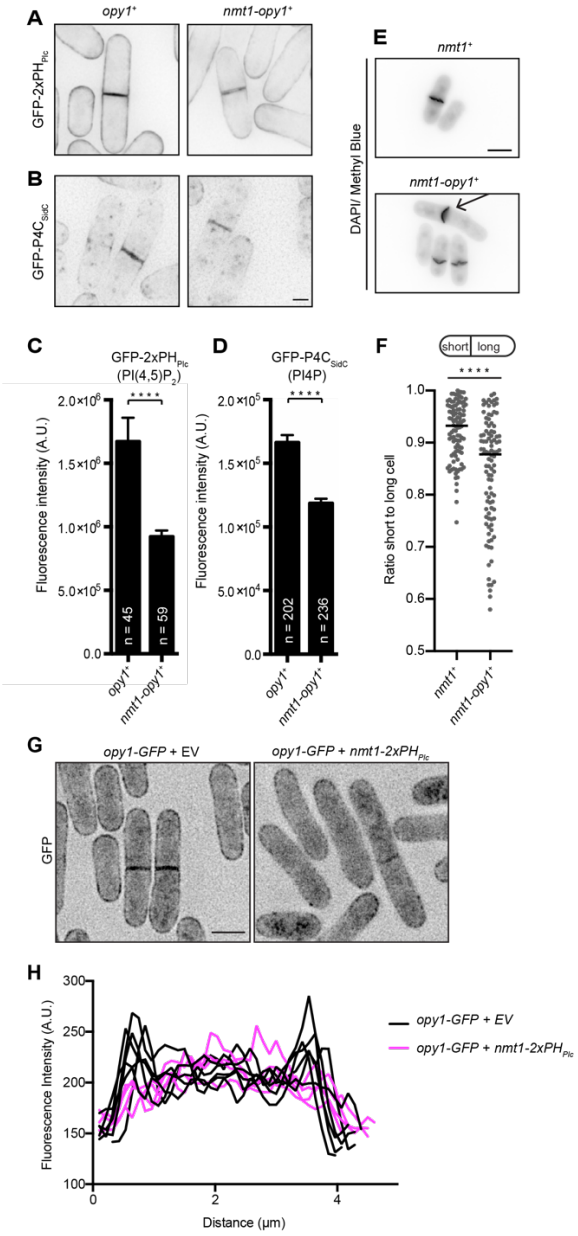

Figure 4.6. Opy1 over-production results in cytokinesis defects. (A, B) Representative live-cell images of indicated PIP biosensors in wildtype (*opy1*$^{+}$) or cells over-producing *opy1* from the *nmt1* promoter (*nmt1-opy1*$^{+}$). Scale bar = 2 μm. (C, D) Quantification of division site intensity of indicated biosensor related to A, B. Error bars represent SEM, **** p < 0.0001, Student's t-test, three experiments. (E) Representative images of fixed cells stained with DAPI and methyl blue. Prior to fixation, overexpression was induced in cells carrying either empty vector (*nmt1*$^{+}$) or an *opy1* overexpression vector (*nmt1-opy1*$^{+}$) for 28 hours in media lacking thiamine. Scale bar = 5 μm. Arrow indicates a cell with an off-center septum. (F) Quantification of off-center septation as a measure of the ratio of short to long daughter cell length related to E. Bars represent means. ****p<0.0001, Student's t-test. (G) Representative live cell images of *opy1-GFP* cells expressing either an empty vector (EV) or *nmt1-2xPH*$_{Plc}$. Scale bar = 5 μm. (H) Five representative line scans across cells from G.

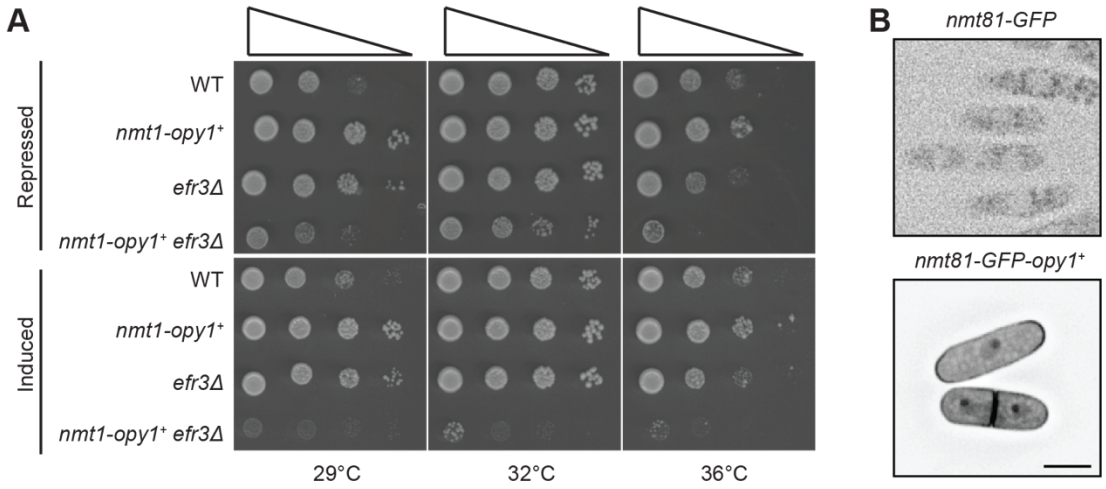

Figure 4.7. Over-expression of Opy1 results in negative genetic interaction with *efr3*Δ. (A) Growth assay of indicated strains at the indicated temperatures on plates containing (repressed) or lacking (induced) thiamine. (B) Representative images showing localization of overexpressed GFP-Opy1. Prior to imaging, overexpression was induced in cells carrying either empty vector (*nmt81-GFP*) or a GFP-Opy1 overexpression vector (*nmt81-GFP-opy1*$^+$*)* for 24 hours in media lacking thiamine. Images are not scaled identically due to the difference in signal. Scale bar = 5 μm.

We have found that *S. pombe* Opy1 binds membrane through its N-terminal PH domain. This is similar to some mammalian dual PH domain proteins (e.g. pleckstrin), which also bind lipids with N-terminal PH domains instead of, or in addition to, C-terminal ones (Bach et al., 2006; Edlich et al., 2005; Ma et al., 1997), but different from *S. cerevisiae* Opy1 that uses its C-terminal PH domain (Ling et al., 2012). However, full-length *S. cerevisiae* and *S. pombe* Opy1 proteins share the property of specifically binding PI(4,5)P_2-containing liposomes and show no appreciable interaction with PI4P- nor PI(3,4,5)P_3-containing membranes. Further, both proteins depend on PI5-kinases for PM localization (Ling et al., 2012; Snider et al., 2018; Snider et al., 2017). Thus, both *S. cerevisiae* and *S. pombe* Opy1 have the properties of an endogenous PI(4,5)P_2 sensor.

Although a direct interaction between *S. cerevisiae* Opy1 and Mss4 has not been reported, both PH1 and PH2 can isolate Mss4 from cell lysates (Ling et al., 2012). In contrast

we found that *S. pombe* Opy1 directly binds both membrane and Its3 through PH1, while no interaction was detected between PH2 and Its3. It is somewhat surprising that PH1-GFP did not localize to the PM given that PH1 binds to both Its3 and $PI(4,5)P_2$. However, other PH domain proteins oligomerize, and in some cases oligomerization is required for high affinity membrane binding (Klein et al., 1998). It is unknown if *S. pombe* Opy1 shares this property, but the need for multimerization could explain why PH1-GFP did not localize to the PM (Figure 4.2B-C).

Importantly, while we found that Its3 and Opy1 can directly interact, we obtained no evidence that Opy1 negatively regulates Its3 kinase activity. This differs from the model that *S. cerevisiae* Opy1 acts as a coincidence detector for $PI(4,5)P_2$ and Mss4 to inhibit Mss4 in the presence of high levels of its product (Ling et al., 2012). We propose therefore that Opy1 evolved to perform different cellular functions in *S. cerevisiae* and *S. pombe*. Different functions are somewhat unexpected considering there are mammalian proteins with similar domain structure to the yeast Opy1 proteins, and one of these, TAPP1, has similar effects to *S. cerevisiae* Opy1 when overproduced in *S. cerevisiae* cells (Ling et al., 2012). Specifically, overexpression of either of these proteins in *S. cerevisiae* cells deficient in PI5-phosphatase activity restored $PI(4,5)P_2$ levels (Ling et al., 2012).

Based on these results, Ling et al. proposed that the dual PH domain containing proteins may utilize their PH2 domains to bind specific PIPs and their PH1 domains to bind different PIP kinases (Ling et al., 2012). However, *S. pombe* Opy1 does not fit this model despite its similarity in domain layout. Also, the PH2 domains of TAPP1, TAPP2, and pleckstrin specifically bind $PI(3,4)P_2$ (Dowler et al., 2000; Edlich et al., 2005; Thomas et al., 2001; Wullschleger et al., 2011), but the connections between the PH1 domains of these proteins and regulation of PIPs are not fully defined (Abrams et al., 1996; Bach et al., 2006; Ma et al., 1997). As exemplified by *S. pombe* Opy1, a major complication in the study of these proteins is that they can sequester their lipid binding partners, giving rise to indirect changes in PM membrane composition. Therefore, caution is warranted when interpreting results from over-expression of dual PH

domain containing proteins. Further study of these proteins, particularly at endogenous expression levels, will be required to determine if there are unifying characteristics amongst this group of proteins beyond a similar domain structure.

Materials and methods

Recombinant protein expression and purification

6xHis-Opy1, GST, GST-Opy1, GST-PH1, GST-PH2, MBP, and MBP-Its3 were produced in *Escherichia coli* Rosetta2(DE3)pLysS cells. 6xHis-Opy1 was purified on cOmplete His-Tag resin (Roche) according to the manufacturers protocol. 6xHis tags were removed by thrombin digestion at room temperature followed by purification on a benzamidine FF Hitrap column (GE Healthcare) to remove thrombin. GST and GST fusions were purified using GST-Bind resin according to the manufacturers protocol (EMD Millipore). MBP and MBP-Its3 were purified using amylose resin according to manufacturer's protocol (New England Biolabs). MBP-Its3 was purified further by gel filtration on a 16/600 Superdex 200 column (GE Healthcare).

Liposome methods

Liposome formation and co-pelleting assays were performed as previously described (McDonald et al., 2016). Folch fraction lipids were obtained from Sigma-Aldrich, all others were obtained from Avanti Polar Lipids. $CHCl_3$ lipid stocks were mixed at the desired ratios and dried under N_2 gas followed by removal of chloroform under high vacuum. For Fig. 4.1, liposomes were rehydrated in 50 mM Tris pH 7.4, 150 mM NaCl and for Fig. 4.4, liposomes were rehydrated in 50 mM Tris pH 7.4, 150 mM NaCl, 10 mM $MgCl_2$, 1 mM DTT to a concentration of 1 mg/mL. Liposomes were subjected to 10 freeze/thaw cycles and extruded through polycarbonate filters of 400 nm pore size (Whatman) with a mini-extruder (Avanti). For Fig. 4.1E-F, phosphatidic acid (PA, egg, chicken), PI4P (brain), PI(4,5)P_2 (brain), and 18:1 PI(3,4,5)P_3 were added at 5% where indicated. DOPS was added at 10% (PS), DOPE at 15%

(PE), and DOPC (PC) was added to make up the total to 100%. For Fig. 4.4, liposomes contained 70% PC, 15% PE, 10% PS, and 5% PI4P. For control liposomes in ADP-Glo assay, no PI4P was included in the liposomes.

For co-pelleting assays in Fig. 4.1, 20 µg of Opy1 was added to 0.5 mg/ml (final concentration) liposomes or buffer for control. For Fig. 4.4D, MBP-Its3 was added at 150 nM and Opy1 was added at a 10 fold molar excess to MBP-Its3. The reaction was incubated for 15 minutes at room temperature before centrifugation at 150,000xg in an Optima TL ultracentrifuge for 15 minutes at 25°C. Pellet and supernatant fractions were resuspended in equal volumes and analyzed by SDS-PAGE. Protein bands were visualized by Coomassie staining and quantified using a LI-COR Odyssey CLx.

For the ADP-Glo assay, 400 µM liposomes (either PI4P-containing or control) were incubated in a 50 µl kinase reaction with 1 µM ATP, 50 nM MBP-Its3, and 500 nM Opy1 where added. The reaction was buffered in 50 mM Tris pH 7.4, 150 mM NaCl, 10 mM $MgCl_2$, 1 mM DTT. The kinase reactions were incubated for 30 minutes at 27°C. The kinase reactions were then added to the ADP-Glo assay according to the manufacturer's protocol (Promega). 25 µl from the kinase reaction was transferred to a white 96-well plate. 25 µl of the ADP-Glo reagent was then added and allowed to incubate for 40 minutes, followed by addition of 50 µl of kinase detection reagent for 30 minutes. Luminescence was detected using a BIO-TEK Synergy HT Microtiter plate reader. For the graph in Fig. 4.4C, four experiments were averaged after subtraction of the luminescence signal resulting from a kinase reaction with control liposomes containing no PI4P.

Yeast methods

S. pombe strains were grown in yeast extract (YE) medium or minimal medium with appropriate supplements. To construct *opy1(4N)* and *opy1* truncation strains, first constructs were generated by PCR amplifying *opy1* or *opy1* fragments from genomic DNA with 300 bp 5'

and 3' flanking regions and then inserted in the BamHI/PstI restriction sites of pSK+ by Gibson assembly. The *opy1(4N)* mutations were introduced by site-directed mutagenesis according with the QuikChange Lightning Multi Site-directed Mutagenesis Kit according to protocol (Agilent Technologies) and verified by sequencing. 1 µg of the pSK+ *opy1* constructs were then linearized by digestion with XhoI and transformed into *opy1::ura+* cells, then integrants were selected on YE + 5-FOA media. Transformants were verified by PCR and by sequencing. Genes were tagged at the 3' end of their ORFs with TAP:kan^R, GFP:kan^R, or mNG:hyg^R using pFA6 cassettes as previously described (Bähler et al., 1998b; Wach et al., 1994) and integration of tags was verified by PCR. A lithium acetate method (Keeney and Boeke, 1994b) was used in *S. pombe* transformations. Introduction of tagged loci into other genetic backgrounds was accomplished using standard *S. pombe* mating, sporulation, and tetrad dissection techniques.

For spot assays, cells were grown to log phase at 25°C in minimal media containing thiamine, then washed into media lacking thiamine for 24 hours prior to plating. 10 million cells were resuspended in 1 mL of water, and 10-fold serial dilutions were made. 2.5 µl of each dilution was spotted on plates lacking thiamine (induced) or containing thiamine (repressed) for Figure 4.7 and on YE plates for Figure 4.5. The plates were incubated at the indicated temperatures.

Overexpression of Opy1 and of 2xPH$_{Plc}$ was accomplished by using the repressible *nmt1* or *nmt81* promoter in the pREP1 series of vectors (Basi et al., 1993). For Fig. 4.6E-F, 1 µg of *pREP1* or *pREP1-opy1* plasmids, for Fig. 4.6G-H 1 µg of *pREP1* or *pREP1-2xPH$_{Plc}$* plasmids and for Fig. 4.7B, 1 µg of *pREP81-GFP* or *pREP81-GFP-opy1* were transformed into wildtype cells by electroporation and plated on media containing thiamine. Cells were then grown in liquid culture in the presence of thiamine and then washed into media lacking thiamine for 28 hours (Fig. 4.6E-F), 26 hours (Fig. 4.6G-H) or 24 hours (Fig. 4.5B) to induce over-production. For Fig. 4.6A-D, 4.5B, and 4.7A, a strain was constructed in which *nmt1-opy1$^+$* was integrated into the genome. This was accomplished by subcloning *nmt1-opy1$^+$* from the *pREP1-opy1$^+$*

plasmid into pJK210 (Keeney and Boeke, 1994b). The resulting plasmid was then linearized with NruI and integrated into the *ura4-294* locus. Integration was verified by PCR. To induce over-production of Opy1 in the resulting strain, cells were grown in media lacking thiamine for 24 hours.

In vitro binding assay

For the binding assay in Fig. 4.3B, all proteins were combined at 1 μM in 50 mM Tris pH 7.4, 150 mM NaCl, 0.1% NP-40 with 10 μL MBP-Trap agarose (Chromotek) to pull down MBP or MBP-Its3. The reactions were incubated for 1.5 hours at 4°C then the beads were washed four times in binding buffer. Associated proteins were analyzed by SDS-PAGE followed by transfer to PVDF and immunoblotting with anti-MBP antibody at a dilution of 1:10,000 (New England Biolabs) and anti-GST antibody at 1:10,000 (VU160, rabbit polyclonal). Secondary antibodies were conjugated to IRDye680LT or IRDye800 (LI-COR Biosciences). Blotted proteins were detected with an Odyssey CLx (LI-COR Biosciences).

TAP purification and MS analysis

Tandem affinity purification of Opy1-TAP and subsequent identification of interacting proteins by mass spectrometry were performed as previously described (Chen et al., 2013; Elmore et al., 2014; Gould et al., 2004) with the following changes: a newer version of Scaffold (Scaffold v4.4.1.1; Proteome Software) was used, and the minimum peptide identification probability was changed to 95.0%. Proteins identified in a mock tandem affinity purification and in an Ada1-TAP purification (Ada1 is a nuclear protein) were subtracted from the Opy1-TAP results.

Western blot of cell lysates

Cell pellets were snap frozen in dry ice-ethanol baths. Lysates were prepared using a Fastprep cell homogenizer (MP Biomedicals). Cells were extracted with 8 M Urea, 50 mM Tris,

1 mM PMSF, 1.3 mM benzamidine. Cleared lysate was then resolved by SDS-PAGE and transferred to PVDF membrane using an iBlot (Invitrogen). The membrane was then probed with anti-GFP at a dilution to 1:1000 (Roche) or anti-PSTAIRE at a dilution of 1:10,000 (Cdc2; Sigma-Aldrich). Secondary antibodies were conjugated to IRDye680LT or IRDye800 (LI-COR Biosciences). Blotted proteins were detected with an Odyssey CLx (LI-COR Biosciences).

Statistical Analysis

All statistical analyses were performed in Prism 8 (GraphPad Software).

Microscopy

Yeast for live-cell imaging were grown at 25°C. Live-cell and fixed-cell images of *S. pombe* cells were acquired using a Personal DeltaVision (Applied Precision) that includes a microscope (IX71; Olympus), 60× NA 1.42 Plan Apochromat and 100× NA 1.40 U Plan S Apochromat objectives, fixed and live-cell filter wheels, a camera (CoolSNAP HQ2; Photometrics), and softWoRx imaging software (Applied Precision). Z-sections were spaced at 0.5 µm. Images for quantification were not deconvolved. Images used for representative images were deconvolved with 10 iterations. For all representative images, the middle z-slice is shown.

Intensity measurements in Fig. 4.6 were made with FIJI (Schindelin et al., 2012). An ROI was created to measure the intensity around the membranes lining the division septum and background was subtracted by creating a region of interest in the same image in an area containing no cells (Snider et al., 2017; Waters, 2009). For intensity measurements, sum projections were analyzed.

For fixed cell imaging, cells were grown to log phase at 32°C and then fixed in 70% ethanol for 30 minutes. Cells were then washed three times with PBS before DAPI and methyl blue staining.

To quantify off-center septation, fixed cells stained for nuclei and cell wall were imaged. The coordinates of the cell tips and septum were logged. Lengths of the shorter and longer cell were calculated from these coordinates and reported as a ratio (Snider et al., 2017).

Chapter V

Opposite surfaces of the Cdc15 F-BAR domain create a membrane platform that coordinates cytoskeletal and signaling components for cytokinesis[4]

Introduction

During cytokinesis, many eukaryotes build an actin- and myosin-based cytokinetic ring (CR) that constricts to bring together opposing membranes and physically pinch the cell in two (Cheffings et al., 2016; Gould, 2016). Studies using the fission yeast *Schizosaccharomyces pombe* have advanced our understanding of the composition, assembly, and function of the CR (Cheffings et al., 2016; Goyal et al., 2011; Mangione and Gould, 2019; Pollard and Wu, 2010; Rincon and Paoletti, 2016). The *S. pombe* CR is composed of ~40 proteins, many of which are evolutionarily conserved (PomBase, (Wood et al., 2012)).

More recently, studies using advanced microscopy techniques, such as fluorescence photoactivatable localization microscopy (fPALM), have revealed finer details of CR structure (McDonald et al., 2017). The pre-constriction CR is 182 $\pm$ 26 nm wide and its components are stratified into layers relative to the PM that extend 293 $\pm$ 64 nm into the cytoplasm. A membrane-proximal layer, 0-80 nm from the PM, is composed primarily of membrane-bound

---

[4] Adapted from Chloe E. Snider, Mintu Chandra, Nathan A. McDonald, Alaina H. Willet, Scott E. Collier, Melanie D. Ohi, Lauren P. Jackson, and Kathleen L. Gould (2020). Opposite surfaces of the Cdc15 F-BAR domain create a membrane platform that coordinates cytoskeletal and signaling components for cytokinesis. *Cell Reports* 33(12):108526.

scaffolds. An intermediate layer contains a network of signaling and accessory components that localize 80-160 nm from the PM. Finally, a distal layer (160-350 nm from the PM) consists of F-actin, myosin motor domains, and actin-binding proteins. Electron cryotomography analysis demonstrated that there is a ~60 nm gap between the F-actin of constricting CRs and the PM (Swulius et al., 2018), consistent with displacement of the F-actin from the PM in pre-constriction CRs. Though a similar stratification of components has been observed for other actin-based structures built on the PM, like focal adhesions (Kanchanawong et al., 2010), it is unknown if stratification or the overall nanoscale architecture is important for CR function.

Clearly, however, the PM-proximal protein layer is key to connecting the CR to the PM. One component of this layer is the essential F-BAR protein Cdc15 (Fankhauser et al., 1995; McDonald et al., 2017). Cdc15 is one of the earliest and most abundant CR proteins to arrive at the division site cortex (Wu and Pollard, 2005; Wu et al., 2003), concordant with its role as a core CR scaffold and anchor (Arasada and Pollard, 2014; Carnahan and Gould, 2003; Mangione et al., 2019; McDonald et al., 2017; McDonald et al., 2015; Ren et al., 2015; Roberts-Galbraith et al., 2009; Wachtler et al., 2006; Willet et al., 2015a). Cdc15 is a conventional F-BAR family member in that it contains an N-terminal F-BAR domain that dimerizes to create a membrane-binding module (McDonald et al., 2015). The F-BAR domain oligomerizes in a tip-to-tip manner, facilitating high avidity membrane binding, however it does not tubulate membrane and belongs to a subset of the F-BAR domain family that lacks tubulation activity (McDonald et al., 2015). When oligomerization of the Cdc15 F-BAR domain is disrupted, the CR is unstable and can disassemble leading to failed cytokinesis (McDonald et al., 2015).

Like other F-BAR family proteins that contain an additional domain(s) for signaling or protein binding, Cdc15 has an SH3 domain (McDonald and Gould, 2016b). Between the N-terminal F-BAR and C-terminal SH3 domains is a predicted intrinsically disordered region (IDR), important for Cdc15 phosphoregulation and recruitment of the protein phosphatase calcineurin (CN) to the CR (Mangione et al., 2019; Roberts-Galbraith et al., 2010). Cdc15 is

hyperphosphorylated in interphase predominantly on residues within the IDR (Bhattacharjee et al., 2020; Kettenbach et al., 2015; Lee et al., 2018; Magliozzi et al., 2020; Roberts-Galbraith et al., 2010; Wachtler et al., 2006). This phosphorylation inhibits Cdc15 oligomerization and membrane and protein binding activities. Upon mitotic entry, Cdc15 is dephosphorylated, allowing it to oligomerize, bind membrane, and perform its scaffolding functions (Bhattacharjee et al., 2020; Roberts-Galbraith et al., 2010).

In the mature pre-constriction CR, the Cdc15 SH3 domain extends ~150 nm away from the PM (McDonald et al., 2017). There it interacts with a network of protein partners that promote robust completion of cytokinesis and septation (Arasada and Pollard, 2014; Cortés et al., 2015; Ren et al., 2015; Roberts-Galbraith et al., 2009). Disruption of the SH3 domain network results in CR fragmentation (Roberts-Galbraith et al., 2009).

While most of Cdc15's protein partners bind to its SH3 domain, the formin Cdc12 binds to the F-BAR domain in the PM-proximal CR layer (Carnahan and Gould, 2003; McDonald et al., 2017; Willet et al., 2015a). Other F-BAR family members also interact with partners through their F-BAR domains (Begonja et al., 2015; Garabedian et al., 2018; Kostan et al., 2014; Liu et al., 2019; Oh et al., 2017; Senju et al., 2011; Shoham et al., 2003), but in no case has a complete structural and mechanistic understanding of these interactions at membranes been described.

Here, we show that the Cdc15 F-BAR domain binds membrane and Cdc12 simultaneously, revealing an important mechanism linking the actin of the CR to the PM. We also report the crystal structure of the Cdc15 F-BAR domain and identify residues on its cytosolic face, opposite the membrane binding face, that coordinate binding to the formin Cdc12, and also the paxillin-like protein Pxl1. Surprisingly, mutation of the Cdc15 F-BAR domain residues that disrupt the CR recruitment of Pxl1 and its binding partner CN results in a shallow pre-constriction CR, with intermediate and distal layer components localizing closer to each other and ~35% closer to the PM than in wildtype. These organizational defects lead to

failures in CR constriction. Our results indicate that an F-BAR domain creates a platform on the PM to bring together cytoskeletal and signaling elements necessary to establish the architecture of the CR that, in turn, is required for its function. Our study presents a view of F-BAR domains in which their functions at membranes profoundly influence the overall architecture of an actin-based structure.

Results

The Cdc15 F-BAR domain binds membrane and Cdc12 simultaneously with opposite faces

The Cdc15 F-BAR domain binds membrane and also a motif in the formin Cdc12 (McDonald et al., 2015; Willet et al., 2015a), but it is unknown if it binds both simultaneously. We generated giant unilamellar vesicles (GUVs), mixed them with purified GFP-Cdc15 F-BAR domain and/or rhodamine(Rh)-conjugated peptide containing the Cdc12 F-BAR binding motif (residues 20-40), and visualized these components by fluorescence microscopy. We observed that the Cdc12 peptide localized to GUVs minimally on its own, however in combination with Cdc15 F-BAR domain, the two proteins co-localized on vesicles (Figure 5.1A). These results indicate that the Cdc15 F-BAR domain can position Cdc12 directly at the PM by binding membrane and Cdc12 simultaneously.

We next took a hybrid structural and biophysical approach to understand how the Cdc15 F-BAR domain coordinates Cdc12 at the PM. Attempts to determine the X-ray crystal structure of wildtype Cdc15 F-BAR domain were unsuccessful. Therefore, we focused on a well-characterized mutant, E30K E152K, that prevents F-BAR domain oligomerization (McDonald et al., 2015). We determined the X-ray crystal structure of the Cdc15 F-BAR domain (residues 19-312; E30K E152K) at 3.5 Å resolution using molecular replacement in PHASER with final R_{work} and R_{free} values of 26.7% and 31.0%, respectively (Figure 5.1B-C, Table 5.1). The *S. pombe* Imp2 F-BAR domain (PDB ID: 5C1F) (McDonald et al., 2016) served as the initial search model (33% sequence identity). Crystals were of space group $P12_11$ with two molecules in the

asymmetric unit. Both copies show well-ordered electron density for residues 35-297. We could not clearly trace electron density at the N- and C-termini of either copy. Specifically, we lack density for chain A residues 19-34 and 299-312 and chain B residues 19-22 and 297-312. The final model exhibits good overall geometry with 92.5% residues favored and 7.3% residues allowed in the Ramachandran plot.

The Cdc15 F-BAR domain has four α-helices (Figure 5.2A-B). We resolved four helices in chain A and three in chain B because the C-terminus exhibits more disorder. As expected (Henne et al., 2007; Peter et al., 2004), the Cdc15 F-BAR domain formed a dimer. The two copies interacted over an extensive solvent accessible surface area (4279.5 $Å^2$ calculated in AREAIMOL), primarily mediated by van der Waals contacts (data not shown). The structure reveals a central core containing a six α-helical dimer bundle, in which each F-BAR domain contributes three extended and partly kinked α-helices (α1/α2/α3). The Cdc15 F-BAR domain has an α-helix at its C-terminus. We observe density for residues in helix α4 (270-279) in both chains but it is better ordered in chain A. The ends of the F-BAR domain have extended wings that adopt a slightly bent conformation compared to the core. The C-termini of both chains (chain A residues 278-299; chain B residues 272-297) lack secondary structure but maintain extensive contact with helices α2 and α3 from the symmetry copy. Previously defined residues required for oligomerization were at the tips of the F-BAR domain dimer (Figure 5.1D) and membrane-binding residues were on the concave face of the dimer (Figure 5.1E), as predicted (McDonald et al., 2015).

The two closest structural homologs in the Protein Data Bank are the *S. pombe* Imp2 and *S. cerevisiae* Hof1 F-BAR domains (McDonald et al., 2016; Moravcevic et al., 2015); these exhibit 1.8 Å and 2.9 Å RMSD, respectively. Structural comparison of the Cdc15 and Imp2 F-BAR domains, however, reveals the Cdc15 F-BAR domain is flatter and wider overall (Figure 5.2C-G). We also compared our structure with the human GAS7 F-BAR domain (PDB: 6IKN)

(Hanawa-Suetsugu et al., 2019). These two F-BAR domains are approximately the same length: the Cdc15 F-BAR domain measures 211 Å from tip to tip, while GAS7 F-BAR domain measures 212 Å. GAS7 F-BAR appears slightly flatter than does Cdc15 F-BAR domain (Figure 5.2C-G), but they are generally similar in form. Considering that GAS7, like Cdc15, is a non-tubulating F-BAR domain (Hanawa-Suetsugu et al., 2019; McDonald et al., 2015), it is logical that the Cdc15 F-BAR domain is more similar in shape to Gas7 than to the Imp2 F-BAR domain (Figure 5.2C-G), which can tubulate membranes (McDonald et al., 2016).

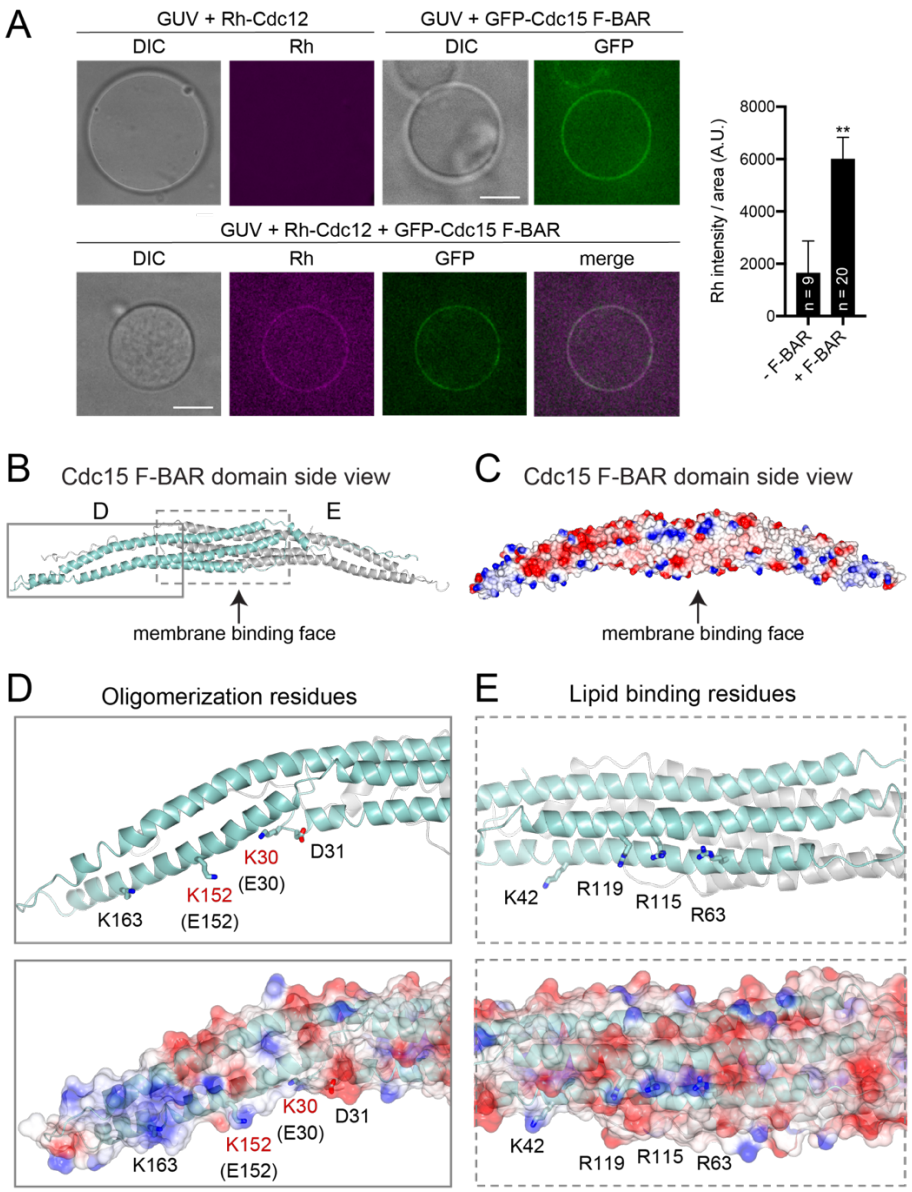

Figure 5.1. The Cdc15 F-BAR domain binds membrane and Cdc12 simultaneously. (A) Left: fluorescence micrographs of GUVs to which rhodamine (Rh)-conjugated Cdc12 peptide (aa 20-40) and GFP-Cdc15 F-BAR domain were added as indicated. GUVs were visualized by DIC. Single Z slices are shown, scale bars = 5 μm. Right: Quantification of mean Rh-Cdc12 signal on GUVs in the absence (- F-BAR) and presence (+ F-BAR) of GFP-Cdc15 F-BAR domain. Error bars represent S.E.M, ** $p < 0.01$, Student's *t* test. Number of vesicles analyzed (n) is indicated. (B) Ribbon diagram of the crystal structure of the Cdc15 F-BAR domain (E30K E152K). Chain A = cyan, Chain B = gray (C) Electrostatic surface potential of the Cdc15 F-BAR domain. Red = negative, blue = positive surface charge. Inset (D) shows a close-up of oligomerization residues (McDonald et al., 2015) on ribbon (top) and surface (bottom) diagrams with wildtype residues in black; two residues shown in red (K30, K152) were mutated to facilitate crystallization. Inset (E) highlights lipid binding residues (McDonald et al., 2015) on ribbon (top) and surface (bottom) diagrams.

Data collection statistics	Cdc15 residues 19-312 (E30K E152K)
PDB ID	6XJ1
Space group	$P12_11$
Molecules in ASU	2
Resolution (Å)	37.59 – 3.52 (3.64 – 3.52) [a]
Unit cell	
a, b, c (Å)	54.77, 75.17, 93.23
α, β, γ (°)	90.0, 95.3, 90.0
Total observations	59,833
Unique reflections	8,999 (688) [a]
Completeness (%)	94.52 (71.89) [a]
R_{merge} [b]	0.094
R_{pim}	0.042
$\langle I/\sigma(I) \rangle$	13.2
$CC_{1/2}$	0.958
Multiplicity	6.4
Refinement statistics	
R_{work}/R_{free}(%) [c,d]	26.67 / 30.96
Protein atoms	4,404
Waters	57
Other	None
Wilson B (Å^2)	19.40
Average B (Å^2)[e]	88.76
R.m.s. deviations	
Bond length (Å)	0.003
Bond angles (°)	0.670
Ramachandran plot	
Favored (%)	92.39
Allowed (%)	7.42
Outliers (%)	0.19

Table 5.1. Summary of crystallographic structure determination statistics

[a]Values in parentheses refer to the highest resolution shell.

[b]$R_{merge} = \Sigma|I - \langle I \rangle| / \Sigma\langle I \rangle$, where I is the intensity of each individual reflection.

[c]$R_{work} = \Sigma h|F_o - F_c| / \Sigma_l|F_o|$, where F_o *and* F_c are the observed and calculated structure-factor amplitudes for each reflection *h.*

[d]R_{free} was calculated with 10% of the diffraction data selected randomly and excluded from refinement.

[e]Calculated using Baverage.

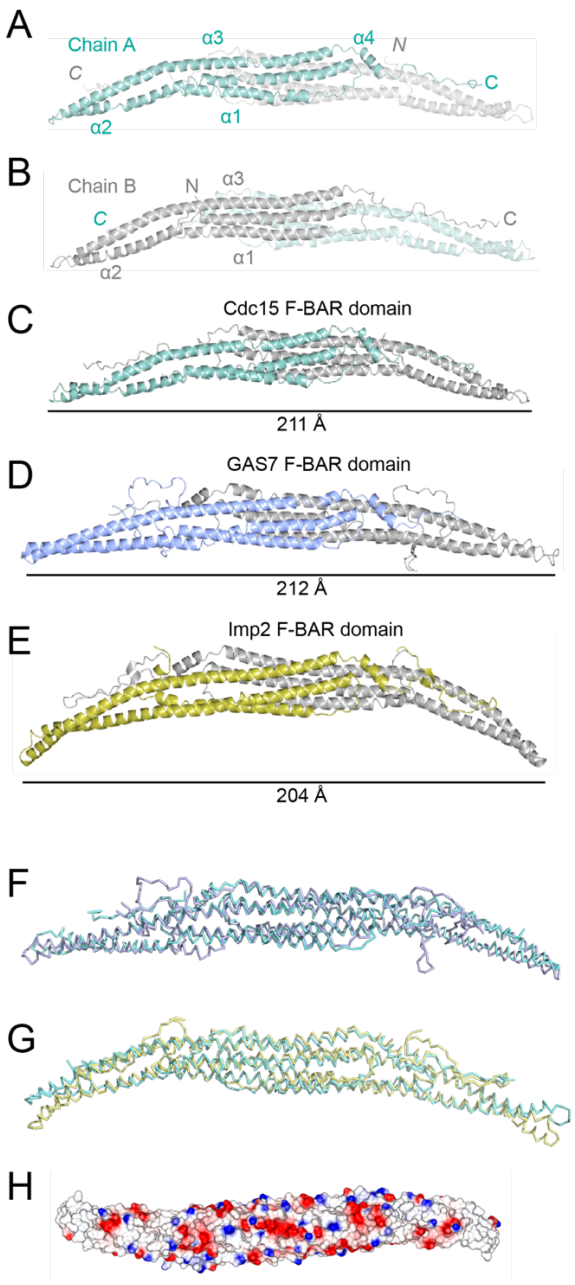

Figure 5.2. Comparison of Cdc15 F-BAR domain with other F-BAR domain structures. (A-B) X-ray crystal structure of the Cdc15 F-BAR domain (E30K E152K) mutant determined here. Chain A and B are labeled as well as helices and N- and C-termini. (C-E) X-ray crystal structure of (C) Cdc15 F-BAR domain (E30K E152K mutant), (D) GAS7 F-BAR domain (PDB ID: 6IKN) and (E) Imp2 F-BAR domain (PDBID: 5C1F). F-BAR domain lengths from tip-to-tip are noted below each. The GAS7 and Cdc15 F-BAR domains exhibit flatter architectures compared to Imp2. (F) RMSD-based structural overlay of Cα trace of GAS7 F-BAR domain (purple) and Cdc15 F-BAR domain (cyan) (G) RMSD-based structural overlay of Cα trace of Imp2 F-BAR domain (yellow) and Cdc15 F-BAR domain (cyan). (H) Electrostatic surface potential of the Imp2 F-BAR domain convex face. Red = negative, blue = positive charge.

We next determined where on the Cdc15 F-BAR domain Cdc12 binds. The Cdc12 F-BAR binding motif is rich in basic amino acids (Willet et al., 2015a) and mutation of an acidic patch on the non-membrane binding face of the F-BAR domain (Cdc15-3A: D255, E256, E259, Figure 5.3A) to alanines eliminated the F-BAR interaction with Cdc12 peptide (residues 20-40) (Figure 5.3B, left). Although the Imp2 F-BAR domain is similar to the Cdc15 F-BAR domain and has acidic patches on its non-membrane binding face (Figure 5.2H), it did not interact with the Cdc12 peptide (Figure 5.3B, right). The Cdc15 (E30K E152K) F-BAR domain exists as a dimer in solution (McDonald et al., 2015) and using isothermal titration calorimetry (ITC), we found that the Cdc12 peptide binds Cdc15 (E30K E152K) F-BAR with low micromolar affinity and calculated stoichiometry (n) of 0.5 (K_d= 5 μM, Figure 5.3C, Table 5.2). We interpret these results to mean that one peptide binds two molecules of Cdc15 F-BAR, or one dimer. Together these results establish that one side of the Cdc15 F-BAR domain binds membrane while the opposite face binds a single molecule of Cdc12, thus linking the key actin nucleator of the CR to the PM. It will be interesting to determine if utilization of non-membrane-binding surfaces for protein interaction is a general feature of other F-BAR domains.

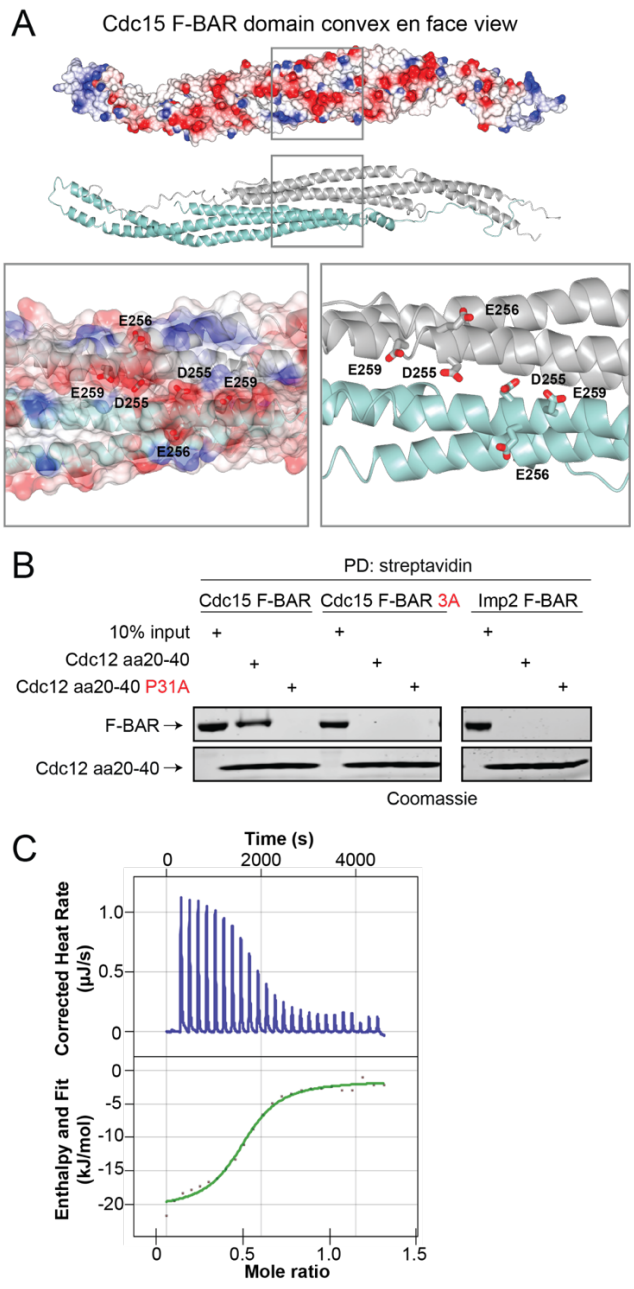

Figure 5.3. Cdc12 binds the cytosolic face of the Cdc15 F-BAR domain. (A) Top: electrostatic surface potential of the Cdc15 F-BAR domain cytosolic face. Red = negative, blue = positive surface charge. Middle: ribbon diagram of the same face. Bottom: close-up of residues mutated in Cdc15-3A. (B) in vitro binding assays with biotin-labeled Cdc12 peptide (aa 20-40) and purified Cdc15 F-BAR domain (left; wildtype and 3A) or Imp2 F-BAR domain (right). F-BAR domain associated with streptavidin resin (PD = pull down) was analyzed by SDS-PAGE followed by Coomassie staining. Cdc12(aa 20-40 P31A) was a negative control (Willet et al., 2015a). (C) Representative ITC experiment with Cdc12 (aa 20-40) peptide and Cdc15 F-BAR domain (E30K E152K). Top panel shows raw data; bottom panel shows normalized integrated data. See also Table 5.2.

Experiment #	Protein	Peptide	K_D (μM)	ΔH° (kCal/mol)	ΔG° (kCal/mol)	TΔS° (kCal/mol)	n
1	Cdc15 F-BAR (200 μM)	Cdc12 (750 μM)	4.7	- 4.6	- 7.3	2.7	0.50
2	Cdc15 F-BAR (200 μM)	Cdc12 (750 μM)	3.5	- 4.2	- 7.5	3.3	0.49
3	Cdc15 F-BAR (200 μM)	Cdc12 (750 μM)	6.9	- 3.7	- 6.7	3.0	0.55
Average ± S.D.	Cdc15 F-BAR (200 μM)	Cdc12 (750 μM)	5.0 ± 0.9	- 4.2 ± 0.4	- 7.2 ± 0.4	3.0 ± 0.3	0.52 ± 0.03

Table 5.2. ITC Summary. Summary of three ITC experiments with Cdc15 F-BAR domain (E30K E152K) and Cdc12 peptide (residues 20-40). S.D. = standard deviation.

The Cdc15 F-BAR domain has additional functions

When Cdc12-Cdc15 F-BAR domain interaction is disrupted by mutating P31 in the Cdc12 F-BAR binding motif (*cdc12-P31A*), Cdc12-P31A recruitment to the CR is reduced (Willet et al., 2015a). We expected that if we disrupted the Cdc12 binding site on the F-BAR domain, Cdc12 localization to the CR would be similarly reduced. Thus, we introduced the 3A mutations into the endogenous *S. pombe* Cdc15 locus to construct *cdc15-3A* and examined Cdc12-mNeonGreen (mNG) localization (Figure 5.4A). As predicted, Cdc12-mNG fluorescence intensity at the CR was reduced by ~40% in *cdc15-3A* compared to wildtype, similar to the reduction measured for Cdc12-P31A-mNG (Figure 5.4A). As expected for two mutations that disrupt the same interaction, the effect of *cdc15-3A* on Cdc12-P31A-mNG CR localization was non-additive (Figure 5.4A). However, unlike *cdc12-P31A*, ~30% of *cdc15-3A* cells had a strikingly abnormal morphology with defects including additional cell poles, bulges, or swells, and heterogeneous lengths (Figure 5.4B). These results indicated that *cdc15-3A* disrupted another F-BAR domain function in addition to interfering with Cdc12 recruitment to the CR.

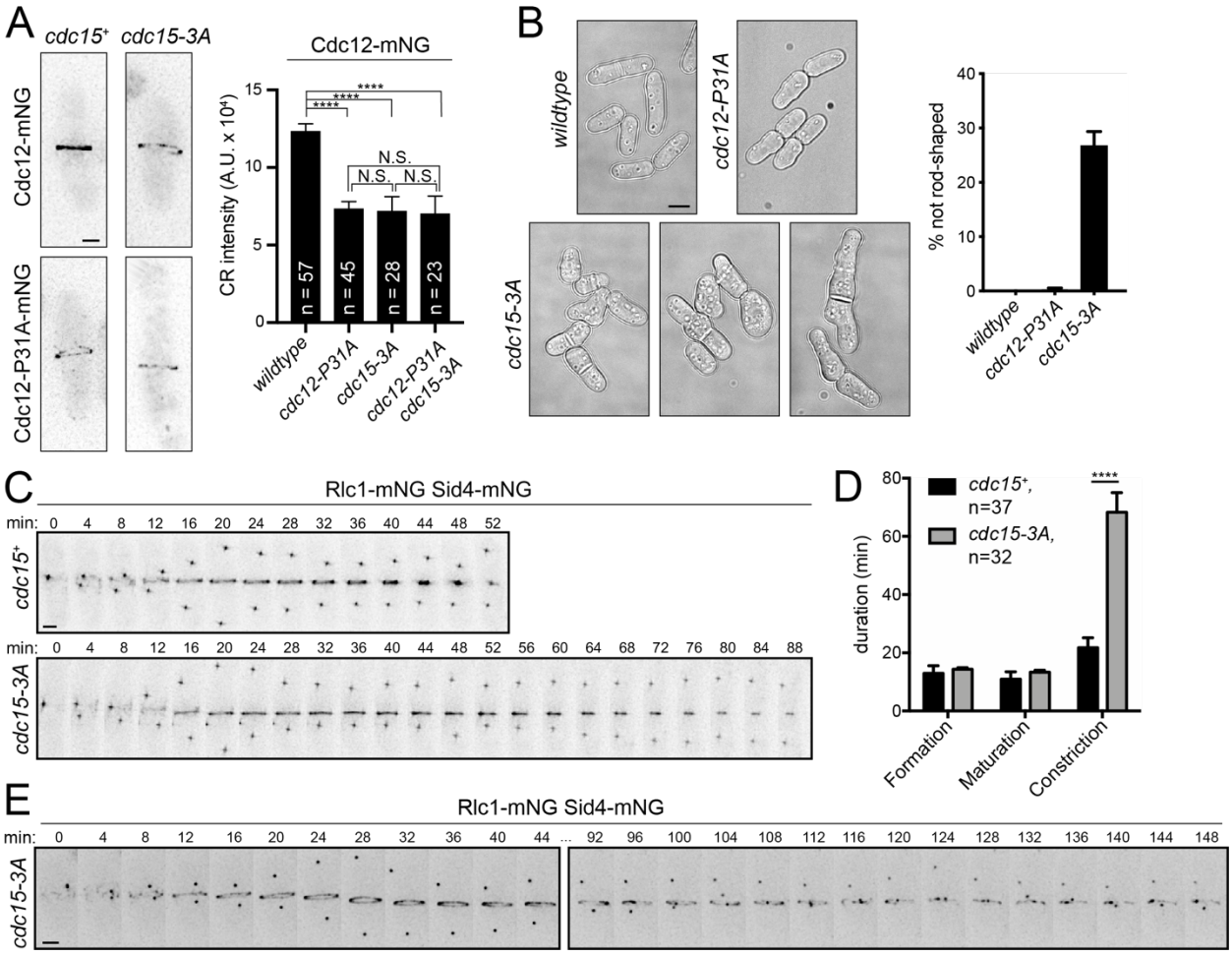

Figure 5.4. The Cdc15 F-BAR domain cytosolic face has functions in addition to scaffolding Cdc12. (A) Left: representative live-cell images; deconvolved max projections are shown. Right: quantification of mean Cdc12-mNG CR intensity. Error bars represent S.E.M. ****p<0.0001, ***p<0.001, N.S. = not significant- p > .99; one-way ANOVA with Tukey's post-hoc test for multiple comparisons. Total number of cells (n) from 3 experiments is indicated. Scale bar = 2 μm. (B) Left, DIC images of the indicated strains grown at 25°C. Single Z slices are shown, scale bar = 5 μm. Right, quantification of morphology defects in indicated strains. wildtype, n = 305 cells; *cdc12-P31A*, n = 341 cells; *cdc15-3A*, n = 436 cells; 3 experiments, error bars = S.E.M. (C) Representative montages from time-lapse imaging. Minutes elapsed since spindle pole body separation are indicated. Max projections are shown. Scale bar = 2 μm. (D) Quantification of the mean duration of CR events, related to C. ****p<0.0001, Student's *t* test. Error bars represent S.E.M., number of cells analyzed (n) is indicated. (E) Example montage of *cdc15-3A* cell with aberrant CR constriction. Ellipses denote frames removed for space, max projections are shown. Scale bar = 2 μm.

We tested if mutating the F-BAR domain surface resulted in an overall loss of protein folding or defects in the known F-BAR domain functions of oligomerization and membrane binding. Recombinant Cdc15-3A F-BAR domain was not defective in overall tertiary structure, as determined by circular dichroism (Figure 5.5A), and was oligomerization-competent as shown by negative stain electron microscopy (Figure 5.5B). To assay Cdc15-3A membrane binding, we produced Cdc15 or Cdc15-3A in bacteria with kinase Pom1, as previously described (Bhattacharjee et al., 2020). Mutations that abolish F-BAR domain oligomerization (E30K E152K) were included to allow robust purification (Bhattacharjee et al., 2020; McDonald et al., 2015). As expected, we found that phosphorylated Cdc15-3A (E30K E152K) did not bind membrane in a liposome co-pelleting assay (Figure 5.5C), as previously reported for phosphorylated Cdc15 (E30K E152K) (Bhattacharjee et al., 2020). But, dephosphorylated Cdc15-3A (E30K E152K) co-pelleted with liposomes to a similar extent as Cdc15 (E30K E152K), indicating that the 3A mutations do not prevent Cdc15 from binding membrane (Figure 5.5C). Next, we confirmed that Cdc15-3A was produced (Figure 5.5D) and localized to the CR at wildtype levels in cells (Figure 5.5E). Thus, there is no significant defect in any known function ascribed to the Cdc15 F-BAR domain except the binding of Cdc12.

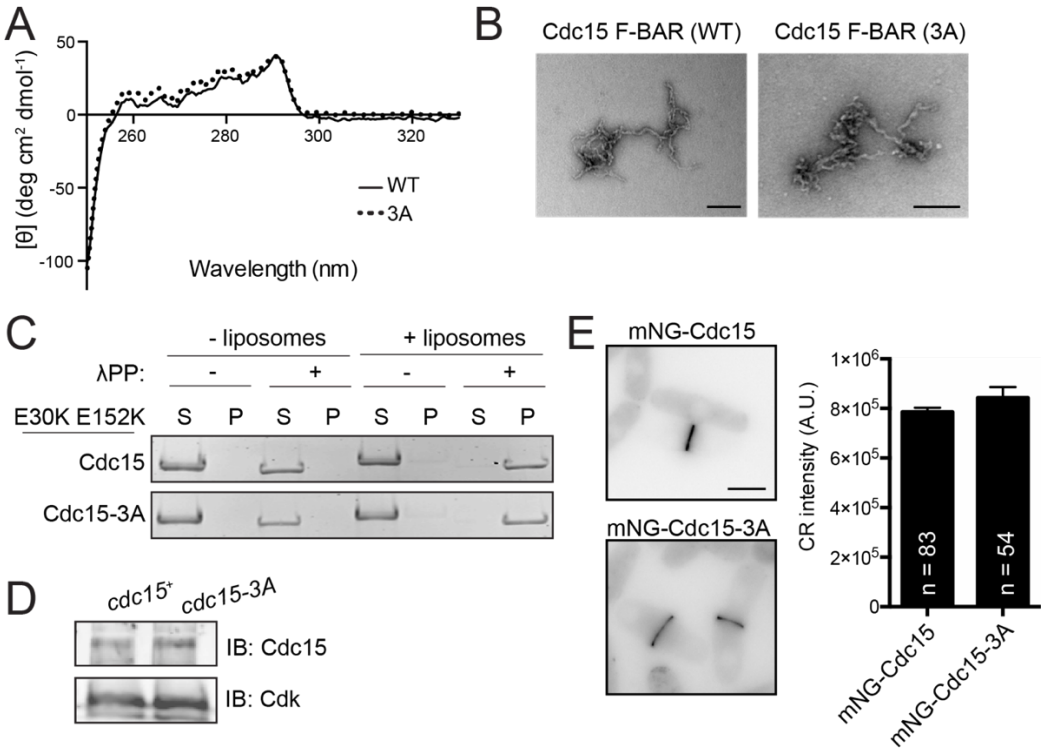

Figure 5.5. Cdc15-3A is competent for membrane-binding, oligomerization, expression, and localization. (A) Near-UV circular dichroism spectra of purified wildtype (solid line) and 3A (dotted line) F-BAR domain. (B) Representative negative stain electron microscopy images of oligomers formed by purified wildtype (left panel) or 3A (right panel) Cdc15 F-BAR domain. Scale bar = 100 nm. (C) Co-pelleting assay with Folch fraction liposomes and FLAG-Cdc15 (E30K E152K) with or without the F-BAR 3A mutations. Cdc15 was either hyper-phosphorylated (-λPP) or hypo-phosphorylated (+λPP). Fractions were collected and analyzed by SDS-PAGE and Coomassie staining. S = supernatant (unbound), P = pellet (bound). (D) Cdc15 was detected in whole cell lysates from indicated genotypes. PSTAIRE was used as a loading control. IB = immunoblot. (E) Left: representative live-cell images of cells expressing mNG-Cdc15 or mNG-Cdc15-3A. Sum projections are shown, scale bar = 5μm. Right: quantification of mean mNG signal at the CR, error bars represent S.E.M. Number of cells analyzed (n) is indicated.

Because Cdc15 is most well-known as a cytokinesis protein (Fankhauser et al., 1995), we examined cytokinesis dynamics in *cdc15-3A*. Cytokinesis occurs in three stages marked by (1) formation of the CR, the time from spindle pole body separation until cytokinetic nodes coalesce into a coherent ring, (2) CR maturation, the time from which the CR is fully formed until constriction initiates, and (3) CR constriction, the time during which the CR decreases in diameter to a single point. Live-cell time-lapse imaging of wildtype and *cdc15-3A* cells

expressing markers of the CR (Rlc1-mNG) and the spindle pole body (Sid4-mNG) to monitor progression through cytokinesis and mitosis, respectively, showed that while the duration of CR formation and maturation were comparable to wildtype in *cdc15-3A*, CR constriction was significantly prolonged (Figure 5.4C-D). In fact we were unable to evaluate all cells because they did not complete constriction before photobleaching of the fluorescent probes or cell death (12.5% of *cdc15-3A* failed constriction, n = 32; 0% of wildtype failed constriction, n = 37). We also saw evidence of CR instability manifested as CR sliding events (CR sliding frequency = 51% $\pm$ 8% for *cdc15-3A,* n = 38 cells; 0% for wildtype, n = 30 cells; 2 experiments) and aberrant constriction (Figure 5.4E). We concluded that *cdc15-3A* cells are defective in the constriction phase of cytokinesis; based on previous results, this cannot be explained by reduced recruitment of Cdc12 alone (Willet et al., 2015a).

The Cdc15 F-BAR domain drives the nanoscale architecture of the CR

Because Cdc15 scaffolds a cohort of proteins through its F-BAR domain, SH3 domain, and IDR, and spans multiple layers of the CR, it is a candidate driver of CR architecture. To examine whether the cytokinesis defects in *cdc15-3A* cells reflected a global change in CR architecture, we used fPALM microscopy (McDonald et al., 2017). In wildtype pre-constriction CRs, the Cdc15 F-BAR domain is positioned at the PM, while its C-terminal SH3 domain extends into the intermediate layer (McDonald et al., 2017). To determine whether this overall organization is retained in Cdc15-3A, we compared the distances to the PM (d_{center}) of the fluorophore mMaple3 fused to the Cdc15 N- or C-terminus. We used the membrane dye mCLING-ATTO647N to label the PM (McDonald et al., 2017; Revelo et al., 2014). Consistent with our in vitro results that there is no apparent deficit in Cdc15-3A membrane binding or oligomerization, we found that mMaple3-Cdc15-3A (F-BAR) was membrane proximal, like wildtype (Figure 5.6A; wildtype: d_{center} = 54 $\pm$ 33 nm; 3A: d_{center} = 51 $\pm$ 41 nm). While in wildtype cells Cdc15-mMaple3 (SH3 domain) is extended into the intermediate layer of the CR, Cdc15-

3A-mMaple3 was on average ~40 nm closer to the PM than wildtype (wildtype: d_{center} = 140 ± 51 nm; 3A: d_{center} = 98 ± 60 nm) (Figure 5.6A). Considering that the *cdc15-3A* mutations are on the F-BAR domain, a position that is ordinarily spatially separated from the Cdc15 SH3 domain, this result was surprising.

Consistent with the altered localization of Cdc15-3A-mMaple3, a second normally intermediate layer protein and Cdc15 SH3 binding partner, Fic1, also localized closer to the PM in *cdc15-3A* (wildtype: d_{center} = 144 ± 43 nm; *cdc15-3A*: d_{center} = 79 ± 59 nm). Unexpectedly, two components of the distal layer, the myosin 2 Myp2 motor head and F-actin also localized closer to the PM (Figure 5.6A) (mMaple3-Myp2- wildtype: d_{center} = 230 ± 75 nm; *cdc15-3A:* d_{center} = 150 ± 70 nm; Phalloidin-Atto488- wildtype: d_{center} = 216 ± 83 nm; *cdc15-3A:* d_{center} = 150 ± 85 nm). On average, these intermediate and distal components localize 35% closer to the PM in *cdc15-3A* compared to wildtype. Altogether these results indicate that there is an overall disruption in the nanoscale architecture of the CR in *cdc15-3A* resulting in a shallower pre-constriction CR. Considering the defects in CR constriction in *cdc15-3A*, this implies that proper distance of the CR away from the PM and distribution of its components relative to one another is required for CR constriction.

The Cdc15 F-BAR domain coordinates partners required for CR architecture

The disruption of CR architecture, subsequent failures in CR constriction, and morphological defects in *cdc15-3A* support the idea that the cytosolic face of the Cdc15 F-BAR domain does more than recruit Cdc12 and likely binds additional factors required for assembling a CR of the proper depth. To define these factors, we examined the localization of 32 proteins in *cdc15-3A* (Table 5.3). Of these, we found that neither paxillin-like protein GFP-Pxl1 (Figure 5.6B) nor the catalytic subunit of the protein phosphatase CN Ppb1-GFP (Figure 5.6C) localized to the CR in *cdc15-3A.* Notably, the morphological defects of *cdc15-3A* resemble those of *pxl1*Δ and *ppb1*Δ (Fujita et al., 2002; Ge and Balasubramanian, 2008; Lu et al., 2002; Martín-García et

al., 2018; Pinar et al., 2008; Yoshida et al., 1994), and CR constriction takes longer in *ppb1*Δ (Figure 5.6D, (Martín-García et al., 2018)), similar to *cdc15-3A* (Figure 5.4C-D). Therefore, the absence of Pxl1 and CN at the CR likely accounts for the morphological and CR defects of *cdc15-3A*.

As the other 30 proteins examined localized to the division site in *cdc15-3A* (Table 5.3), we focused on the possibility that the Cdc15 F-BAR domain binds Pxl1 and/or CN. Although we did not detect binding between purified Cdc15 F-BAR domain and recombinant CN, MBP-Pxl1 bound the Cdc15 F-BAR domain (Figure 5.6E). This binding interaction was abrogated by the Cdc15-3A mutation (Figure 5.6E), indicating that Pxl1 utilizes the same F-BAR binding site as Cdc12. Because Pxl1 associates with CN and is required for its CR localization (Martín-García et al., 2018), we reasoned that loss of CN from the CR in *cdc15-3A* is likely an indirect effect of Pxl1 loss.

Protein	Localized to division site?
GFP-Adf1	Yes
Ain1-GFP	Yes
nmt1-GFP-Cdc8	Yes
Cdc12-mNG	Reduced
Crib-GFP (Cdc42)	Yes
Clp1-GFP	Yes
Cnb1-mNG	No
Cyk3-mNG	Yes
Fic1-mNG	Yes
Fim1-GFP	Yes
For3-mNG	Yes
Hhp1-mNG	Yes
Hhp2-mNG	Yes
Kin1-GFP	Yes
Mid1-GFP	Yes
Mid2-GFP	Yes
Myo1-mNG	Yes
GFP-Myo2	Yes
Myp2-GFP	Yes
Pck1-mNG	Yes
Pck2-mNG	Yes
Pom1-GFP	Yes
Ppb1-GFP	No
GFP-Pxl1	No
Rga7-mNG	Yes
Rgf3-mNG	Yes
GFP-Rng2	Yes
Shk1-mNG	Yes
Sid2-GFP	Yes
Spa2-mNG	Yes
Spn4-GFP	Yes
Wsp1-mNG	Yes

Table 5.3. Protein localizations examined in *cdc15-3A*. Summary of proteins examined for localization to the division site in wildtype and *cdc15-3A* cells by fluorescence microscopy.

We next tested if Pxl1 and/or CN influence Cdc15 conformation in the pre-constriction CR. We wanted to assay Cdc15-mMaple3 position in *pxl1*Δ by fPALM, but a negative genetic interaction with the tagged *cdc15* allele and *pxl1*Δ prevented cell growth in liquid culture. Thus, we focused on CN. Cdc15 phosphostate changes when cells are treated with the CN inhibitor FK506 (Martín-García et al., 2018), and we confirmed that Cdc15 is a direct substrate of

recombinant CN in vitro (Figure 5.6F). Because phosphorylated and dephosphorylated forms of Cdc15 have different conformations when visualized by negative stain electron microscopy, one model for Cdc15 regulation posits that dephosphorylation allows Cdc15 to adopt a more open conformation (Roberts-Galbraith et al., 2010; Wachtler et al., 2006). Therefore we considered if loss of CN in *cdc15-3A* CRs underlies the defects in placement of the Cdc15 C-terminus away from the PM. As predicted, after treatment with the CN inhibitor FK506, the Cdc15 C-terminus was not extended away from the PM to the same extent as in DMSO treated cells, similar to the defect in *cdc15-3A* (Figure 5.6G, DMSO: d_{center} = 152 $\pm$ 55 nm; FK506: d_{center} = 94 $\pm$ 53 nm). Furthermore, we found that Fic1 and the two distal layer components F-actin and the Myp2 motor head localized closer to the PM in FK506 treated cells (Figure 5.6G, Fic1-mMaple3- DMSO: d_{center} = 114 $\pm$ 49 nm, FK506: d_{center} = 95 $\pm$ 61 nm; mMaple3-Myp2- DMSO: d_{center} = 222 $\pm$ 62 nm, FK506: d_{center} = 136 $\pm$ 67 nm; Phalloidin-Atto488- DMSO: d_{center} = 216 $\pm$ 63 nm, FK506: d_{center} = 153 $\pm$ 67 nm). This indicates that CN activity is required for proper Cdc15 conformation and nanoscale organization of the pre-constriction CR.

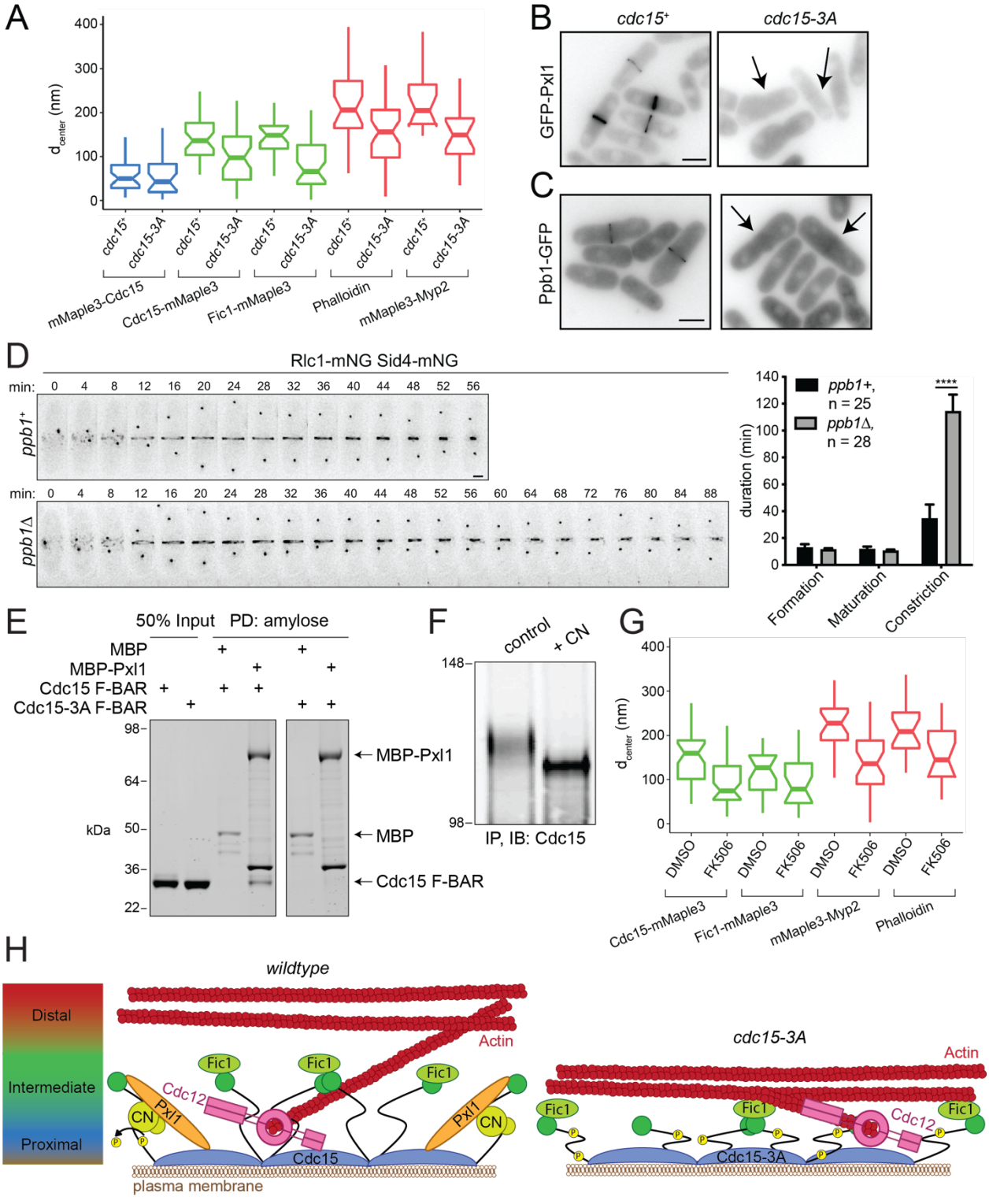
A
B
C
D
E
F
G
H
cdc15+
cdc15-3A
GFP-Pxl1
Ppb1-GFP
mMaple3-Cdc15
Cdc15-mMaple3
Fic1-mMaple3
Phalloidin
mMaple3-Myp2
Rlc1-mNG Sid4-mNG
ppb1+,
n = 25
ppb1Δ,
n = 28
Formation
Maturation
Constriction
50% Input
PD: amylose
MBP
MBP-Pxl1
Cdc15 F-BAR
Cdc15-3A F-BAR
kDa
IP, IB: Cdc15
control
+ CN
DMSO
FK506
wildtype
Distal
Intermediate
Proximal
Actin
Fic1
Cdc12
Pxl1
CN
Cdc15
plasma membrane
Cdc15-3A

Figure 5.6. The Cdc15 F-BAR domain coordinates other binding partners required for proper CR architecture. (A) Distance from the plasma membrane (d_{center}) of the indicated CR components calculated from fPALM. Components of the CR membrane-proximal layer are in blue, intermediate in green, and distal in red. Box plots depict 1st and 3rd quartiles and median; whiskers, minimum and maximum; notches, 95% confidence intervals. See also Table 5.4. (B-C) Representative images of GFP-Pxl1 (B) and Ppb1-GFP (C). Sum projections are shown, scale bars = 5 μm. Arrows indicate cells without CR signal. (D) Left: representative time-lapse montages. Minutes elapsed since spindle pole body separation are indicated; deconvolved max projections are shown. Scale bar = 2 μm. Right: quantification of the mean duration of CR events, ****p<0.0001, Student's *t* test. Error bars represent S.E.M., number of cells analyzed (n) is indicated. (E) Coomassie-stained SDS-PAGE of proteins pulled down (PD) with amylose resin after in vitro binding assay. Both F-BAR constructs also contain E30K E152K mutations. Experiment was repeated with similar results. (F) Immunoblot (IB) of Cdc15 after immunoprecipitation (IP) from asynchronous cells and treatment with either a control or recombinant calcineurin (CN) phosphatase reaction. Numbers indicate position of molecular weight markers in kDa. Experiment was repeated with similar results. (G) Distance from the plasma membrane (d_{center}) of the indicated CR components in cells treated with DMSO or FK506, as in A. See also Table 5.4. (H) Model for the role of the Cdc15 F-BAR domain in driving nanoscale architecture of the CR. Left: The Cdc15 F-BAR domain recruits the formin Cdc12, but also Pxl1, which is required for CN localization. CN dephosphorylates Cdc15 to promote its open conformation. Right: In *cdc15-3A*, the protein network established by the Cdc15 F-BAR domain is disrupted, resulting in a shallower CR. Model not drawn to scale.

	d_{center} ± S.D. (nm)	σ_{width} ± S.D. (nm)	σ_{vert} ± S.D. (nm)	# rings	# localizations	uncertainty ± S.D. (nm)
mMaple3-Cdc15	54 ± 33	136 ± 25	138 ± 29	18	277152	35 ± 8
mMaple3-Cdc15-3A	51 ± 41	149 ± 26	143 ± 26	15	126778	36 ± 8
Cdc15-mMaple3	140 ± 51	144 ± 22	151 ± 34	18	250451	34 ± 8
Cdc15-3A-mMaple3	98 ± 60	154 ± 24	159 ± 31	21	132077	36 ± 8
Fic1-mMaple3	144 ± 43	146 ± 24	152 ± 27	12	142745	36 ± 8
Fic1-mMaple3 *cdc15-3A*	79 ± 59	163 ± 19	159 ± 24	20	141408	37 ± 8
mMaple3-Myp2	231 ± 75	150 ± 19	162 ± 29	8	35039	38 ± 8
mMaple3-Myp2 *cdc15-3A*	150 ± 70	153 ± 22	162 ± 25	8	42563	38 ± 9
Phalloidin-Alexa488	216 ± 83	145 ± 25	136 ± 26	15	142039	32 ± 9
Phalloidin-Alexa488 *cdc15-3A*	150 ± 75	144 ± 28	139 ± 25	21	236193	32 ± 9
Cdc15-mMaple3 + DMSO	152 ± 55	141 ± 29	147 ± 40	19	255067	33 ± 8
Cdc15-mMaple3 + FK506	94 ± 53	168 ± 31	173 ± 28	23	318983	36 ± 9
Fic1-mMaple3 + DMSO	114 ± 49	164 ± 25	145 ± 20	11	100714	36 ± 8
Fic1-mMaple3 + FK506	95 ± 61	175 ± 34	159 ± 28	12	88622	36 ± 8
mMaple3-Myp2 + DMSO	222 ± 62	175 ± 30	179 ± 40	11	39981	36 ± 8
mMaple3- Myp2 + FK506	136 ± 67	167 ± 25	181 ± 35	16	71163	36 ± 9
Phalloidin-Alexa488 + DMSO	216 ± 63	177 ± 36	169 ± 28	10	2814	35 ± 6
Phalloidin-Alexa488 + FK506	153 ± 67	194 ± 25	179 ± 30	9	20744	39 ± 10

Table 5.4. fPALM summary. Summary of fPALM datasets. d_{center} = average distance from the membrane, σ_{vert} = vertical width parameter, σ_{width} = horizontal width parameter averaged across multiple rings as described in McDonald et al., 2017. S.D. = standard deviation.

Discussion

We have demonstrated here that the dimeric Cdc15 F-BAR domain forms a membrane-binding module of shallow curvature. Although multiple F-BAR domain structures have been determined, only one prior study described a crystal structure of an F-BAR domain from the subset that does not tubulate membrane, GAS7 (Hanawa-Suetsugu et al., 2019). Given that both Cdc15 and GAS7 F-BAR crystal structures reveal shallow curvature, we suggest that this structural feature may underlie their inability to tubulate and distinguish them from other family members. Together these structural and functional studies provide further evidence that the primary function of F-BAR domains is to serve as oligomeric membrane binding platforms for the assembly of actin-rich structures (McDonald and Gould, 2016b; Traub, 2015).

Our results demonstrate for the first time that an F-BAR domain can bind membrane and a protein partner simultaneously and establish that the Cdc15 F-BAR does so using opposite faces. Because the PM-bound Cdc15 F-BAR domain is abundant within the CR (Wu and Pollard, 2005), it is intuitive that the large amount of F-BAR domain surface area facing the cytoplasm could be utilized for placing other proteins at the PM. Considering that Cdc15 is in vast excess to its known partner Cdc12 within the mature CR (16,100 $\pm$ 2,300 Cdc15 molecules vs 300 $\pm$ 50 Cdc12 molecules (Wu and Pollard, 2005)), it seems likely that other proteins (e.g. Pxl1) can be accommodated on this surface without competing for a binding site. Although several F-BAR domains from other proteins can substitute for the F-BAR of Cdc15 to support cell viability, cells producing these F-BAR-Cdc15 fusions display morphological defects similar to *cdc15-3A* (Mangione et al., 2019). It is likely that this phenotype arises from the inability of these other F-BAR domains to bind Cdc12 and Pxl1, as we have determined here is the case for the Imp2 F-BAR domain. It will be fascinating to discern how generally F-BAR domains serve to create binding platforms on membranes for specialized components of complex actin structures.

We propose a model wherein the Cdc15 F-BAR domain itself establishes a protein interaction network critical for the integrity of the CR (Figure 5.6H). In addition to Cdc12, we discovered that Pxl1 and CN are part of this network. Although a second Pxl1 binding site exists within Cdc15 consisting of the SH3 domain and a portion of the IDR (Bhattacharjee et al., 2020), we found that an intact F-BAR domain binding site is required for Pxl1 recruitment to the CR. Because both Pxl1 and the Cdc15 IDR are required for CN localization to the CR (Mangione et al., 2019; Martín-García et al., 2018), we propose that Pxl1 recruitment by the Cdc15 F-BAR domain allows Pxl1 and the Cdc15 IDR to cooperatively recruit CN.

Disruption of the network established by the Cdc15 F-BAR domain on the PM has surprisingly long-range effects on the placement of the Cdc15 C-terminus and the rest of the CR's architecture. Our results suggest that there is either a defect in extension of CR components away from the PM during ring assembly or there is a collapse or compression of CR components toward the membrane over time, and it will be interesting to distinguish between these possibilities in future studies.

Although the complete cohort of CN substrates involved in proper CR architecture is unknown, Cdc15 is likely a major target. Because CN does not localize to the CR until it is fully formed, Cdc15 is likely dephosphorylated by other phosphatases first to allow CR formation. Indeed, one model of Cdc15 regulation suggests that dephosphorylation and the subsequent change in conformation occur in two steps, with the first dependent upon the Cdc14 family phosphatase, Clp1 (Roberts-Galbraith et al., 2010; Wachtler et al., 2006). We propose that in the absence of CN, Cdc15 is only partially dephosphorylated, resulting in an intermediate conformation that allows F-BAR domain membrane-binding but not full extension of the remainder of the protein away from the PM (Figure 5.6H). In accord, when cells are treated with FK506, Cdc15 is dephosphorylated as cells enter mitosis, but not to the same extent as in the absence of inhibitor (Martín-García et al., 2018). In support of a multi-step activation model for

F-BAR proteins, more than one stimulus is required for relief of Nwk autoinhibition, including binding to $PI(4,5)P_2$ and multiple proteins (Del Signore et al., 2020).

In summary, our results establish that F-BAR domain oligomers can serve as an extensive platform to link numerous proteins in actin-based structures to the PM. Moreover, disruption of F-BAR domain function as a protein landing pad can have long-range ramifications to the architecture and functionality of cytoskeletal structures.

Materials and methods

Experimental model and subject details

S. pombe strains were grown in yeast extract (YE) media and all strains for live-cell imaging were grown at 25°C. Standard methods were used for genetic crosses and tetrad analyses.

Yeast methods

cdc15 mutants were integrated at the endogenous locus by rescuing *cdc15*$^{+}$ */cdc15::ura4*$^{+}$ diploids with pIRT2-*cdc15* mutant constructs containing 5' and 3' noncoding flanks. Haploid integrants resistant to 5-fluorourotic acid (5-FOA) were isolated and the *cdc15* mutations were verified by PCR and sequencing. Transformations of *S. pombe* cells were performed with a lithium acetate method (Keeney and Boeke, 1994b).

Plasmids

Cdc15-3A mutant constructs (D255A E256A E259A) were generated by site-directed mutagnesis and sequenced to confirm. To co-express the calcineurin subunits, *ppb1*, *cnb1*, and *cam1* were PCR amplified from *S. pombe* cDNA. In pET-Duet-1, *ppb1* was assembed in the BamHI/NotI sites in frame with the 6X-His tag and Cnb1 was assembled in the NdeI/KpnI sites by Gibson assembly. Cam1 was assembled in the NcoI/NotI sites of pRSF-Duet-1.

Recombinant protein expression and purification.

The pET15b plasmid encoding 6X-His fusion Cdc15 F-BAR domain (residues 19-312 E30K E152K) was transformed into BL21(DE3)/pLysS *E. coli* cells and expressed in 2XTY broth at 37°C until the O.D. (A_{600}) reached 0.8. The cultures were induced with 0.5 mM isopropyl-1-thio-β-D-galactopyranoside (IPTG) at 20°C overnight, and cells were harvested by centrifugation (6000 × g, 10 min, 4°C). The cell pellet was resuspended in lysis buffer (20 mM Tris pH 8.0, 300 mM NaCl, 50 µg/ml of benzamidine, 100 units DNase I, and 2 mM β-mercaptoethanol). The cells were lysed by mechanical disruption at 30 kpsi using a cell disrupter (Constant Systems). The lysate was clarified by centrifugation at 50,000 × g for 30 min at 4 °C. Proteins were purified using affinity chromatography from the clarified lysate. The purification was performed on a Ni-NTA (GE healthcare) gravity column. The column was thoroughly washed with lysis buffer containing 100–500 mM salt. Finally, the protein of interest was eluted using a linear gradient of imidazole (100–300 mM) in 20mM Tris pH 8.0, 300 mM NaCl. The eluted affinity purified 6X-His tagged Cdc15 F-BAR domain was finally subjected to size exclusion chromatography using a superdex-200 16/600 HiLoad column, pre-equilibrated with 20 mM Tris (pH 8.0), 100 mM NaCl and 2 mM DTT, attached to an AKTA pure (GE Healthcare). The purified protein was concentrated to 10 mg/ml using a Centricon Ultra-10 kDa centrifugal filter (Millipore, USA) for crystallization.

Cdc15 F-BAR domains (residues 19-312) for all experiments other than crystallography were expressed as a 6xHis fusion in *E. coli* Rosetta2(DE3)pLysS cells grown to log phase in terrific broth, induced overnight at 17°C with 0.1 mM IPTG. Cells were lysed by sonication and F-BAR domains were purified on cOmplete His-Tag resin (Roche) according to manufacturer's protocol. His tags were then cleaved by thrombin digestion and F-BARs were further purified on a HiTrap Q SP anion exchange column (Cytiva Life Sciences) and concentrated with Amicon Ultra Centrifugal Filters (EMD-Millipore).

Full-length Cdc15 constructs were produced as previously described (Bhattacharjee et al., 2020) by co-expressing FLAG-Cdc15(E30K E152K, with or without the 3A mutations) with the kinase Pom1 in Rosetta2(DE3)pLysS cells grown to log phase in terrific broth, induced overnight at 17°C with 0.1 mM IPTG. Cells were lysed in 50 mM Tris pH 7.4, 150 mM NaCl, 0.1% NP-40 by sonication. Cleared lysate was incubated with Anti-FLAG-M2 magnetic resin for 2 hours at 4°C. Beads were then washed extensively in 50 mM Tris pH 7.4, 150 mM NaCl before elution in 200 µg/mL 3x-FLAG peptide for 20 minutes at room temperature. Eluates were then concentrated and cleared by spinning at high speed. For de-phosphorylated samples, 1 µL lambda phosphatase (New England Biolabs) and 1 mM $MnCl_2$ was added and incubated for 15 minutes at room temperature.

Pxl1 was expressed as an MBP fusion as previously described (Bhattacharjee et al., 2020) in the pMAL-c2 vector in Rosetta2(DE3)pLysS cells, which were grown to log phase in terrific broth + 150 µM $ZnCl_2$ (to increase production), induced overnight at 17°C with 0.1 mM IPTG. Cells were harvested, flash frozen, and lysed by sonication in 20 mM Tris pH 7.4, 150 mM NaCl, 0.1% NP-40, and cOmplete EDTA-free protease inhibitor cocktail (Roche). Lysate was cleared at high speed then incubated with amylose resin (New England BioLabs) for 2 hrs at 4°C. Resin was washed thoroughly in lysis buffer. After washing, buffer was added to the resin to create a 1:1 slurry of buffer and resin-bound protein. The concentration of MBP-Pxl1 fusion on resin was calculated by running a sample on SDS-PAGE alongside BSA standards and staining with Coomassie blue.

Calcineurin was produced by co-expressing Ppb1 as a 6xHis fusion (catalytic subunit), Cnb1 (regulatory subunit), and Cam1 (calmodulin) in Rosetta2(DE3)pLysS cells. Cells were lysed by sonication in 50 mM Tris pH 7.4, 150 mM NaCl, 0.1% NP-40 and cleared lysate was incubated with cOmplete His Tag resin (Roche). Resin was washed thoroughly in lysis buffer and then eluted in lysis buffer + 200 mM imidazole. Eluted protein was then dialyzed into 50 mM Tris pH 7.4, 150 mM NaCl, 0.1% NP-40, 2 mM $CaCl_2$, 10 mM $MgCl_2$.

Crystallization and crystallography

Cdc15 F-BAR domain was supplemented with 10 mM DTT before setting up 96-well sitting-drop crystallization screens using a Mosquito liquid handling robot (TTP LabTech). Crystallization plates were incubated at 20°C in a Rock-imager storage hotel (Formulatrix). Cdc15 F-BAR domain at 10 mg/ml was crystallized in 100 mM HEPES (pH 7.0), 1.1 M Sodium Malonate Dibasic Monohydrate (pH 7.0) and 0.5% Jeffamine ED 2003 (pH 7.0) by mixing equal volumes of protein with reservoir solution. Optimized diffraction-quality crystals of Cdc15 F-BAR domain were obtained using streak seeding in hanging drop vapor diffusion 24 well plates at 20°C by mixing equal volumes of protein with reservoir solution. The optimized crystallization condition was 100 mM HEPES (pH 7.0), 1.1 M Sodium Malonate Dibasic Monohydrate (pH 7.0) and 1% Jeffamine ED 2003 (pH 7.0). Diffraction data were collected at the Life Sciences Collaborative Access Team (LS-CAT) facility on beamline 21-ID-D at a wavelength of 0.979Å. To prevent radiation damage, crystals were equilibrated in a cryo-protectant containing 20% Glycerol (v/v) and then flash frozen in a 100 K Nitrogen stream. Cdc15 F-BAR crystal diffracted to 3.5 Å resolution. The data set for Cdc15 F-BAR domain was merged and scaled in the Primitive Monoclinic space group, $P12_11$, using the HKL2000 software suite (Otwinowski and Minor, 1997). The structure of Cdc15 F-BAR domain was solved using molecular replacement in PHASER (McCoy et al., 2007) with the crystal structure of Imp2 F-BAR (PDB ID: 5C1F) as the search model. After several rounds of refinement in PHENIX and model building in COOT (Emsley et al., 2010), the final model consists of two molecules in the asymmetric unit with a R_{factor} and R_{free} of 26% and 29% respectively. Structure images were prepared using PYMOL (pymol.org). Stereochemistry and quality of the structure was monitored after each round of refinement using PROCHECK (Laskowski et al., 1993) and Molprobity (Chen et al., 2010). Data collection and refinement statistics are summarized in Table 5.1. The structural coordinates and structure factors of the Cdc15 F-BAR domain have been deposited in the RCSB Protein Data Bank (PDB: 6XJ1).

Structural analyses and comparison of F-BAR structures

Visualizations and structural superpositions of structures, including Cα overlay traces, were carried out in CCPMG (McNicholas et al., 2011). F-BAR domain length distances were measured in Coot. Solvent-accessible surface area was calculated using CCP4 suite (Winn et al., 2011) program AREAIMOL (Lee and Richards, 1971) with a 1.4 Å radius sphere as a probe. Buried surface area was calculated with the PISA server (Krissinel and Henrick, 2007) (www.ebi.ac.uk/pisa).

Peptides

The Cdc12 synthetic peptide (residues 20-40, TPTPSARRTIGPRAPKSKTTY) used for ITC was synthesized by Genscript. Cdc12 peptide was dissolved in 20 mM Tris, pH 8, 100 mM NaCl and 2 mM DTT for use in ITC binding experiments and crystal screening with Cdc15 F-BAR domain protein. The Cdc12 (residues 20-40) and Cdc12-P31A (residues 20-40) peptides used for binding assays were synthesized with an N-terminal biotin modification and Cdc12 (residues 20-40) peptide for GUV binding assays was synthesized with an N-terminal rhodamine, also by GenScript.

Isothermal titration calorimetry (ITC)

ITC measurements were conducted on a Nano-ITC instrument (TA Instruments) in buffer consisting of 20 mM Tris (pH 8.0), 100 mM NaCl and 2 mM DTT. The sample cell was filled with 300 µL of Cdc15 F-BAR domain protein, while the syringe contained 50 µL of the Cdc12 synthetic peptide (TPTPSARRTIGPRAPKSKTTY). All solutions were degassed prior to being loaded into the cell. Aliquots (2 µL) of 750 µM Cdc12 synthetic peptide solutions were injected into a 100 µM Cdc15 F-BAR domain protein solution at 25°C with an interval gap of 3 min and the syringe rotating at 150 rpm to ensure proper mixing. The heat of dilution was measured by injecting the Cdc12 synthetic peptide into the buffer solution and subtracted from the heat of interaction. Data were analyzed using Nanoanalyser software to extract the thermodynamic

parameters, ΔH°, K_d ($1/K_a$), and stoichiometry, n. The dissociation constant (K_d), enthalpy of binding (ΔH°), and stoichiometry (n) were obtained after fitting the integrated and normalized data to a single-site binding model. The stoichiometry was refined initially, and the value obtained was close to 1; then, n was set to 1.0 for calculation. The apparent binding free energy (ΔG°) and entropy (ΔS°) were calculated from the relationships $\Delta G° = RT\ln(K_d)$ and $\Delta G° = \Delta H° - T\Delta S°$. Experiments were performed in triplicate to check for reproducibility of the data.

Binding assays

Binding assays with Cdc15 F-BAR domains and synthetic biotinylated Cdc12 peptides were performed by mixing F-BAR domain at 0.05 μM and peptide at 0.10 μM with Pierce streptavidin UltraLink resin and incubating for 1 hr at 4°C in binding buffer (50 mM Tris pH 7.4, 250 mM NaCl, 0.1% NP-40). After thorough washing, samples were separated by SDS-PAGE, then stained with Coomassie blue and documented using an Odyssey CLx (LiCor Biosciences).

Binding assays with Cdc15 F-BAR domains and MBP/MBP-Pxl1 were performed by mixing 1 μM MBP or MBP-Pxl1 on amylose resin with 5 μg Cdc15 F-BAR domain in 50 mM Tris pH 7.4, 250 mM NaCl, 0.1% NP-40. All F-BAR domain constructs contained the mutations E30K E152K alone or in addition to 3A mutations. Binding assays were incubated for 1 hr at 4°C. Resin was then washed thoroughly and separated by SDS-PAGE. Gels were then stained with Coomassie blue and documented using an Odyssey CLx.

Western blot of cell lysates

To assay Cdc15 expression levels, pellets were collected from asynchronous populations and snap frozen. Cells were lysed by glass bead disruption in NP-40 buffer (Gould et al., 1991). Lysates were denatured by boiling at 95°C for 1 minute then lysate samples were separated by SDS-PAGE, transferred to PVDF membrane (Immobilon-FL) and probed with anti-Cdc15 serum (VU326 1:10,000) (Roberts-Galbraith et al., 2009) and anti-PSTAIRE (1:10,000,

Sigma-Aldrich) for loading control. Secondary antibodies conjugated to IRdye680/800 were utilized for detection with the Odyssey CLx.

Calcineurin phosphatase assay

Pellets collected from asynchronous cells were flash frozen then lysed by glass bead disruption in a modified NP-40 buffer lacking EDTA. Lysates were denatured by boiling at 95°C for 1 minute. Cdc15 was immunoprecipitated from denatured lysate using anti-Cdc15 serum (VU326) and protein A sepharose (GE Healthcare 17-5280-04) incubated for two hours at 4°C. Sepharose was washed three times with modified NP-40 buffer then washed two times with calcineurin buffer (50 mM Tris pH 7.4, 150 mM NaCl, 0.1% NP-40, 2 mM $CaCl_2$, 10 mM $MgCl_2$). 20 µg recombinant calcineurin or calcineurin buffer for control was then added to the sepharose and incubated for 30 minutes at 30°C with shaking. Samples were then resolved by SDS-PAGE, transferred to PVDF, and probed with anti-Cdc15 serum (VU326). Secondary antibodies conjugated to IRdye680/800 were utilized for detection with the Odyssey CLx.

Circular dichroism

For Near-UV circular dichroism (CD) spectrometry, purified Cdc15 F-BAR domains were analyzed using a Jasco J-810 spectropolarimeter (Jasco Analytical Instruments, Easton, MD). Near-UV data was collected at a protein concentration of 1.05 mg/ml for Cdc15 F-BAR domain and 1.10mg/ml for Cdc15-3A F-BAR domain. Near-UV CD spectra were collected in a 1-cm quartz cuvette with an average time of 4 s for each point and a step size of 10 nm/min from a wavelength of 250 to 330 nm. For both Cdc15 and Cdc15-3A F-BAR domains, four spectra were collected for Near-UV data and background corrected against a buffer blank. Data were converted to mean residue ellipticity [θ]m (degrees cm2dmol−1) using the formula [θ]m = (100*signal in mdeg)/(Cnl), where [θ]m is the mean residue ellipticity, C is the molar concentration of protein in millimolar, n is the number of residues/chain, and l is the cell path length in cm.

Liposome assays

Folch fraction lipids were obtained from Sigma-Aldrich, all others were obtained from Avanti Polar Lipids. Liposomes were formed as previously described (Itoh et al., 2005; McDonald et al., 2015). Briefly, $CHCl_3$ lipid stocks were evaporated in a glass tube under N_2 stream, vacuum dried for 1 hour, rehydrated in 20 mM Tris pH 7.4, 150 mM NaCl buffer before vortexing, 10 cycles of freeze-thawing, and extrusion to 400 nm with an Avanti mini-extruder. Liposome co-pelleting assays were performed as previously described (McDonald and Gould, 2016a), where 100 uL of 1 mg/mL liposomes were mixed with 100 uL of FLAG-Cdc15 (10 µg total) for 15 min at room temperature before centrifugation at 150,000 xg in an Optima TL ultracentrifuge for 15 min at 25˚C. Supernatant and pellet fractions were separated by SDS-PAGE and visualized by staining with Coomassie blue.

Giant Unilamellar Vesicles (GUVs) were formed as previously described (McDonald and Gould, 2016a) by drying 10 µL of 10 mg/mL $CHCl_3$ lipids (69% DOPC, 15% DOPE, 10% DOPS, 5% PI(4)P) on Indium-Tin-Oxide-coated (ITO) glass coverslips (Sigma-Aldrich) under N_2 stream followed by vacuum for 1 hour. A 2 mm chamber was assembled between the coverslips and filled with a 20 mM HEPES pH 7.4 and 500 mM sucrose buffer through which a 10 Hz, 2.5 V sinusoidal current was passed for 2 hours. After formation, glucose was added to the GUV solution to 500 mM, forming an isomolar solution. Recombinant GFP-F-BAR domain and Rhodamine-Cdc12(residues 20-40) solutions were mixed with GUVs at a final concentration of 10 µM before imaging in a 0.5 mm chamber on the DeltaVision system described below.

Microscopy methods

Yeast for live-cell imaging were grown at 25°C. Live-cell images of *S. pombe* cells were acquired using a Personal DeltaVision (Cytiva Life Sciences) that includes a microscope (IX71; Olympus), 60× NA 1.42 Plan Apochromat and 100× NA 1.40 U Plan S Apochromat objectives, fixed and live-cell filter wheels, a camera (CoolSNAP HQ2; Photometrics), and softWoRx

imaging software (Cytiva Life Sciences). Z-sections were spaced at 0.5 μm. Images for quantification of *S. pombe* CR intensity were not deconvolved and were sum projected. Intensity measurements were made with FIJI (Schindelin et al., 2012). For CR measurements, a region of interest (ROI) was created to measure the intensity around the CR and background was subtracted by creating a ROI in the same image in an area containing no cells (Waters, 2009). For measurement of Rh-Cdc12 intensity on GUVs, a single Z-slice through the middle of the GUV was analyzed, determined as the slice where the diameter of the GUV was the greatest. The intensity was then measured for two concentric circles per GUV, one encompassing the entire GUV and one just below the surface of the membrane. To calculate the intensity of Rh-Cdc12 on the membrane only, the intensity of the inner circle was subtracted from the intensity of the outer circle, a background subtraction was performed, and the subtracted intensity was divided by the number of pixels (outer circle area subtracted by the inner circle area) to normalize for GUV size.

Time-lapse imaging was performed on log-phase cells at 29°C using an ONIX microfluidics perfusion system that allows for flow of YE media through the imaging chamber at 5 psi throughout the time-lapse. Time-lapse images were deconvolved with 10 iterations and visualized as maximum projections.

S. pombe samples for fPALM imaging were prepared as previously described (McDonald et al., 2017). Briefly, samples were prepared by enriching for cells with CRs by isolating newly separated short cells from a 7-30% lactose gradient, grown for 80 minutes in YE, labeled with 0.5 mM mCLING-ATTO647N (Revelo et al., 2014) (Synaptic Systems, Goettingen, Germany) for 10 minutes, and fixed in 3.7% formaldehyde for 15 minutes. Cells were washed 6x with PBS. For actin staining, fixed cells were incubated with 3.3 μM Phalloidin-Atto488, 0.01% NP-40 for 30 minutes and washed 3 times with PBS. Cells were resuspended with a small volume of PBS containing 1:100 diluted 80 nm gold particles (Microspheres-Nanospheres, Cold Spring, NY) and mounted on a 3% agar pad to prevent drift. For samples treated with inhibitor,

DMSO or 20 µg/mL FK506 (LC Laboratories) was added to media immediately after extraction from the lactose gradient, resulting in a treatment time of 90 minutes prior to fixation.

As described previously (McDonald et al., 2017), fPALM imaging was performed on a Nikon dSTORM 4.0 system including a Nikon Eclipse Ti microscope, 405, 488, 561, and 647 nm solid state lasers, a Hamamatsu ORCA-Flash4.0 camera, and a 100x CFI HP Apochromat TIRF 1.49NA objective with a 1.5x tubelens (110 nm pixel size). A 0°C laser angle focused at the center of cells in Z was used. The Nikon Perfect Focus system was engaged to minimize drift. The mMaple3 channel was imaged with simultaneous 0.1-0.5% 405 nm activation and 7.5% 561 nm excitation lasers, filtered through a polychroic mirror (ZT405/488/561/647rpc, Chroma, Bellows Falls, VT) and emission filter (ET585/65 m, Chroma), and captured with 30 ms exposures of 10-20k frames. The ATTO647N channel was imaged with simultaneous 0.2% 405 nm activation and 2% 647 nm excitation lasers, filtered through a polychroic mirror (ZT405/488/561/647rpc, Chroma) and emission filter (ET705/75 m, Chroma), and captured with 10 ms exposures over 15k frames. For Phalloidin-Atto488 imaging, simultaneous 0.2% 405nm activation and 2% 488 nm excitation lasers were used, filtered through a polychroic mirror (ZT405/488/561/647rpc, Chroma) and emission filter (ET525/50 m, Chroma), and captured with 10 ms exposures over 15k frames. Laser powers and exposure times were optimized for single photoactivated localizations per ring per frame.

fPALM images were analyzed as previously described (McDonald et al., 2017) using the ImageJ ThunderSTORM plugin (Ovesný et al., 2014). Images were pre-filtered with a wavelet B-spline filter and molecules were approximately localized with the 8-neighborhood local maximum method. Molecules were localized using the elliptical Gaussian weighted least squares method to identify precise lateral and Z positions. 0.1 µm Tetraspek beads were used for a Z-calibration (ThermoFisher). Fully formed pre-constriction CRs were identified in processed and aligned images as previously described (McDonald et al., 2017). The PM edge was identified using an automated threshold method to determine where mCLING-ATTO647N

signal drops to 5% of its maximum PM intensity (McDonald et al., 2017). Distances of each individual mMaple3 or Phalloidin-Atto488 localization to this edge were determined and these data were fit with a Gaussian curve with the MASS package in R (Kanchanawong et al., 2010; McDonald et al., 2017; Venables and Ripley, 2002). Distances from the PM (d_{center}), vertical width parameter (σ_{vert} or FWHM), and horizontal width parameter (σ_{width} or FWHM) were determined. d_{center} from multiple CRs analyzed were plotted using ggplot2 in R (McDonald et al., 2017).

Cdc15 F-BAR domain oligomerization was observed by negative stain electron microscopy as described previously (McDonald et al., 2015), 5 uL of 1 ug/mL Cdc15 F-BAR solution diluted into 50 mM NaCl, 20 mM Tris-HCl pH 7.4 was adsorbed to a glow discharged 200-mesh copper grid covered with carbon-coated collodion film (Electron Microscopy Services, Hatfield, PA). Grids were washed in two drops of water to remove unbound sample and stained with two drops of 0.75% uranyl formate (Ohi et al., 2004). Samples were imaged on a FEI Morgagni electron microscope operated at 100 kV and images were captured at 18,000-36,000X on a 1K x 1K CCD camera (AMT, Woburn, MA).

Quantification and statistical analysis

No statistical methods were used to pre-determine sample size. Details of statistical tests performed are described in the relevant figures, legends, and tables.

Chapter VI

Conclusions and future directions

Conclusions

Robust anchoring of the CR to the PM is critical for the integrity of cytokinesis and cell division. However, our knowledge of this process is incomplete. The work described in this dissertation represents a key advance in our mechanistic understanding of CR anchoring.

In Chapters II-IV, I discussed the evidence that PM PI(4,5)P_2 promotes CR anchoring in the cell center in *S. pombe*, and represents a CR anchoring mechanism distinct from those previously described (Snider et al., 2020b; Snider et al., 2018; Snider et al., 2017). When PI(4,5)P_2 levels are reduced, the CR slides away from its central position in a type V myosin-dependent manner, demonstrating for the first time that the CR experiences forces parallel to the long axis of the cell that can displace it.

In Chapter V, I discussed new insights into the mechanism by which the F-BAR protein Cdc15 acts as a CR-PM anchor. Using opposite faces, the Cdc15 F-BAR domain engages both the PM and formin Cdc12 simultaneously to link the actin of the CR to membrane (Snider et al., 2020a). Interestingly, the Cdc15 F-BAR domain scaffolds additional proteins with the cytosol-facing surface, including paxillin-like protein, Pxl1. Mutating the Cdc15 F-BAR scaffolding face not only disrupts the protein interaction network anchored by Cdc15, but also compresses the overall nanoscale architecture of the CR and compromises its function.

Future directions

How do the forces that generate CR sliding arise and how are they counteracted?

When PM PI(4,5)P_2 levels are reduced through genetic approaches (*efr3*Δ, *its3-1*), the CR slides away from its central position in ~50% of cells (Snider et al., 2018; Snider et al., 2017). The sliding motion requires the type V myosin Myo51, suggesting that force is required to move the CR. It remains unknown how these forces are generated. Considering that CR sliding events happen in ~50% of *efr3*Δ cells and that the CR has an equal likelihood of sliding toward either end of the cell, it seems likely that the force imbalances that result in CR sliding occur randomly. Because Myo51 is associated with both longitudinal actin cables and the CR, we proposed that CR-associated Myo51 may walk along actin cables to generate sliding. Although we have detected actin cables in close proximity to sliding CRs in *efr3*Δ, evidence either in support or in conflict with this model is lacking and is an exciting area of future study. In this model, perhaps Myo51 randomly accumulates to a greater extent on one side of the CR thus resulting in CR sliding. High-resolution (in both space and time) imaging techniques may inform what the Myo51 subcellular distribution is prior to and during CR sliding events.

The requirement for Myo51 to generate CR sliding implies that the forces parallel to the cell's long axis that generate CR sliding are present in wildtype cells. Presumably these forces are balanced and/or counteracted by protein anchors in wildtype such that the CR remains centrally positioned throughout cytokinesis. An alternative explanation is that Myo51 has increased activity or is less inhibited in cells with reduced PI(4,5)P_2, such that it is then able to generate increased force and move the CR; however there are currently no reports that Myo51 is regulated by PIPs.

In efforts to identify anchors that may act to counteract forces on the CR that generate sliding, we analyzed the localization of proteins containing membrane-binding domains in wildtype and *efr3*Δ. I have described three such proteins (Rgf1, Scd1, Opy1) that localize to the PM, but at reduced levels in *efr3*Δ and *its3-1* mutants in which PI(4,5)P_2 levels are reduced. It would be expected that if any of these identified candidates served as a key CR anchor, that those deletion phenotypes would be similar to *efr3*Δ. However, as described in Chapter III,

*opy1*Δ has only a mild off-center septation phenotype, and rarely displays CR sliding. *rgf1*Δ does not have off-center septa, and although *scd1*Δ does divide off-center, these cells have polarity defects unlike *efr3*Δ (Figure 6.1). Together this suggests that none of these three proteins alone can support $PI(4,5)P_2$-dependent CR anchoring. We suggest that CR anchoring may be accomplished through an ensemble of proteins that bind the PM sub-optimally in conditions where $PI(4,5)P_2$ is reduced. To test this model, identification of the full cohort of proteins with $PI(4,5)P_2$-dependent membrane localization is required, followed by an analysis of CR anchoring phenotypes in combinations of candidate mutations. In support of the idea that additional $PI(4,5)P_2$-sensitive PM proteins have not yet been identified, another protein, UNC-13/Munc13 protein Ync13, was reported to have reduced localization to the division site in *its3-1* since our study was reported (Zhu et al., 2018).

Another fascinating area of future study is exploring if our findings of the roles of $PI(4,5)P_2$ in CR anchoring in *S. pombe* are applicable in mammalian cell types. Depleting $PI(4,5)P_2$ in mammalian culture cells results in an increase in the frequency of cytokinesis failure, however the mechanism is undefined (Field et al., 2005). Perhaps CR-PM anchoring is disrupted in these conditions and time-lapse imaging will likely reveal if this is the case. Considering that PI4KIIIα and its scaffolding components are conserved (Baird et al., 2008; Chung et al., 2015), genetic manipulation of these scaffolding proteins in human cell types may complement previous studies by specifically disrupting PIP production at the PM.

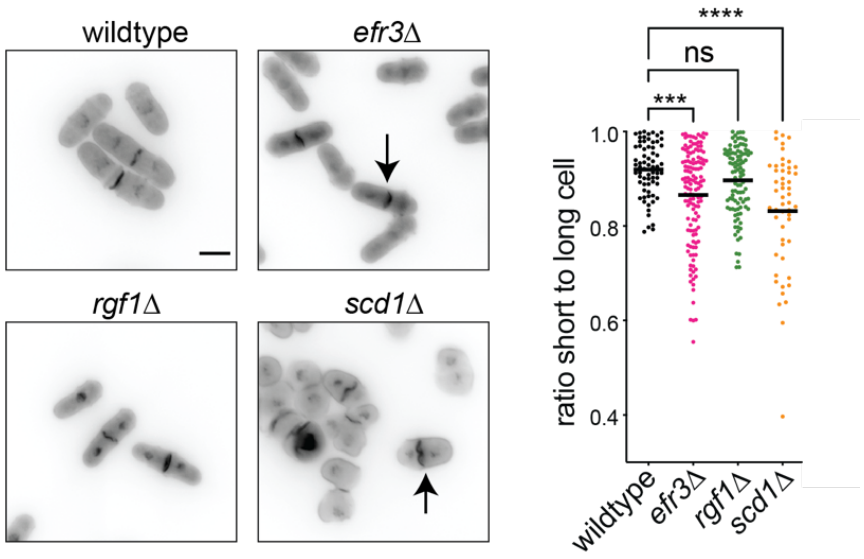

Figure 6.1. *rgf1*Δ and *scd1*Δ do not phenocopy *efr3*Δ. Left: Micrographs of DAPI and methyl blue stained cells of indicated genotypes. Arrows indicate cells with off-center septa. Scale bar = 5 μm. Right: Quantification of off-center septation, as measured by the ratio of the length of the short cell to the length of the long cell at septation. Bars depict median ratio. *** $p < 0.001$, **** $p < 0.0001$, ns = not significant $p > 0.2$; One-way ANOVA followed by Dunnett's multiple comparisons test.

Does Opy1 have another function, if not regulation of PI5-kinase Its3? How is Its3 regulated?

Although Opy1 negatively regulates the PI5-kinase Mss4 in *S. cerevisiae*, this work demonstrates that *S. pombe* Opy1 has no effect on PI5-kinase Its3 activity. Thus, it remains unknown what the physiological function(s) of *S. pombe* Opy1 is. Although we have demonstrated that Opy1 is a sensitive sensor of PM $PI(4,5)P_2$ and that its N-terminal PH domain mediates membrane-binding, a function for the C-terminal PH domain has not been identified. Perhaps Opy1 senses $PI(4,5)P_2$ through its N-terminal PH domain and then transmits that signal to another unknown molecule(s) through its C-terminal PH domain. It will be interesting to determine if Opy1 associates with other proteins, which may indicate unidentified functions. Proximity-based biotinylation assays (BioID) followed by mass spectrometry may prove useful in identifying the full Opy1 interactome by detecting transient interactions that were undetected in our Opy1-TAP analysis (Gingras et al., 2019; Roux et al., 2012).

We determined that Opy1 does not regulate Its3 kinase activity, leading to the question of what factors do regulate Its3. Interestingly, Its3 is negatively regulated when phosphorylated by the casein kinase Cki1 (Vancurova et al., 1999), however it is unknown what signals promote phosphorylation events and in which cellular contexts. Considering our findings that increased levels of $PI(4,5)P_2$ in the PM have no influence on cytokinesis, negative regulation of Its3 may not be required for proper completion of cell division, but may influence other processes. To potentially identify both positive and negative regulators of Its3, BioID assays and/or an Its3-TAP purification will likely provide candidates. In a preliminary Its3-BioID experiment, an uncharacterized DUF1769 (domain of unknown function) family protein, Spcc594.01, was identified as a candidate Its3 interactor. Interestingly, *spcc594.01*Δ has the off-center septation phenotype, indicating that it may be a regulator or effector of Its3 (Figure 6.2). These preliminary results indicate that additional proximity ligation assays and validation experiments will likely identify the Its3 interactome and reveal fascinating lipid kinase biology. Because of the sequence similarity and diverse roles of PI5-kinases in a variety of eukaryotic organisms from yeast to humans, elucidation of the factors that regulate Its3 is expected to further our understanding of PI5-kinases in different contexts.

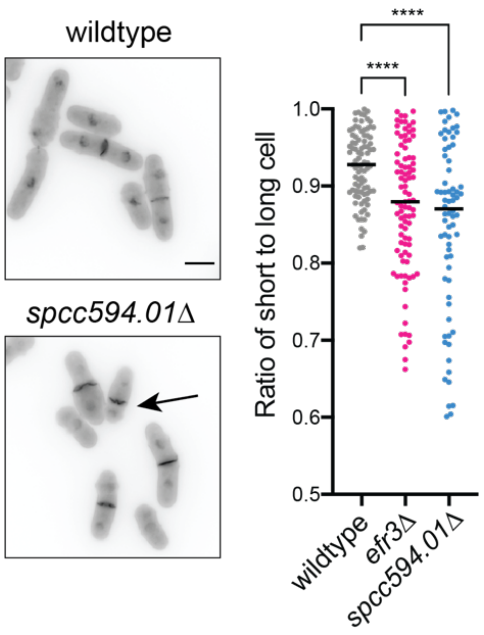

Figure 6.2. *spcc594.01*Δ, which encodes a candidate Its3 interactor, has an off-center septation phenotype. Left: Micrographs of DAPI and methyl blue stained cells of indicated genotypes. Arrow indicates a cell with off-center septum. Scale bar = 5 μm. Right: Quantification of off-center septation, as measured by the ratio of the length of the short cell to the length of the long cell at septation. Bars depict median ratio. **** $p < 0.0001$; One-way ANOVA followed by Dunnett's multiple comparisons test.

How do F-BAR domains dictate the nanoscale architecture of actin-based structures?

F-BAR domain binding partners have now been identified in a variety of cell types and processes; however few examples provide a complete mechanistic description of the structure and function of these F-BAR domain interactions. Here, we identified a completely different interaction mechanism between the formin Cdc12 and the Cdc15 F-BAR domain from those previously described. Cdc12 binds the cytosolic face of the F-BAR dimer (Snider et al., 2020a). This positioning allows the F-BAR domain to simultaneously bind the membrane and formin, positioning Cdc12 for F-actin nucleation at the division site. A homology model of the human PSTPIP1 F-BAR domain based on the FBP17 F-BAR domain structure reveals that negatively charged residues implicated in pyrin association are likely also on the convex side of the F-BAR

domain (Waite et al., 2009). Given these parallels, it will be interesting to determine if PSTPIP1 F-BAR domain also sandwiches itself between the membrane and a protein partner. Considering that most F-BAR domains use their concave faces for membrane-binding and tips for oligomerization, it is plausible that utilization of the convex face for protein binding is a general F-BAR feature.

Mutating the cytosolic scaffolding face of the Cdc15 F-BAR domain not only reduces recruitment of formin Cdc12 to the cytokinetic ring, but also results in loss of paxillin-like protein Pxl1 and protein phosphatase calcineurin (Snider et al., 2020a). Ordinarily, the components of the cytokinetic ring are stratified into layers arranged from the plasma membrane toward the cell interior (McDonald et al., 2017). Surprisingly, disruption of the protein interaction network organized by the Cdc15 F-BAR domain collapses this architecture such that even components normally hundreds of nanometers away localize closer to the membrane.

Although the mechanism explaining how the Cdc15 F-BAR domain influences the nanoscale architecture of the cytokinetic ring is not yet clear, it is likely through binding partners. Pxl1 binds the Cdc15 F-BAR domain, but it also binds the Cdc15 C-terminal SH3 domain (Snider et al., 2020a). Because the Cdc15 F-BAR and SH3 domains occupy distinct spatial zones within the cytokinetic ring (McDonald et al., 2017), it may be that Pxl1 displaces the Cdc15 SH3 domain away from the plasma membrane. Although this has not yet been tested, there is precedent for the existence of proteins that bind multiple sites within an F-BAR protein. Dap160/intersectin interacts with both the F-BAR and SH3 domains of Nwk at sites of synaptic endocytosis in *D. melanogaster* (Del Signore et al., 2020) and pyrin requires both the F-BAR domain and SH3 domain to bind PSTPIP1 in human blood cells (Shoham et al., 2003). Although the PSTPIP1 SH3 domain is dispensable for pyrin-mediated PSTPIP1 localization to the inflammasome (Waite et al., 2009), it may need to be engaged by pyrin for PSTPIP1 function. Determining if proteins generally modulate the overall conformation and function of F-BAR

proteins via multivalent interactions will likely inform how they are regulated at actin-based structures.

In order to test if Pxl1 influences the conformation of Cdc15 within the CR in this way, it will first be necessary to determine how Pxl1 engages with two Cdc15 binding sites. Notably, Pxl1 contains a motif in its N-terminus that is similar in sequence to the Cdc12 motif that mediates F-BAR domain binding (Figure 6.3A). In preliminary binding assays, a peptide containing this Pxl1 motif (residues 3-27) is sufficient to interact with the Cdc15 F-BAR domain, and mutation of proline 18 to alanine (analogous to Cdc12-P31A) disrupts this interaction (Figure 6.3B). Considering the similarity between the Cdc12 and Pxl1 F-BAR binding motifs, it is likely that one molecule of Pxl1 engages one F-BAR dimer as in the case of Cdc12. Additionally, one would expect that these two motifs can compete for F-BAR domain binding sites, however the large abundance of Cdc15 in the CR may indicate that competition is not necessary. These models will be tested in future studies. Although the details of how Pxl1 binds the Cdc15 C-terminus have not yet been determined, it is likely that one or more of the PxxP motifs in the Pxl1 N-terminus mediate this binding event, considering that the Cdc15-W903S mutant, which disrupts canonical SH3-PxxP interactions, greatly reduces Pxl1-Cdc15 C-terminus association (Bhattacharjee et al., 2020). It is unknown if Pxl1 can bind both the Cdc15 F-BAR and SH3 binding sites simultaneously, but this will be an important aspect of the model that Pxl1 modulates Cdc15 conformation to test.

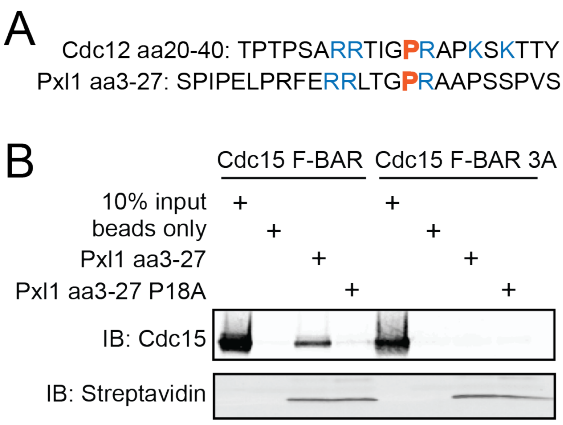

Figure 6.3. Like Cdc12, Pxl1 contains an N-terminal F-BAR binding motif. (A) Amino acid sequences of the F-BAR binding motifs from Cdc12 and Pxl1. The prolines critical for interaction are highlighted in orange, basic residues in blue. (B) in vitro binding assay with biotinylated Pxl1 peptides (aa3-27) wildtype and P18A and Cdc15 F-BAR domain wildtype and 3A. Proteins associated with streptavidin resin after the binding reaction were separated by SDS-PAGE and analyzed by immunoblotting with indicated antibodies.

Another possible explanation for the CR defects in *cdc15* F-BAR scaffolding mutants is mis-regulated signaling in the absence of calcineurin. PSTPIP1 also facilitates signaling, by bringing a phosphatase and a substrate into proximity. PSTPIP1 binds the protein tyrosine phosphatase PEST through its F-BAR domain and the c-abl kinase through its C-terminal SH3 domain (Cong et al., 2000). These binding events promote efficient c-abl dephosphorylation by PEST and thus regulate c-abl kinase activity. To test if Cdc15 works analogously to bring calcineurin and its substrates together, the full cohort of calcineurin substrates at the CR will first need to be identified. With a powerful combination of techniques including in vitro phage display, in vivo BioID assays, and in silico prediction of calcineurin docking motifs, a large set of calcineurin substrates were defined and validated in human cells (Wigington et al., 2020). Because of the high degree of sequence similarity of calcineurin throughout evolution (Thewes, 2014), these tools will likely allow for the identification of calcineurin substrates in *S. pombe*.

Substrates identified that localize to the CR will be top candidates for drivers of CR architecture and function.

In this work, I have focused on the role of the Cdc15 F-BAR domain in driving the architecture of the CR during cytokinesis. However, F-BAR domains act as platforms for building actin-based structures in other biological contexts as well. The FCHSD2 F-BAR domain localizes to the base of clathrin coated pits in human cells, and is important for coordinating actin polymerization at these structures (Almeida-Souza et al., 2018a). Similarly, the coordinated interactions of Dap160 and WASp with Nwk promote F-actin assembly during synaptic endocytosis in *D. melanogaster* (Del Signore et al., 2020). In *S. cerevisiae,* Hof1 plays a role in linking F-actin cables to the septin network at the bud neck, which is crucial for proper nanoscale spacing of actin cables (Garabedian et al., 2020). It will be interesting to explore if other F-BAR domain networks at membranes influence the nanoscale architecture of the actin-based structures they support.

REFERENCES

Abe, M., A. Makino, F. Hullin-Matsuda, K. Kamijo, Y. Ohno-Iwashita, K. Hanada, H. Mizuno, A. Miyawaki, and T. Kobayashi. 2012. A role for sphingomyelin-rich lipid domains in the accumulation of phosphatidylinositol-4, 5-bisphosphate to the cleavage furrow during cytokinesis. *Molecular and cellular biology*. 32:1396-1407.

Abrams, C.S., J. Zhang, C.P. Downes, X.-w. Tang, W. Zhao, and S.E. Rittenhouse. 1996. Phosphopleckstrin Inhibits Gβγ-activable Platelet Phosphatidylinositol-4,5-bisphosphate 3-Kinase. *Journal of Biological Chemistry*. 271:25192-25197.

Almeida-Souza, L., R.A.W. Frank, J. Garcia-Nafria, A. Colussi, N. Gunawardana, C.M. Johnson, M.M. Yu, G. Howard, B. Andrews, Y. Vallis, and H.T. McMahon. 2018a. A Flat BAR Protein Promotes Actin Polymerization at the Base of Clathrin-Coated Pits. *Cell*. 174:325-337.

Almeida-Souza, L., R.A.W. Frank, J. García-Nafría, A. Colussi, N. Gunawardana, C.M. Johnson, M. Yu, G. Howard, B. Andrews, Y. Vallis, and H.T. McMahon. 2018b. A Flat BAR Protein Promotes Actin Polymerization at the Base of Clathrin-Coated Pits. *Cell*. 174:325-337.e314.

Arai, R., and I. Mabuchi. 2002. F-actin ring formation and the role of F-actin cables in the fission yeast S*chizosaccharomyces pombe*. *Journal of Cell Science*. 115:887-898.

Arasada, R., and T.D. Pollard. 2014. Contractile Ring Stability in S. pombe Depends on F-BAR Protein Cdc15p and Bgs1p Transport from the Golgi Complex. *Cell Reports*. 8:1533--1544.

Atilgan, E., V. Magidson, A. Khodjakov, and F. Chang. 2015. Morphogenesis of the Fission Yeast Cell through Cell Wall Expansion. *Current Biology*. 25:2150--2157.

Audhya, A., and S.D. Emr. 2002. Stt4 PI 4-kinase localizes to the plasma membrane and functions in the Pkc1-mediated MAP kinase cascade. *Developmental Cell*. 2:593--605.

Bach, T.L., W.T. Kerr, Y. Wang, E.M. Bauman, P. Kine, E.L. Whiteman, R.S. Morgan, E.K. Williamson, E.M. Ostap, J.K. Burkhardt, G.A. Koretzky, M.J. Birnbaum, and C.S. Abrams. 2006. PI3K regulates pleckstrin-2 in T-cell cytoskeletal reorganization. *Blood*. 109:1147-1155.

Baird, D., C. Stefan, A. Audhya, S. Weys, and S.D. Emr. 2008. Assembly of the PtdIns 4-kinase Stt4 complex at the plasma membrane requires Ypp1 and Efr3. *Journal of Cell Biology*. 183:1061--1074.

Balasubramanian, M.K., D. McCollum, L. Chang, K.C.Y. Wong, N.I. Naqvi, X. He, S. Sazer, and K.L. Gould. 1998. Isolation and characterization of new fission yeast cytokinesis mutants. *Genetics*. 149:1265--1275.

Basi, G., E. Schmid, and K. Maundrell. 1993. TATA box mutations in the Schizosaccharomyces pombe nmt1 promoter affect transcription efficiency but not the transcription start point or thiamine repressibility. *Gene*. 123:131-136.

Becalska, A.N., C.F. Kelley, C. Berciu, T.B. Stanishneva-Konovalova, X.F. Fu, S.Y. Wang, O.S. Sokolova, D. Nicastro, and A.A. Rodal. 2013. Formation of membrane ridges and scallops by the F-BAR protein Nervous Wreck. *Molecular Biology of the Cell*. 24:2406-2418.

Begonja, A.J., F.G. Pluthero, W. Suphamungmee, S. Giannini, H. Christensen, R. Leung, R.W. Lo, F. Nakamura, W. Lehman, M. Plomann, K.M. Hoffmeister, W.H.A. Kahr, J.H. Hartwig, and H. Falet. 2015. FlnA binding to PACSIN2 F-BAR domain regulates membrane tubulation in megakaryocytes and platelets. *Blood*. 126:80-88.

Bhattacharjee, R., M.C. Mangione, M. Wos, J.-S. Chen, C.E. Snider, R.H. Roberts-Galbraith, N.A. McDonald, L.L. Presti, S.G. Martin, and K.L. Gould. 2020. DYRK kinase Pom1 drives F-BAR protein Cdc15 from the membrane to promote medial division. *Molecular Biology of the Cell*. 31:917-929.

Bohnert, K.A., and K.L. Gould. 2011. On the cutting edge: post-translational modifications in cytokinesis. *Trends in Cell Biology*. 21:283--292.

Botelho, R.J., J.A. Efe, D. Teis, and S.D. Emr. 2008. Assembly of a Fab1 phosphoinositide kinase signaling complex requires the Fig4 phosphoinositide phosphatase. *Molecular biology of the cell*. 19:4273-4286.

Brill, J.A., G.R. Hime, M. Scharer-Schuksz, and M.T. Fuller. 2000. A phospholipid kinase regulates actin organization and intercellular bridge formation during germline cytokinesis. *Development*. 127:3855-3864.

Bähler, J., and J.R. Pringle. 1998. Pom1p, a fission yeast protein kinase that provides positional information for both polarized growth and cytokinesis. *Genes and Development*. 12:1356--1370.

Bähler, J., A.B. Steever, S. Wheatley, Y.L. Wang, J.R. Pringle, K.L. Gould, and D. McCollum. 1998a. Role of Polo kinase and Mid1p in determining the site of cell division in fission yeast. *Journal of Cell Biology*. 143:1603--1616.

Bähler, J., J.Q. Wu, M.S. Longtine, N.G. Shah, A. McKenzie, A.B. Steever, A. Wach, P. Philippsen, and J.R. Pringle. 1998b. Heterologous modules for efficient and versatile PCR-based gene targeting in Schizosaccharomyces pombe. *Yeast*. 14:943--951.

Carman, P.J., and R. Dominguez. 2018. BAR domain proteins—a linkage between cellular membranes, signaling pathways, and the actin cytoskeleton. *Biophysical Reviews*. 10:1587-1604.

Carnahan, R.H., and K.L. Gould. 2003. The PCH family protein, Cdc15p, recruits two F-actin nucleation pathways to coordinate cytokinetic actin ring formation in Schizosaccharomyces pombe. *Journal of Cell Biology*. 162:851--862.

Carpy, A., K. Krug, S. Graf, A. Koch, S. Popic, S. Hauf, and B. Macek. 2014. Absolute proteome and phosphoproteome dynamics during the cell cycle of fission yeast. *Molecular & Cellular Proteomics*:1925--1936.

Celton-Morizur, S., N. Bordes, V. Fraisier, P.T. Tran, and A. Paoletti. 2004. C-Terminal Anchoring of mid1p to Membranes Stabilizes Cytokinetic Ring Position in Early Mitosis in Fission Yeast. *Molecular and Cellular Biology*. 24:10621--10635.

Chang, F., A. Woollard, and P. Nurse. 1996. Isolation and characterization of fission yeast mutants defective in the assembly and placement of the contractile actin ring. *Journal of Cell Science*. 109 (Pt 1:131--142.

Chardwiriyapreecha, S., K. Manabe, T. Iwaki, M. Kawano-Kawada, T. Sekito, S. Lunprom, K. Akiyama, K. Takegawa, and Y. Kakinuma. 2015. Functional expression and characterization of Schizosaccharomyces pombe Avt3p as a vacuolar amino acid exporter in Saccharomyces cerevisiae. *PloS one*. 10:e0130542.

Cheffings, T.H., N.J. Burroughs, and M.K. Balasubramanian. 2016. Actomyosin Ring Formation and Tension Generation in Eukaryotic Cytokinesis. *Current Biology*. 26:R719-R737.

Chen, J.-S., J.R. Beckley, N.A. McDonald, L. Ren, M. Mangione, S.J. Jang, Z.C. Elmore, N. Rachfall, A. Feoktistova, C.M. Jones, A.H. Willet, R. Guillen, D.A. Bitton, J. Bähler, M.A. Jensen, N. Rhind, and K.L. Gould. 2015. Identification of New Players in Cell Division, DNA Damage Response, and Morphogenesis Through Construction of Schizosaccharomyces pombe Deletion Strains. *G3-Genes|Genomes|Genetics*. 5:361--370.

Chen, J.-S., M.R. Broadus, J.R. McLean, A. Feoktistova, L. Ren, and K.L. Gould. 2013. Comprehensive proteomics analysis reveals new substrates and regulators of the fission yeast clp1/cdc14 phosphatase. *Molecular & Cellular Proteomics*. 12:1074--1086.

Chen, V.B., W.B. Arendall, III, J.J. Headd, D.A. Keedy, R.M. Immormino, G.J. Kapral, L.W. Murray, J.S. Richardson, and D.C. Richardson. 2010. MolProbity: all-atom structure validation for macromolecular crystallography. *Acta Crystallographica Section D*. 66:12-21.

Chung, J., F. Nakatsu, J.M. Baskin, and P. De Camilli. 2015. Plasticity of PI4KIIIa interactions at the plasma membrane. *EMBO reports*. 16:312--320.

Clubb, F.J.J.a.B.S.P. 1984. Formation of binucleated myocardial cells in the neonatal rat. An index for growth hypertrophy. *Lab Invest*. 50:571--577.

Cong, F., S. Spencer, J.-F. Côté, Y. Wu, M.L. Tremblay, L.A. Lasky, and S.P. Goff. 2000. Cytoskeletal Protein PSTPIP1 Directs the PEST-Type Protein Tyrosine Phosphatase to the c-Abl Kinase to Mediate Abl Dephosphorylation. *Molecular Cell*. 6:1413-1423.

Cortés, J.C.G., N. Pujol, M. Sato, M. Pinar, M. Ramos, M. Belén, M. Osumi, R.J. Carlos, and P. Peréz. 2015. Cooperation between Paxillin-like Protein Pxl1 and Glucan Synthase Bgs1 Is Essential for Actomyosin Ring Stability and Septum Formation in Fission Yeast. *PLoS Genetics*. 11:1--24.

Dambournet, D., M. Machicoane, L. Chesneau, M. Sachse, M. Rocancourt, A. El Marjou, E. Formstecher, R. Salomon, B. Goud, and A. Echard. 2011. Rab35 GTPase and OCRL phosphatase remodel lipids and F-actin for successful cytokinesis. *Nature Cell Biology*. 13:981--988.

Davidson, R., J.A. Pontasch, and J.-Q. Wu. 2016. Sbg1 Is a Novel Regulator for the Localization of the β-Glucan Synthase Bgs1 in Fission Yeast. *PLoS One*. 11:e0167043.

Del Signore, S.J., C.F. Kelley, E.M. Messelaar, T. Lemos, M.F. Marchan, B. Ermanoska, M. Mund, M. Kaksonen, and A.A. Rodal. 2020. Autoregulation clamps the synaptic membrane-remodeling machinery and promotes productive actin-dependent endocytosis. *bioRxiv*:2020.2003.2006.981076.

Dickson, E.J., and B. Hille. 2019. Understanding phosphoinositides: rare, dynamic, and essential membrane phospholipids. *Biochemical Journal*. 476:1-23.

Dowler, S., R.A. Currie, D.G. Campbell, M. Deak, G. Kular, C.P. Downes, and D.R. Alessi. 2000. Identification of pleckstrin-homology-domain-containing proteins with novel phosphoinositide-binding specificities. *Biochemical Journal*. 351:19-31.

Echard, A. 2012. Phosphoinositides and cytokinesis: The “PIP” of the iceberg. *Cytoskeleton*. 69:893--912.

Edlich, C., G. Stier, B. Simon, M. Sattler, and C. Muhle-Goll. 2005. Structure and Phosphatidylinositol-(3,4)- Bisphosphate Binding of the C-Terminal PH Domain of Human Pleckstrin. *Structure*. 13:277-286.

Eggert, U.S., A.A. Kiger, C. Richter, Z.E. Perlman, N. Perrimon, T.J. Mitchison, and C.M. Field. 2004. Parallel chemical genetic and genome-wide RNAi screens identify cytokinesis inhibitors and targets. *PLoS Biology*. 2:e379.

El Kadhi, K.B., C. Roubinet, S. Solinet, G. Emery, and S. Carréno. 2011. The inositol 5-phosphatase dOCRL controls PI (4, 5) P2 homeostasis and is necessary for cytokinesis. *Current Biology*. 21:1074-1079.

Elmore, Z.C., J.R. Beckley, Chen Jun-Song, and K.L. Gould. 2014. Histone H2B ubiquitination promotes the function of the anaphase-promoting complex/cyclosome in Schizosaccharomyces pombe. *G3: Genes|Genomes|Genetics*. 4:1529--1538.

Emoto, K., H. Inadome, Y. Kanaho, S. Narumiya, and M. Umeda. 2005. Local change in phospholipid composition at the cleavage furrow is essential for completion of cytokinesis. *Journal of Biological Chemistry*. 280:37901--37907.

Emsley, P., B. Lohkamp, W.G. Scott, and K. Cowtan. 2010. Features and development of Coot. *Acta Crystallographica Section D: Biological Crystallography*. 66:486-501.

Fankhauser, C., A. Reymond, L. Cerutti, S. Utzig, K. Hofmann, and V. Simanis. 1995. The S. pombe cdc15 gene is a key element in the reorganization of F-actin at mitosis. *Cell*. 82:435--444.

Field, S.J., N. Madson, M.L. Kerr, K.A.A. Galbraith, C.E. Kennedy, M. Tahiliani, A. Wilkins, and L.C. Cantley. 2005. PtdIns(4,5)P2 Functions at the Cleavage Furrow during Cytokinesis. *Current Biology*. 15:1407--1412.

Frost, A., P. De Camilli, and V.M. Unger. 2007. F-BAR Proteins Join the BAR Family Fold. *Structure*. 15:751--753.

Frost, A., R. Perera, A. Roux, K. Spasov, O. Destaing, E.H. Egelman, P. De Camilli, and V.M. Unger. 2008. Structural basis of membrane invagination by F-BAR domains. *Cell*. 132:807-817.

Fujita, M., R. Sugiura, Y. Lu, L. Xu, Y. Xia, H. Shuntoh, and T. Kuno. 2002. Genetic Interaction Between Calcineurin and Type 2 Myosin and Their Involvement in the Regulation of Cytokinesis and Chloride Ion Homeostasis in Fission Yeast. *Genetics*. 161:971.

Fujiwara, T., M. Bandi, M. Nitta, E.V. Ivanova, R.T. Bronson, and D. Pellman. 2005. Cytokinesis failure generating tetraploids promotes tumorigenesis in p53-null cells. *Nature*. 437:1043--1047.

Ganem, N.J., S.A. Godinho, and D. Pellman. 2009. A mechanism linking extra centrosomes to chromosomal instability. *Nature*. 460:278--282.

Garabedian, M.V., T. Stanishneva-Konovalova, C. Lou, T.J. Rands, L.W. Pollard, O.S. Sokolova, and B.L. Goode. 2018. Integrated control of formin-mediated actin assembly by a stationary inhibitor and a mobile activator. *Journal of Cell Biology*. 217:3512-3530.

Garabedian, M.V., A. Wirshing, A. Vakhrusheva, B. Turegun, O.S. Sokolova, and B.L. Goode. 2020. A septin-Hof1 scaffold at the yeast bud neck binds and organizes actin cables. *Molecular Biology of the Cell*. 31:1988-2001.

Ge, W., and M.K. Balasubramanian. 2008. Pxl1p, a Paxillin-related protein, stabilizes the actomyosin ring during cytokinesis in fission yeast. *Molecular Biology of the Cell*. 19:1680--1692.

Gingras, A.-C., K.T. Abe, and B. Raught. 2019. Getting to know the neighborhood: using proximity-dependent biotinylation to characterize protein complexes and map organelles. *Current Opinion in Chemical Biology*. 48:44-54.

Gould, G.W. 2016. Animal cell cytokinesis: the role of dynamic changes in the plasma membrane proteome and lipidome. *In Seminars in Cell & Developmental Biology*. Vol. 53. Elsevier. 64-73.

Gould, K.L., S. Moreno, D.J. Owen, S. Sazer, and P. Nurse. 1991. Phosphorylation at Thr167 is required for Schizosaccharomyces pombe p34cdc2 function. *EMBO J*. 10:3297-3309.

Gould, K.L., L. Ren, A.S. Feoktistova, J.L. Jennings, and A.J. Link. 2004. Tandem affinity purification and identification of protein complex components. *Methods*. 33:239--244.

Goyal, A., M. Takaine, V. Simanis, and K. Nakano. 2011. Dividing the spoils of growth and the cell cycle: The fission yeast as a model for the study of cytokinesis . *Cytoskeleton*. 68:69-88.

Gray, A., J. Van der Kaay, and C.P. Downes. 1999. The pleckstrin homology domains of protein kinase B and GRP1 (general receptor for phosphoinositides-1) are sensitive and selective probes for the cellular detection of phosphatidylinositol 3, 4-bisphosphate and/or phosphatidylinositol 3, 4, 5-trisphosphate in vivo. *Biochemical Journal*. 344:929-936.

Graziano, B.R., H.-Y.E. Yu, S.L. Alioto, J.A. Eskin, C.A. Ydenberg, D.P. Waterman, M. Garabedian, and B.L. Goode. 2014. The F-BAR protein Hof1 tunes formin activity to sculpt actin cables during polarized growth. *Molecular Biology of the Cell*. 25:1730-1743.

Guertin, D.A., S. Trautmann, and D. McCollum. 2002. Cytokinesis in Eukaryotes. *Microbiology and Molecular Biology Reviews*. 66:155.

Hachet, O., M. Berthelot-Grosjean, K. Kokkoris, V. Vincenzetti, J. Moosbrugger, and S.G. Martin. 2011. A phosphorylation cycle shapes gradients of the DYRK family kinase pom1 at the plasma membrane. *Cell*. 145:1116--1128.

Hachet, O., and V. Simanis. 2008. Mid1p/anillin and the septation initiation network orchestrate contractile ring assembly for cytokinesis. *Genes & Development*. 22:3205-3216.

Hanawa-Suetsugu, K., Y. Itoh, M. Ab Fatah, T. Nishimura, K. Takemura, K. Takeshita, S. Kubota, N. Miyazaki, W.N.I. Wan Mohamad Noor, T. Inaba, N.T.H. Nguyen, S. Hamada-Nakahara, K. Oono-Yakura, M. Tachikawa, K. Iwasaki, D. Kohda, M. Yamamoto, A. Kitao, A. Shimada, and S. Suetsugu. 2019. Phagocytosis is mediated by two-dimensional assemblies of the F-BAR protein GAS7. *Nature Communications*. 10:4763.

Harlan, J.E., P.J. Hajduk, H.S. Yoon, and S.W. Fesik. 1994. Pleckstrin homology domains bind to phosphatidylinositol-4, 5-bisphosphate. *Nature*. 371:168-170.

Harlan, J.E., H.S. Yoon, P.J. Hajduk, and S.W. Fesik. 1995. Structural characterization of the interaction between a pleckstrin homology domain and phosphatidylinositol 4, 5-bisphosphate. *Biochemistry*. 34:9859-9864.

Hayashi, M.T., and J. Karlseder. 2013. DNA damage associated with mitosis and cytokinesis failure. *Oncogene*. 32:4593--4601.

Hayles, J., V. Wood, L. Jeffery, K.-L. Hoe, D.-U. Kim, H.-O. Park, S. Salas-Pino, C. Heichinger, and P. Nurse. 2013. A genome-wide resource of cell cycle and cell shape genes of fission yeast. *Open biology*. 3:130053.

Henne, W.M., H.M. Kent, M.G.J. Ford, B.G. Hegde, O. Daumke, P.J.G. Butler, R. Mittal, R. Langen, P.R. Evans, and H.T. McMahon. 2007. Structure and Analysis of FCHo2 F-BAR Domain: A Dimerizing and Membrane Recruitment Module that Effects Membrane Curvature. *Structure*. 15:839--852.

Higgs, H.N., and T.D. Pollard. 2000. Activation by Cdc42 and PIP2 of Wiskott-Aldrich syndrome protein (WASp) stimulates actin nucleation by Arp2/3 complex. *The Journal of cell biology*. 150:1311-1320.

Ho, H.Y.H., R. Rohatgi, A.M. Lebensohn, L. Ma, J.X. Li, S.P. Gygi, and M.W. Kirschner. 2004. Toca-1 mediates Cdc42-dependent actin nucleation by activating the N-WASP-WIP complex. *Cell*. 118:203-216.

Hosomi, A., Y.-Y. Kawanishi, N. Tanaka, and K. Takegawa. 2008. PXA domain-containing protein Pxa1 is required for normal vacuole function and morphology in Schizosaccharomyces pombe. *Bioscience, biotechnology, and biochemistry*. 72:548-556.

Huang, J., Y. Huang, H. Yu, D. Subramanian, A. Padmanabhan, R. Thadani, Y. Tao, X. Tang, R. Wedlich-Soldner, and M.K. Balasubramanian. 2012. Nonmedially assembled F-actin cables incorporate into the actomyosin ring in fission yeast. *Journal of Cell Biology*. 199:831--847.

Huang, Y., H. Yan, and M.K. Balasubramanian. 2008. Assembly of normal actomyosin rings in the absence of Mid1p and cortical nodes in fi ssion yeast. *Journal of Cell Biology*. 183:979--988.

Itoh, T., and P. De Camilli. 2006. BAR, F-BAR (EFC) and ENTH/ANTH domains in the regulation of membrane–cytosol interfaces and membrane curvature. *Biochimica et Biophysica Acta (BBA) - Molecular and Cell Biology of Lipids*. 1761:897-912.

Itoh, T., K.S. Erdmann, A. Roux, B. Habermann, H. Werner, and P. De Camilli. 2005. Dynamin and the Actin Cytoskeleton Cooperatively Regulate Plasma Membrane Invagination by BAR and F-BAR Proteins. *Developmental Cell*. 9:791-804.

Janetopoulos, C., J. Borleis, F. Vazquez, M. Iijima, and P. Devreotes. 2005. Temporal and spatial regulation of phosphoinositide signaling mediates cytokinesis. *Developmental cell*. 8:467-477.

Kabeche, R., A. Roguev, N.J. Krogan, and J.B. Moseley. 2014. A Pil1–Sle1–Syj1–Tax4 functional pathway links eisosomes with PI (4, 5) P2 regulation. *J Cell Sci*. 127:1318-1326.

Kanchanawong, P., G. Shtengel, A.M. Pasapera, E.B. Ramko, M.W. Davidson, H.F. Hess, and C.M. Waterman. 2010. Nanoscale architecture of integrin-based cell adhesions. *Nature*. 468:580-584.

Kawano, F., H. Suzuki, A. Furuya, and M. Sato. 2015. Engineered pairs of distinct photoswitches for optogenetic control of cellular proteins. *Nature communications*. 6:6256.

Keeney, J.B., and J.D. Boeke. 1994a. Efficient targeted integration at leu1-32 and ura4-294 in *Schizosaccharomyces pombe*. *Genetics*. 136:849-856.

Keeney, J.B., and J.D. Boeke. 1994b. Efficient targeted integration at leu1-32 and ura4-294 in Schizosaccharomyces pombe. *Genetics*. 136:849--856.

Kettenbach, A.N., L. Deng, Y. Wu, S. Baldissard, M.E. Adamo, S.A. Gerber, and J.B. Moseley. 2015. Quantitative Phosphoproteomics Reveals Pathways for Coordination of Cell Growth and Division by the Conserved Fission Yeast Kinase Pom1. *Molecular & Cellular Proteomics*. 14:1275.

Kim, D.U., J. Hayles, V. Wood, P.H.M.O. J., M. Won, H.S. Yoo, T. Duhig, M. Nam, G. Palmer, S. Han, L. Jeffery, S.T. Baek, H. Lee, Y.S. Shim, M. Lee, L. Kim, K.S. Heo, E.J. Noh, A.R. Lee, Y.J. Jang, K.S. Chung, S.J. Choi, J.Y. Park, Y. Park, H.M.B. Kim, S.K. Park, E.J. Kang, H.S. Kang, K. Kim, K.B. Song, P. Nurse, and K.L. Hoe. 2010. Analysis of a genome-wide set of gene deletions in the fission yeast Schizosaccharomyces pombe. *Nature Biotechnology*. 28:617--623.

Kitayama, C., A. Sugimoto, and M. Yamamoto. 1997. Type II Myosin Heavy Chain Encoded by the m*yo2* Gene Composes the Contractile Ring during Cytokinesis in S*chizosaccharomyces pombe*. *Journal of Cell Biology* 137:1309-1319.

Klein, D.E., A. Lee, D.W. Frank, M.S. Marks, and M.A. Lemmon. 1998. The Pleckstrin Homology Domains of Dynamin Isoforms Require Oligomerization for High Affinity Phosphoinositide Binding. *Journal of Biological Chemistry*. 273:27725-27733.

Kostan, J., U. Salzer, A. Orlova, I. Törö, V. Hodnik, Y. Senju, J. Zou, C. Schreiner, J. Steiner, J. Meriläinen, M. Nikki, I. Virtanen, O. Carugo, J. Rappsilber, P. Lappalainen, V.-P. Lehto,

G. Anderluh, E.H. Egelman, and K. Djinović-Carugo. 2014. Direct interaction of actin filaments with F-BAR protein pacsin2. *EMBO reports*. 15:1154-1162.

Kouranti, I., M. Sachse, N. Arouche, B. Goud, and A. Echard. 2006. Rab35 regulates an endocytic recycling pathway essential for the terminal steps of cytokinesis. *Current biology*. 16:1719-1725.

Krajcovic, M., N.B. Johnson, Q. Sun, G. Normand, N. Hoover, E. Yao, A.L. Richardson, R.W. King, E.S. Cibas, S.J. Schnitt, J.S. Brugge, and M. Overholtzer. 2011. A non-genetic route to aneuploidy in human cancers. *Nature Cell Biology*. 13:324--330.

Krissinel, E., and K. Henrick. 2007. Inference of Macromolecular Assemblies from Crystalline State. *Journal of Molecular Biology*. 372:774-797.

Lacroix, B., and A.S. Maddox. 2012. Cytokinesis, ploidy and aneuploidy. *Journal of Pathology*. 226:338--351.

Laporte, D., V.C. Coffman, I.J. Lee, and J.Q. Wu. 2011. Assembly and architecture of precursor nodes during fission yeast cytokinesis. *Journal of Cell Biology*. 192:1005--1021.

Laskowski, R.A., M.W. MacArthur, D.S. Moss, and J.M. Thornton. 1993. PROCHECK: a program to check the stereochemical quality of protein structures. *Journal of Applied Crystallography*. 26:283-291.

Lee, B., and F.M. Richards. 1971. The interpretation of protein structures: Estimation of static accessibility. *Journal of Molecular Biology*. 55:379-IN374.

Lee, I.-J., V.C. Coffman, and J.-Q. Wu. 2012. Contractile-Ring Assembly in Fission Yeast Cytokinesis: Recent Advances and New Perspectives. *Cytoskeleton*. 69:751-763.

Lee, M.E., S.F. Rusin, N. Jenkins, A.N. Kettenbach, and J.B. Moseley. 2018. Mechanisms Connecting the Conserved Protein Kinases Ssp1, Kin1, and Pom1 in Fission Yeast Cell Polarity and Division. *Current Biology*. 28:84-92.e84.

Lemmon, M.A. 2007. Pleckstrin homology (PH) domains and phosphoinositides. *Biochemical Society symposium*:81-93.

Li, F., X. Wang, J.M. Capasso, and A.M. Gerdes. 1996. Rapid transition of cardiac myocytes from hyperplasia to hypertrophy during postnatal development. *Journal of Molecular and Cellular Cardiology*. 28:1737--1746.

Li, F., X. Wang, and A.M. Gerdes. 1997. Formation of binucleated cardiac myocytes in rat heart: II. Cytoskeletal organisation. *Journal of Molecular and Cellular Cardiology*. 29:1553--1565.

Li, K. The image stabilizer plugin for ImageJ., http://www.cs.cmu.edu/~kangli/code/Image_Stabilizer.html.

Ling, Y., C.J. Stefan, J.A. MacGurn, A. Audhya, and S.D. Emr. 2012. The dual PH domain protein Opy1 functions as a sensor and modulator of PtdIns(4,5)P2 synthesis. *The EMBO journal*. 31:2882--2894.

Liu, J., G.D. Fairn, D.F. Ceccarelli, F. Sicheri, and A. Wilde. 2012. Cleavage furrow organization requires PIP2-mediated recruitment of anillin. *Current biology*. 22:64-69.

Liu, Y., N.A. McDonald, S.M. Naegele, K.L. Gould, and J.-Q. Wu. 2019. The F-BAR Domain of Rga7 Relies on a Cooperative Mechanism of Membrane Binding with a Partner Protein during Fission Yeast Cytokinesis. *Cell Reports*. 26:2540-2548.e2544.

Lu, Y., R. Sugiura, T. Yada, H. Cheng, S.O. Sio, H. Shuntoh, and T. Kuno. 2002. Calcineurin is implicated in the regulation of the septation initiation network in fission yeast. *Genes to Cells*. 7:1009-1019.

Luo, X., D.J. Wasilko, Y. Liu, J. Sun, X. Wu, Z.-Q. Luo, and Y. Mao. 2015. Structure of the Legionella virulence factor, SidC reveals a unique PI (4) P-specific binding domain essential for its targeting to the bacterial phagosome. *PLoS pathogens*. 11:e1004965.

Ma, A.D., L.F. Brass, and C.S. Abrams. 1997. Pleckstrin Associates with Plasma Membranes and Induces the Formation of Membrane Projections: Requirements for Phosphorylation and the NH2-terminal PH Domain. *The Journal of Cell Biology*. 136:1071-1079.

Machesky, L.M., P.J. Goldschmidt-Clermont, and T.D. Pollard. 1990. The affinities of human platelet and Acanthamoeba profilin isoforms for polyphosphoinositides account for their relative abilities to inhibit phospholipase C. *Cell regulation*. 1:937-950.

Madeira, F., Y.M. Park, J. Lee, N. Buso, T. Gur, N. Madhusoodanan, P. Basutkar, A.R.N. Tivey, S.C. Potter, R.D. Finn, and R. Lopez. 2019. The EMBL-EBI search and sequence analysis tools APIs in 2019. *Nucleic acids research*. 47:W636-W641.

Magliozzi, J.O., J. Sears, L. Cressey, M. Brady, H.E. Opalko, A.N. Kettenbach, and J.B. Moseley. 2020. Fission yeast Pak1 phosphorylates anillin-like Mid1 for spatial control of cytokinesis. *Journal of Cell Biology*. 219.

Mangione, M.C., and K.L. Gould. 2019. Molecular form and function of the cytokinetic ring. *Journal of Cell Science*. 132:jcs226928.

Mangione, M.C., C.E. Snider, and K.L. Gould. 2019. The intrinsically disordered region of the cytokinetic F-BAR protein Cdc15 performs a unique essential function in maintenance of cytokinetic ring integrity. *Molecular Biology of the Cell*. 30:2790-2801.

Marks, J., I.M. Hagan, and J.S. Hyams. 1986. Growth polarity and cytokinesis in fission yeast: the role of the cytoskeleton. *J Cell Sci Suppl*. 5:229--241.

Marks, J., and J.S. Hyams. 1985. Localization of F-actin through the cell division cycle of S*chizosaccharomyces pombe*. *Eur. J. Cell Biol*. 39:27-32.

Martín-García, R., V. Arribas, P.M. Coll, M. Pinar, R.A. Viana, S.A. Rincón, J. Correa-Bordes, J.C. Ribas, and P. Pérez. 2018. Paxillin-Mediated Recruitment of Calcineurin to the Contractile Ring Is Required for the Correct Progression of Cytokinesis in Fission Yeast. *Cell Reports*. 25:772-783.e774.

Matsuyama, A., R. Arai, Y. Yashiroda, A. Shirai, A. Kamata, S. Sekido, Y. Kobayashi, A. Hashimoto, M. Hamamoto, and Y. Hiraoka. 2006. ORFeome cloning and global analysis of protein localization in the fission yeast Schizosaccharomyces pombe. *Nature biotechnology*. 24:841.

Maundrell, K. 1993. Thiamine-repressible expression vectors pREP and pRIP for fission yeast. *Gene*. 123:127-130.

McCoy, A.J., R.W. Grosse-Kunstleve, P.D. Adams, M.D. Winn, L.C. Storoni, and R.J. Read. 2007. Phaser crystallographic software. *Journal of Applied Crystallography*. 40:658-674.

McDonald, N.A., and K.L. Gould. 2016a. Characterization of Cytokinetic F-BARs and Other Membrane-Binding Proteins. *In* Yeast Cytokinesis: Methods and Protocols. A. Sanchez-Diaz and P. Perez, editors. Springer New York, New York, NY. 181-189.

McDonald, N.A., and K.L. Gould. 2016b. Linking up at the BAR: Oligomerization and F-BAR protein function. *Cell Cycle*. 15:1977-1985.

McDonald, N.A., A.L. Lind, S.E. Smith, R. Li, and K.L. Gould. 2017. Nanoscale architecture of the Schizosaccharomyces pombe contractile ring. *eLife*. 6:e28865.

McDonald, N.A., Y. Takizawa, A. Feoktistova, P. Xu, M.D. Ohi, C.W. Vander Kooi, and K.L. Gould. 2016. The Tubulation Activity of a Fission Yeast F-BAR Protein Is Dispensable for Its Function in Cytokinesis. *Cell Reports*. 14:1--13.

McDonald, N.A., C.W. Vander Kooi, M.D. Ohi, and K.L. Gould. 2015. Oligomerization but Not Membrane Bending Underlies the Function of Certain F-BAR Proteins in Cell Motility and Cytokinesis. *Developmental Cell*. 35:725--736.

McNicholas, S., E. Potterton, K.S. Wilson, and M.E.M. Noble. 2011. Presenting your structures: the CCP4mg molecular-graphics software. *Acta crystallographica. Section D, Biological crystallography*. 67:386-394.

Mishra, M., Y. Huang, P. Srivastava, R. Srinivasan, M. Sevugan, R. Shlomovitz, N. Gov, M. Rao, and M. Balasubramanian. 2012. Cylindrical cellular geometry ensures fidelity of division site placement in fission yeast. *Journal of Cell Science*. 125:3850-3857.

Mishra, M., J. Kashiwazaki, T. Takagi, R. Srinivasan, Y. Huang, M.K. Balasubramanian, and I. Mabuchi. 2013. In vitro contraction of cytokinetic ring depends on myosin II but not on actin dynamics. *Nature Cell Biology*. 15:853--859.

Mitra, P., Y. Zhang, L.E. Rameh, M.P. Ivshina, D. McCollum, J.J. Nunnari, G.M. Hendricks, M.L. Kerr, S.J. Field, and L.C. Cantley. 2004. A novel phosphatidylinositol (3, 4, 5) P3 pathway in fission yeast. *The Journal of cell biology*. 166:205-211.

Moravcevic, K., D. Alvarado, Karl R. Schmitz, Jon A. Kenniston, Jeannine M. Mendrola, Kathryn M. Ferguson, and Mark A. Lemmon. 2015. Comparison of *Saccharomyces cerevisiae* F-BAR Domain Structures Reveals a Conserved Inositol Phosphate Binding Site. *Structure*. 23:352-363.

Morishita, M., and C. Shimoda. 2000. Positioning of medial actin rings affected by eccentrically located nuclei in a fission yeast mutant having large vacuoles. *FEMS microbiology letters*. 188:63-67.

Muñoz, J., J.C. Cortés, M. Spipiczi, M. Ramos, J.A. Clemente-Ramos, M.B. Moreno, I.M. Martins, P. Pérez, and J.C. Ribas. 2013. Extracellular cell wall β(1,3)glucan is required to couple septation to actomyosin ring contraction. *Journal of Cell Biology* 203:265-282.

Nakatsu, F., J.M. Baskin, J. Chung, L.B. Tanner, G. Shui, S.Y. Lee, M. Pirruccello, M. Hao, N.T. Ingolia, M.R. Wenk, and P. De Camilli. 2012. PtdIns4P synthesis by PI4KIIIa at the plasma membrane and its impact on plasma membrane identity. *Journal of Cell Biology*. 199:1003--1016.

Nishimura, T., M. Gecht, R. Covino, G. Hummer, M.A. Surma, C. Klose, H. Arai, N. Kono, and C.J. Stefan. 2019. Osh Proteins Control Nanoscale Lipid Organization Necessary for PI(4,5)P2 Synthesis. *Molecular Cell*. 75:1043-1057.e1048.

Nishimura, T., N. Morone, and S. Suetsugu. 2018. Membrane re-modelling by BAR domain superfamily proteins via molecular and non-molecular factors. *Biochem Soc Trans*. 46:379-389.

Oh, Y., J.H. Schreiter, H. Okada, C. Wloka, S. Okada, D. Yan, X. Duan, and E. Bi. 2017. Hof1 and Chs4 Interact via F-BAR Domain and Sel1-like Repeats to Control Extracellular Matrix Deposition during Cytokinesis. *Current Biology*. 27:2878-2886.e2875.

Ohi, M., Y. Li, Y. Cheng, and T. Walz. 2004. Negative Staining and Image Classification - Powerful Tools in Modern Electron Microscopy. *Biological procedures online*. 6:23-34.

Otwinowski, Z., and W. Minor. 1997. [20] Processing of X-ray diffraction data collected in oscillation mode. *In* Methods in Enzymology. Vol. 276. Academic Press. 307-326.

Ovesný, M., P. Křížek, J. Borkovec, Z. Švindrych, and G.M. Hagen. 2014. ThunderSTORM: a comprehensive ImageJ plug-in for PALM and STORM data analysis and super-resolution imaging. *Bioinformatics*. 30:2389-2390.

Pardo, M., and P. Nurse. 2003. Equatorial retention of the contractile actin ring by microtubules during cytokinesis. *Science*. 300:1569--1574.

Park, J.-S., S.K. Steinbach, M. Desautels, and S.M. Hemmingsen. 2009. Essential role for Schizosaccharomyces pombe pik1 in septation. *PloS one*. 4:e6179.

Pelham, R.J., and F. Chang. 2002. Actin dynamics in the contractile ring during cytokinesis in fission yeast. *Nature*. 419:82--86.

Peter, B.J., H.M. Kent, I.G. Mills, Y. Vallis, P.J.G. Butler, P.R. Evans, and H.T. McMahon. 2004. BAR Domains as Sensors of Membrane Curvature: The Amphiphysin BAR Structure. *Science*. 303:495.

Pinar, M., P.M. Coll, S.A. Rincón, and P. Pérez. 2008. Schizosaccharomyces pombe Pxl1 Is a Paxillin Homologue That Modulates Rho1 Activity and Participates in Cytokinesis. *Molecular Biology of the Cell*. 19:1727-1738.

Pollard, T.D. 2010. Mechanics of cytokinesis in eukaryotes. *Curr Opin Cell Biol*. 22:50--56.

Pollard, T.D., and J.-Q. Wu. 2010. Understanding cytokinesis: lessons from fission yeast. *Nature Reviews Molecular Cell Biology*. 11:149--155.

Proctor, S.A., N. Minc, A. Boudaoud, and F. Chang. 2012. Contributions of turgor pressure, the contractile ring, and septum assembly to forces in cytokinesis in fission yeast. *Current Biology*. 22:1601--1608.

Rajamanoharan, D., H.V. McCue, R.D. Burgoyne, and L.P. Haynes. 2015. Modulation of phosphatidylinositol 4-phosphate levels by CaBP7 controls cytokinesis in mammalian cells. *Molecular biology of the cell*. 26:1428-1439.

Ren, L., A.H. Willet, R.H. Roberts-Galbraith, N.A. McDonald, A. Feoktistova, J.S. Chen, H. Huang, R. Guillen, C. Boone, S.S. Sidhu, J.R. Beckley, and K.L. Gould. 2015. The Cdc15 and Imp2 SH3 domains cooperatively scaffold a network of proteins that redundantly ensure efficient cell division in fission yeast. *Molecular Biology of the Cell*. 26:256--269.

Revelo, N.H., D. Kamin, S. Truckenbrodt, A.B. Wong, K. Reuter-Jessen, E. Reisinger, T. Moser, and S.O. Rizzoli. 2014. A new probe for super-resolution imaging of membranes elucidates trafficking pathways. *Journal of Cell Biology*. 205:591-606.

Rincon, S.A., and A. Paoletti. 2016. Molecular control of fission yeast cytokinesis. *Seminars in Cell & Developmental Biology*:1--11.

Roberts-Galbraith, R.H., J.-S. Chen, J. Wang, and K.L. Gould. 2009. The SH3 domains of two PCH family members cooperate in assembly of the schizosaccharomyces pombe contractile ring. *Journal of Cell Biology*. 184:113--127.

Roberts-Galbraith, R.H., M.D. Ohi, B.A. Ballif, J.-S. Chen, W.H. McDonald, S.P. Gygi, J.R.I. Yates, and K.L. Gould. 2010. Dephosphorylation of F-BAR protein Cdc15 modulates its confromation and stimulates its scaffolding activity at the cell division site. *Molecular Cell*. 39:86--99.

Roubinet, C., B. Decelle, G. Chicanne, J.F. Dorn, B. Payrastre, F. Payre, and S. Carreno. 2011. Molecular networks linked by Moesin drive remodeling of the cell cortex during mitosis. *J Cell Biol*. 195:99-112.

Roux, K.J., D.I. Kim, M. Raida, and B. Burke. 2012. A promiscuous biotin ligase fusion protein identifies proximal and interacting proteins in mammalian cells. *Journal of Cell Biology*. 196:801-810.

Sbrissa, D., O.C. Ikonomov, H. Fenner, and A. Shisheva. 2008. ArPIKfyve homomeric and heteromeric interactions scaffold PIKfyve and Sac3 in a complex to promote PIKfyve activity and functionality. *Journal of molecular biology*. 384:766-779.

Schindelin, J., I. Arganda-Carreras, E. Frise, V. Kaynig, M. Longair, T. Pietzsch, S. Preibisch, C. Rueden, S. Saalfeld, and B. Schmid. 2012. Fiji: an open-source platform for biological-image analysis. *Nature methods*. 9:676.

Schink, K.O., K.-W. Tan, and H. Stenmark. 2016. Phosphoinositides in Control of Membrane Dynamics. *Annual Review of Cell and Developmental Biology*. 32:143-171.

Senju, Y., Y. Itoh, K. Takano, S. Hamada, and S. Suetsugu. 2011. Essential role of PACSIN2/syndapin-II in caveolae membrane sculpting. *Journal of Cell Science*. 124:2032.

Sethi, K., S. Palani, J.C. Cortés, M. Sato, M. Sevugan, M. Ramos, S. Vijaykumar, M. Osumi, N.I. Naqvi, J.C. Ribas, and M.K. Balasubramanian. 2016. A New Membrane Protein Sbg1 Links the Contractile Ring Apparatus and Septum Synthesis Machinery in Fission Yeast. *PLoS Genetics* 12:e1006383.

Shimada, A., H. Niwa, K. Tsujita, S. Suetsugu, K. Nitta, K. Hanawa-Suetsugu, R. Akasaka, Y. Nishino, M. Toyama, L. Chen, Z.-J. Liu, B.-C. Wang, M. Yamamoto, T. Terada, A. Miyazawa, A. Tanaka, S. Sugano, M. Shirouzu, K. Nagayama, T. Takenawa, and S. Yokoyama. 2007. Curved EFC/F-BAR-domain dimers are joined end to end into a filament for membrane invagination in endocytosis. *Cell*. 129:761-772.

Shoham, N.G., M. Centola, E. Mansfield, K.M. Hull, G. Wood, C.A. Wise, and D.L. Kastner. 2003. Pyrin binds the PSTPIP1/CD2BP1 protein, defining familial Mediterranean fever and PAPA syndrome as disorders in the same pathway. *Proceedings of the National Academy of Sciences*. 100:13501.

Snead, W.T., C.C. Hayden, A.K. Gadok, C. Zhao, E.M. Lafer, P. Rangamani, and J.C. Stachowiak. 2017. Membrane fission by protein crowding. *Proceedings of the National Academy of Sciences*. 114:E3258.

Snider, C.E., M. Chandra, N.A. McDonald, A.H. Willet, S.E. Collier, M.D. Ohi, L.P. Jackson, and K.L. Gould. 2020a. Opposite Surfaces of the Cdc15 F-BAR Domain Create a Membrane Platform That Coordinates Cytoskeletal and Signaling Components for Cytokinesis. *Cell Rep*. 33:108526.

Snider, C.E., A.H. Willet, H.T. Brown, J.S. Chen, J.M. Evers, and K.L. Gould. 2020b. Fission yeast Opy1 is an endogenous PI(4,5)P(2) sensor that binds to the phosphatidylinositol 4-phosphate 5-kinase Its3. *J Cell Sci*. 133.

Snider, C.E., A.H. Willet, H.T. Brown, and K.L. Gould. 2018. Analysis of the contribution of phosphoinositides to medial septation in fission yeast highlights the importance of PI(4,5)P2 for medial contractile ring anchoring. *Molecular Biology of the Cell*. 29:2148-2155.

Snider, C.E., A.H. Willet, J.-S. Chen, G. Arpağ, M. Zanic, and K.L. Gould. 2017. Phosphoinositide-mediated ring anchoring resists perpendicular forces to promote medial cytokinesis. *J Cell Biol*. 216:3041-3050.

Sohrmann, M., C. Fankhauser, C. Brodbeck, and V. Simanis. 1996. The dmf1/mid1 gene is essential for correct positioning of the division septum in fission yeast. *Genes & Development*. 10:2707--2719.

Spencer, S., D. Dowbenko, J. Cheng, W. Li, J. Brush, S. Utzig, V. Simanis, and L.A. Lasky. 1997. PSTPIP: a tyrosine phosphorylated cleavage furrow-associated protein that is a substrate for a PEST tyrosine phosphatase. *The Journal of Cell Biology*. 138:845--860.

Stachowiak, Matthew R., C. Laplante, Harvey F. Chin, B. Guirao, E. Karatekin, Thomas D. Pollard, and B. O'Shaughnessy. 2014. Mechanism of Cytokinetic Contractile Ring Constriction in Fission Yeast. *Developmental Cell*. 29:547-561.

Stanishneva-Konovalova, T.B., C.F. Kelley, T.L. Eskin, E.M. Messelaar, S.A. Wasserman, O.S. Sokolova, and A.A. Rodal. 2016. Coordinated autoinhibition of F-BAR domain membrane binding and WASp activation by Nervous Wreck. *Proc Natl Acad Sci U S A*. 113:E5552-5561.

Stefan, C.J., A. Audhya, and S.D. Emr. 2002. The yeast synaptojanin-like proteins control the cellular distribution of phosphatidylinositol (4,5)-bisphosphate. *Molecular Biology of the Cell*. 13:542--557.

Steinkühler, J., R.L. Knorr, Z. Zhao, T. Bhatia, S.M. Bartelt, S. Wegner, R. Dimova, and R. Lipowsky. 2020. Controlled division of cell-sized vesicles by low densities of membrane-bound proteins. *Nat. Commun.* 11:905.

Strahl, T., I.G. Huttner, J.D. Lusin, M. Osawa, D. King, J. Thorner, and J.B. Ames. 2007. Structural insights into activation of phosphatidylinositol 4-kinase (Pik1) by yeast frequenin (Frq1). *Journal of Biological Chemistry*. 282:30949-30959.

Suetsugu, S., and A. Gautreau. 2012. Synergistic BAR–NPF interactions in actin-driven membrane remodeling. *Trends in Cell Biology*. 22:141-150.

Suetsugu, S., K. Toyooka, and Y. Senju. 2010. Subcellular membrane curvature mediated by the BAR domain superfamily proteins. *Semin Cell Dev Biol*. 21:340-349.

Sun, L., R. Guan, I.J. Lee, Y. Liu, M. Chen, J. Wang, J.-Q. Wu, and Z. Chen. 2015. Mechanistic Insights into the Anchorage of the Contractile Ring by Anillin and Mid1. *Developmental Cell*. 33:413--426.

Swulius, M.T., L.T. Nguyen, M.S. Ladinsky, D.R. Ortega, S. Aich, M. Mishra, and G.J. Jensen. 2018. Structure of the fission yeast actomyosin ring during constriction. *Proceedings of the National Academy of Sciences*. 115:E1455.

Takano, K., K. Toyooka, and S. Suetsugu. 2008. EFC/F-BAR proteins and the N-WASP-WIP complex induce membrane curvature-dependent actin polymerization. *Embo Journal*. 27:2817-2828.

Takegawa, K., D.B. DeWald, and S.D. Emr. 1995. Schizosaccharomyces pombe Vps34p, a phosphatidylinositol-specific PI 3-kinase essential for normal cell growth and vacuole morphology. *Journal of cell science*. 108:3745-3756.

Tarantino, N., J.Y. Tinevez, E.F. Crowell, B. Boisson, R. Henriques, M. Mhlanga, F. Agou, A. Isral, and E. Laplantine. 2014. TNF and IL-1 exhibit distinct ubiquitin requirements for inducing NEMO-IKK supramolecular structures. *Journal of Cell Biology*. 204:231--245.

Thewes, S. 2014. Calcineurin-Crz1 Signaling in Lower Eukaryotes. *Eukaryotic Cell*. 13:694.

Thomas, C.C., S. Dowler, M. Deak, D.R. Alessi, and D.M.F. van Aalten. 2001. Crystal structure of the phosphatidylinositol 3,4-bisphosphate-binding pleckstrin homology (PH) domain of tandem PH-domain-containing protein 1 (TAPP1): molecular basis of lipid specificity. *Biochemical Journal*. 358:287-294.

Tinevez, J.-Y., N. Perry, J. Schindelin, G.M. Hoopes, G.D. Reynolds, E. Laplantine, S.Y. Bednarek, S.L. Shorte, and K.W. Eliceiri. 2017. TrackMate: An open and extensible platform for single-particle tracking. *Methods*. 115:80-90.

Traub, Linton M. 2015. F-BAR/EFC Domain Proteins: Some Assembly Required. *Developmental Cell*. 35:664-666.

Tsuboi, S., H. Takada, T. Hara, N. Mochizuki, T. Funyu, H. Saitoh, Y. Terayama, K. Yamaya, C. Ohyama, S. Nonoyama, and H.D. Ochs. 2009. FBP17 Mediates a Common Molecular Step in the Formation of Podosomes and Phagocytic Cups in Macrophages. *Journal of Biological Chemistry*. 284:8548-8556.

Tsujita, K., T. Takenawa, and T. Itoh. 2015. Feedback regulation between plasma membrane tension and membrane-bending proteins organizes cell polarity during leading edge formation. *Nature Cell Biology*. 17:749-+.

Vancurova, I., J.H. Choi, H. Lin, J. Kuret, and A. Vancura. 1999. Regulation of Phosphatidylinositol 4-Phosphate 5-Kinase fromSchizosaccharomyces pombe by Casein Kinase I. *Journal of Biological Chemistry*. 274:1147-1155.

Vavylonis, D., J.-Q. Wu, S. Hao, B. Shaughnessy, and T.D. Pollard. 2008. Assembly Mechanism of the Contractile Ring for Cytokinesis by Fission Yeast. *Science*. 319:97.

Venables, W.N., and B.D. Ripley. 2002. Modern Applied Statistics with S. Springer-Verlag New York, New York. 498.

Wach, A., A. Brachat, R. Pöhlmann, and P. Philippsen. 1994. New heterologous modules for classical or PCR-based gene disruptions in Saccharomyces cerevisiae. *Yeast*. 10:1793--1808.

Wachtler, V., Y. Huang, J. Karagiannis, and M.K. Balasubramanian. 2006. Cell Cycle-dependent Roles for the FCH-Domain Protein Cdc15p in Formation of the Actomyosin Ring in Schizosaccharomyces pombe. *Molecular Biology of the Cell*. 17:3254--3266.

Waite, A.L., P. Schaner, N. Richards, B. Balci-Peynircioglu, S.L. Masters, S.D. Brydges, M. Fox, A. Hong, E. Yilmaz, D.L. Kastner, E.L. Reinherz, and D.L. Gumucio. 2009. Pyrin Modulates the Intracellular Distribution of PSTPIP1. *PLOS ONE*. 4:e6147.

Wang, N., L. Lo Presti, Y.H. Zhu, M. Kang, Z. Wu, S.G. Martin, and J.-Q. Wu. 2014. The novel proteins Rng8 and Rng9 regulate the myosin-V Myo51 during fission yeast cytokinesis. *Journal of Cell Biology*. 205:357--375.

Wang, Q., M. Navarro, G. Peng, E. Molinelli, S.L. Goh, B.L. Judson, K.R. Rajashankar, and H. Sondermann. 2009. Molecular mechanism of membrane constriction and tubulation mediated by the F-BAR protein Pacsin/Syndapin. *Proceedings of the National Academy of Sciences of the United States of America*. 106:12700-12705.

Waters, J.C. 2009. Accuracy and precision in quantitative fluorescence microscopy. *Journal of Cell Biology*. 185:1135--1148.

Wenk, M.R., L. Lucast, G. Di Paolo, A.J. Romanelli, S.F. Suchy, R.L. Nussbaum, G.W. Cline, G.I. Shulman, W. McMurray, and P. De Camilli. 2003. Phosphoinositide profiling in complex lipid mixtures using electrospray ionization mass spectrometry. *Nature biotechnology*. 21:813.

Werler, P.J.H., E. Hartsuiker, and A.M. Carr. 2003. A simple Cre-loxP method for chromosomal N-terminal tagging of essential and non-essential Schizosaccharomyces pombe genes. *Gene*. 304:133--141.

West, R.R., E.V. Vaisberg, R. Ding, P. Nurse, and J.R. McIntosh. 1998. cut11+: a gene required for cell cycle-dependent spindle pole body anchoring in the nuclear envelope and bipolar spindle formation in Schizosaccharomyces pombe. *Molecular biology of the cell*. 9:2839-2855.

Wigington, C.P., J. Roy, N.P. Damle, V.K. Yadav, C. Blikstad, E. Resch, C.J. Wong, D.R. Mackay, J.T. Wang, I. Krystkowiak, D.A. Bradburn, E. Tsekitsidou, S.H. Hong, M.A. Kaderali, S.L. Xu, T. Stearns, A.C. Gingras, K.S. Ullman, Y. Ivarsson, N.E. Davey, and M.S. Cyert. 2020. Systematic Discovery of Short Linear Motifs Decodes Calcineurin Phosphatase Signaling. *Mol Cell*. 79:342-358.e312.

Willet, A.H., N.A. McDonald, K.A. Bohnert, M.A. Baird, J.R. Allen, M.W. Davidson, and K.L. Gould. 2015a. The F-BAR Cdc15 promotes contractile ring formation through the direct recruitment of the formin Cdc12. *The Journal of Cell Biology*. 208:391--399.

Willet, A.H., N.A. McDonald, and K.L. Gould. 2015b. Regulation of contractile ring formation and septation in Schizosaccharomyces pombe. *Current Opinion in Microbiology*. 28:46--52.

Winn, M.D., C.C. Ballard, K.D. Cowtan, E.J. Dodson, P. Emsley, P.R. Evans, R.M. Keegan, E.B. Krissinel, A.G.W. Leslie, A. McCoy, S.J. McNicholas, G.N. Murshudov, N.S. Pannu, E.A. Potterton, H.R. Powell, R.J. Read, A. Vagin, and K.S. Wilson. 2011. Overview of the CCP4 suite and current developments. *Acta crystallographica. Section D, Biological crystallography*. 67:235-242.

Wong, R., I. Hadjiyanni, H.-C. Wei, G. Polevoy, R. McBride, K.-P. Sem, and J.A. Brill. 2005. PIP2 Hydrolysis and Calcium Release Are Required for Cytokinesis in Drosophila Spermatocytes. *Current Biology*. 15:1401-1406.

Wood, V., M.A. Harris, M.D. McDowall, K. Rutherford, B.W. Vaughan, D.M. Staines, M. Aslett, A. Lock, J. Bähler, and P.J. Kersey. 2012. PomBase: a comprehensive online resource for fission yeast. *Nucleic acids research*. 40:D695-D699.

Wu, J.-Q., and T.D. Pollard. 2005. Counting Cytokinesis Proteins Globally and Locally in Fission Yeast. *Science*. 310:310.

Wu, J.-Q., V. Sirotkin, D.R. Kovar, M. Lord, C.C. Beltzner, J.R. Kuhn, and T.D. Pollard. 2006. Assembly of the cytokinetic contractile ring from a broad band of nodes in fission yeast. *Journal of Cell Biology*. 174:391-402.

Wu, J.Q., J.R. Kuhn, D.R. Kovar, and T.D. Pollard. 2003. Spatial and temporal pathway for assembly and constriction of the contractile ring in fission yeast cytokinesis. *Developmental Cell*. 5:723--734.

Wullschleger, S., David H. Wasserman, A. Gray, K. Sakamoto, and Dario R. Alessi. 2011. Role of TAPP1 and TAPP2 adaptor binding to PtdIns(3,4)P2 in regulating insulin sensitivity defined by knock-in analysis. *Biochemical Journal*. 434:265-274.

Yao, G., X. Su, V. Nguyen, K. Roberts, X. Li, A. Takakura, M. Plomann, and J. Zhou. 2014. Polycystin-1 regulates actin cytoskeleton organization and directional cell migration through a novel PC1-Pacsin 2-N-Wasp complex. *Hum Mol Genet*. 23:2769-2779.

Yoshida, T., T. Toda, and M. Yanagida. 1994. A calcineurin-like gene ppb1+ in fission yeast: mutant defects in cytokinesis, cell polarity, mating and spindle pole body positioning. *Journal of Cell Science*. 107:1725.

Zhang, Y., R. Sugiura, Y. Lu, M. Asami, T. Maeda, T. Itoh, T. Takenawa, H. Shuntoh, and T. Kuno. 2000. Phosphatidylinositol 4-Phosphate 5-Kinase Its3 and Calcineurin Ppb1 Coordinately Regulate Cytokinesis in Fission Yeast. *Journal of Biological Chemistry*. 275:35600--35606.

Zhu, Y.H., J. Hyun, Y.Z. Pan, J.E. Hopper, J. Rizo, and J.Q. Wu. 2018. Roles of the fission yeast UNC-13/Munc13 protein Ync13 in late stages of cytokinesis. *Mol Biol Cell*. 29:2259-2279.